The Study of the Growth Mechanism of TiO_2 Nanotubes and Their Applications

By

Zainab Taha Al-Abdullah

A Thesis Submitted for the Degree of Doctor of Philosophy

School of Life Sciences

University of Sussex

November 2012

Declaration

I hereby declare that this work has not been submitted in any substance to another University for the award of any other degree or other academic or professional distinction.

Signature ……..…….. Zainab Taha Yassin Al-Abdullah

Acknowledgments

I would like to express my sincere gratitude and obligation to my supervisor Dr. Qiao Chen for guiding me through my study. I started working with him with very little knowledge of the subject, but his patience and support helped me gain a lot of experimental skills and understanding. I am grateful for all the help and the support from him and his research group. Without them, the thesis would be impossible.

I would also like to thank my second supervisor, Dr. Alaa Abdul-Sada who has given valuable advice, help and support throughout this work.

I would like to thank the Ministry of Higher Education and Scientific Research in Iraq for giving me this great opportunity and sponsoring my PhD study. I hope my work will benefit the country in the future.

I would like to express my warmest thanks to Victoria Smith for her assistance in the English language and support. I would also like to thank my colleague Rantej Kler for the support and help with computer programmes and sharing knowledge. I am grateful to our group members, including Daniel Lester, Fang Yuanxing, Teo Mertanen, Giacomo Canciani, Ali Shahroozi, Brnyia Omar, Adward Lee and Jasbir Bedi, for their help and sharing their knowledge and experiences. I specially thank Dr. Mark Osborne and his group members Simon Cooper and Remi Boulineau for their help and support. I wish to express my enormous gratitude to Prof. Malcolm Heggie and Dr John Turner for their encouragement and academic support. Special thanks must goes to Dr. Julian

Thorpe for TEM imaging. I would also like to thank Mr. Mick Henry in the teaching lab for his help. I would like to thank Dr. Talib Al-Salih for encouragement and support.

Although Karen White is no longer a member of the Sussex staff, I would like to extend my gratitude for her help and kindness throughout the process leading to the offer of a place.

I would like to express my gratitude to my dear husband and my lovely kids for all the patience, help and encouragement throughout the whole intense process and I am sorry that they had to sacrifice part of their life, plans and dreams to allow me to achieve my ambition.

I would like to express my sincere gratitude to my father for offering his house a surety for my scholarship. This showed the confidence he had in me. Special thanks to my mother and brothers who have always been there for me in all the difficult times, for their love, support and encouragement, for their belief in my ability during my experience in the UK.

Special thank for my friends Dr. Waleed Alhusabi, Dr Raghad Al-Salhi, Shatha Sami, Youssra Al-Hilaly, Dr. Asma Mohammed, Maan Rasheed and Amran Yunis for providing great assistance and always being available for help and suggestions.

I dedicate this thesis to my dear Bassam

University of Sussex

Zainab Taha Yassin Al-Abdullah

D.Phil

The Study of the Growth Mechanism of TiO_2 Nanotubes and Their Applications

Summary

This research project focused on the creation of nanomaterials and their applications. The main aim was to control the growth of TiO_2 nanotubes with various morphologies and to investigate potential applications for controlled drug release and for photocatalytic water splitting.

The electrochemical anodisation process in fluoride-containing organic electrolytes was employed to prepare vertically aligned TiO_2 nanotubular arrays, with inner diameters of individual nanotubes ranging from 50 to 150 nm. A variety of morphologies was created by precise control of experimental conditions and parameters. The formation of crystal phases in the TiO_2 nanotubes was controlled by the annealing temperature (in air) and monitored by powder X-ray diffraction (XRD).

The fundamental anodisation parameters affecting the morphologies, such as anodisation voltage, electrolyte composition, stirring and the effect of magnetic fields were investigated. Various processing procedures that affect the anodisation process have been studied. The influence of hydroxide islands on the growth mechanism was shown by analysis of anodisation current-time profiles, contact angle measurements and SEM observations.

The effect of pre-patterns on the Ti substrate was also studied. The substrate was patterned either mechanically or by Electron Beam Lithography (EBL) with polymethylmethacrylate (PMMA) as a positive photoresist. Instead of circular nanotubes, polygonal TiO_2 nanotubes were formed from the mechanically patterned substrate whereas rectangular and tube-in-tube TiO_2 nanotubes were formed by using EBL.

The TiO_2 nanotubes were used as photoanodes for photocatalytic water splitting using a photoelectrochemical cell for generating hydrogen gas. The effects of nanotube morphology and crystal structure on the efficiency of the conversion of photon energy to chemical energy were studied on samples annealed at various temperatures, and with a range of organic hole scavengers.

In addition, control of the morphology was realised by surface passivation with organic thin films and by the control of the anodisation parameters. With stepwise control, bottle shaped nanotubes (nanobottles) were designed and created for their application in controlled drug release.

Scanning and transmission electronic microscopy (SEM and TEM) were used to examine the structure and morphology of the nanotubes. The surface composition was studied by X-ray Photo-electron Spectroscopy (XPS) and Energy Dispersive X-ray Spectroscopy (EDX). Crystal phases were identified by XRD.

Table of contents

List of Abbreviations

(d)	Barrier layer thickness [nm]
(*h*)	Plank constant [6.62 *10^{-34} J/s]
(h^+)	Hole
(nm)	Nanometer
˚C	Degree centigrade
µm	Micrometer
AAO	anodic aluminium oxide
AM	Air mass
AM_0	Air mass characterize the solar radiation in the space
ATO	Anodic titanium oxide
CB	Conduction band
d spacing	Distance between planes in a crystal [Å]
DI water	Deionised water
DSSC(s)	Dye sensitized solar cell(s)
e^-	Electron
EBL	Electron beam lithography
EDTA	Ethylenediaminetetraacetic acid
EDX	Energy dispersive X-ray spectroscopy
EG	Ethylene glycol
EMF	Electromotive force of the cell
Eqn	Equation
F	Field strength across the oxide
FF	Fill factor

F_g	Growth factor
HOMO	highest occupied molecular orbitals
ID	Nanotube inner diameter
I_{sc}	Short circuit current
I-V curve	Current voltage curve
J	Current density passing across the anodic oxide
kV	Kilovolt
K_α	Emission Energy for Electronic transition
L	Nanotube length
LIB	Lithium ion battery
LUMO	Lowest unoccupied molecular orbital
M	Metal
MB	Methylene blue
MO	Metal oxide
N_A	Avogadro's number mol^{-1}
OD	Nanotube outer diameter
ODPA	Octadecylphosphonic acid
PC	Photocurrent
PEC	Photoelectrochemical cell
P_{inc}	Incident power [W]
P_{max}	Maximum power(maximum)
PMMA	Polymethylmethaacrylate
PV	Photovoltaic
PVA	Polyvinyl alcohol
SAED	Selected area electron diffraction

SEI	Secondary electron image
SEM	Scanning electron microscopy
TEM	Transmission electron microscopy
UV	Ultraviolet
V	Applied anodisation voltage [V]
v	The frequency of the light
VB	Valence band
V_{oc}	Open circuit voltage
vol.%	Volume percentage %
W	Nanotube wall thickness
Wt.%	Weight percentage%
XPS	X-ray photoelectron spectroscopy
XRD	X-ray diffraction
ΔG_{298}	Gibb's free energy of formation at 298K [kJ / mol)]
ΔU	Change in potential across the oxide
η	Efficiency of the solar cell

List of Figures

List of Tables

List of publications

Al-Abdullah, Z.T.Y., Shin, Y.Y., Kler, R., Perry, C.C., Zhou, W.Z. and Chen, Q. *The influence of hydroxide on the initial stages of anodic growth of TiO_2 nanotubular arrays*. **Nanotechnology**, 2010. 21(50).

Chapter 1 Introduction

1.1 An Overview of TiO_2 Nanotube Structure and Synthesis

Titanium dioxide, TiO_2, known as titania, is one of the most widely studied metal oxide semiconductors due to its excellent photocatalytic activity [1-3]. It is therefore not surprising that over the past decades, researchers have focused their studies on the production and processing of nanotitania. Titanium dioxide has three types of crystal structure [4]. Figure 1.1 shows, rutile (tetragonal, structure a), anatase (tetragonal, structure b) and brookite (orthorhombic, structure c).

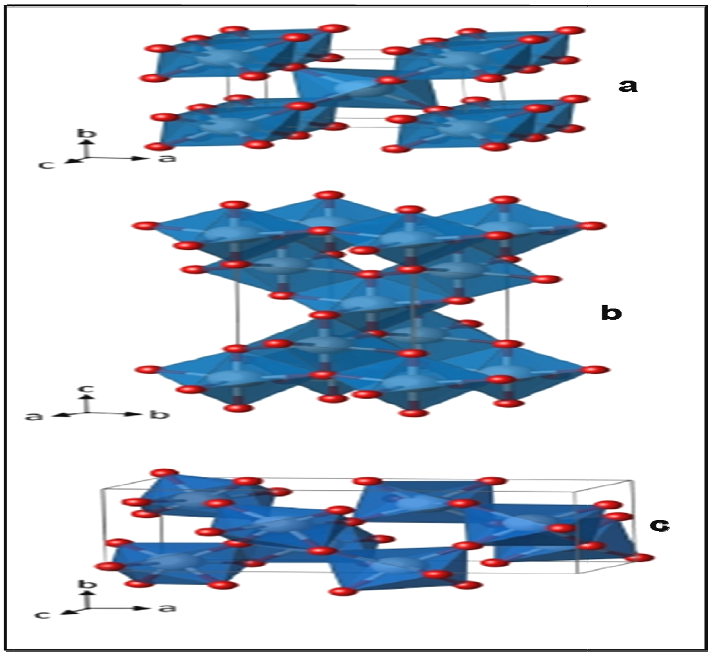

Figure 1.1 Crystal structures of TiO_2 (a) Rutile (b) Anatase (c) Brookite. Ti (white) and O (red) [5].

These three crystal structures are made up of distorted octahedra, each representing a TiO_6 unit, in which Ti^{4+} is at the centre and O^{2-} ions are at the corners.

The wire frames in Figure 1.1 represent the unit cell of the TiO_2 phases [5]. In each unit cell, there are two, four and eight Ti^{4+} cations for rutile, anatase, and brookite respectively, corresponding to two, four and eight TiO_2 formula units.

When amorphous TiO_2 is annealed, anatase is formed at 280 ºC. Rutile is formed at 650 ºC. The difference in the formation temperature is reflected in the higher density and lower molecular volume of rutile, as seen from Table 1.1. For rutile and anatase the Ti-O bond lengths are similar; however anatase has higher range of O-Ti-O bond angles than rutile resulting from the distortion of the octahedra in its more open structure [6]. Brookite is obtained as a mineral but it can't be formed under normal laboratory conditions.

Table 1.1 The crystal structures of TiO_2 [4, 6].

Structures	Refractive Index	Crystal system	Band gap(eV)	Density(g/m^3)	Volume/molecule ($Å^3$)	O-Ti-O Bond angles
Rutile	2.72	Tetragonal	3.00	4.13	31.2160	81.2° - 90.0°
Anatase	2.52	Tetragonal	3.19	3.79	34.0610	77.7° - 92.6°
Brookite	2.63	Orthorhombic	3.11	3.99	32.1720	77.0° - 105°

The properties of TiO_2 determine its applications. For example, the high refractive index and bright white colour of titanium dioxide lead to its widespread use as a pigment.

As a wide-band-gap semiconductor, TiO_2 nanomaterials have received a great deal of attention due to their high chemical stability and photocatalytic activity [7, 8].

At room temperature, TiO_2 is stable under normal acidic and basic conditions, except in HF solutions, and resistant to corrosion by common gases.

TiO_2 nanomaterials present promising opportunities in high efficiency solar energy harvesting systems, which are expected to reduce dependence on fossil-fuel based energy sources [9]. Both TiO_2 nanotubes and nanofibers were developed for solar cells which convert solar energy into electrical energy [10, 11]. The nanotube-based dye sensitized solar cell(s) (DSSC(s)) are expected to collect the light more efficiently than conventional DSSCs, possibly due to stronger light scattering effects, although their use is far from optimized [1]. The production of nanostructures and control of the electronic structures of the TiO_2 can potentially improve the efficiency of photovoltaic devices [1, 12, 13]. Similarly, TiO_2 nanomaterials could also play a crucial role as photoanodes in generating energy from hydrogen; the photoexcited electrons and holes are directly used to break the H-O bond in water [14]. TiO_2 can also be used as a photocatalyst for degradation of pollutants in the environment [3] through formation of oxidant radicals on the surface of the photoexcited TiO_2.

Anodised TiO_2 nanotubes are vertically aligned on the underlying Ti plate. They are interesting nanomaterials with various applications due to their unique structural properties [2] including their highly ordered three-dimensional, one-end open tubular structure, large surface area, large aspect ratio and excellent biocompatibility. Such vertical aligned structures are ideal for high efficiency solar cells [15-22], photocatalysis [2, 23, 24] and bioapplications [25].

1.1.1 The Electronic Structure of the Semiconductor

The electronic structure of TiO_2 can be described by the formation of molecular orbitals. Molecular orbitals are formed from the linear combination of multiple periodically arranged atomic orbitals. When a large number of orbitals overlap they form essentially continuous bands with s, p, and d orbital character. The valence band is formed from the overlapping of the highest occupied molecular orbitals (HOMOs) whilst the higher energy conduction band evolves from the overlap of the lowest unoccupied molecular orbitals (LUMOs). The separation between the two is empty of energy levels and called the band gap, which defines the minimum energy required for an electronic transition in the material. The conduction band (CB) of titanium dioxide is derived from the higher energy Ti 3d orbitals while the valence band (VB) originates from the 2p orbitals of oxygen [9, 26]. The difference in the crystal structure between rutile and anatase affects the periodic arrangement and therefore the overlap of the atomic orbitals. The size of the band gap determines the absorption frequency of each material. TiO_2 is a typical n-type semiconductor that has, depending on its crystal structure, a band gap of 3.2 eV (388 nm) for anatase, 3.0 eV (415 nm) for rutile, or 3.2 to 3.5 eV in its amorphous state [27]. Light is absorbed over the boundary between UV and visible wavelengths. This gives a white colour for anatase and slightly yellow colour for rutile.

1.1.2 Fermi Level and Doping

The Fermi level is the energy at which the probability of an energy level being occupied by an electron is exactly one-half. For semiconductors the Fermi level resides within the band gap. In case of an intrinsic semiconductor the Fermi level is

approximately midway between the minimum energy of its conduction band (E_c) and maximum energy of its valence band (E_v). For n-type doping the Fermi level shifts towards the conduction band, whereas for p-type doping the Fermi level shifts towards the valence band [28, 29]. Figure 1.2 shows the shift of the Fermi level with doping.

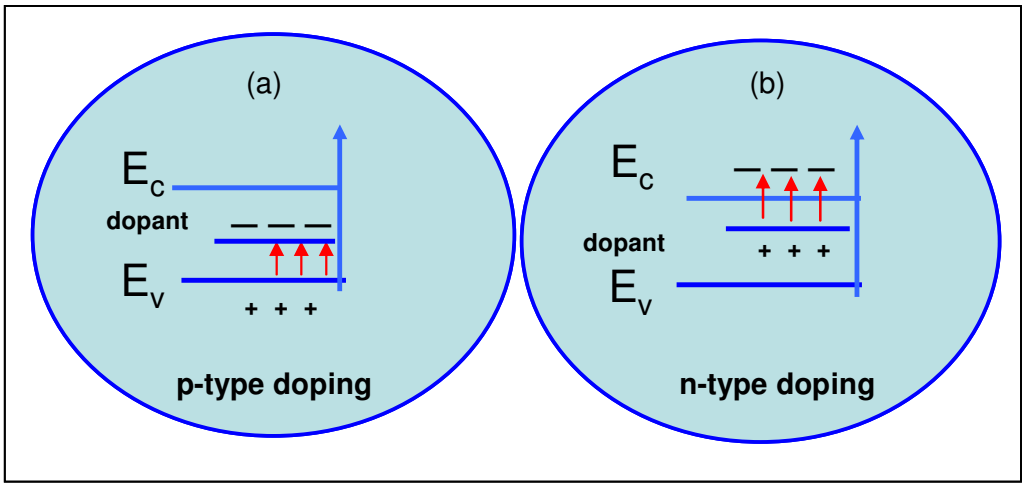

Figure 1.2 Shifts with (a) p-type doping and (b) n-type doping.

With n-type doping the Fermi level shifts towards the lowest edge of the conduction band. With, p-type doping the Fermi level shifts towards the highest edge of valence band. In both cases, the effective band gap is significantly reduced.

The activation of neat titanium dioxide is limited to photons of light at wavelengths <390 nm. This results from a large band gap and is a major limitation in the use of TiO_2 in devices using solar radiation, since the majority of solar energy is in the visible range. In order to make use of the full spectrum of solar energy, much research has focused on the reduction of the band gap [4, 30]. Non-metal doping of

TiO_2 has been shown to be effective in achieving photocatalysis activated by visible light [31].

1.1.3 The Fundamentals of Synthesis of TiO_2 Nanotubular Arrays

Nanomaterials with large surface area can take various forms and shapes, including particles, fibers, rods, spheres and tubes. My work is focused on TiO_2 nanotubes made by electrochemical anodisation. Production of titania by anodisation is simple and reliable and does not require sophisticated synthetic facilities.

The advantage of anodic films is their ability to direct charge transfer [32] due to their orientation and three-dimensional ordering. By controlling the anodisation, it is possible to tune the shape and size of nanotubes, including wall thickness, diameter and length, to meet the demands of specific applications. The production and processing of nanostructured titania has therefore been a focus of study over the past few years. The most important methods for the synthesis of nanostructured TiO_2 nanotubes are anodisation, sol-gel, hydrothermal [7], templating [33] and vapour deposition methods [9, 34]. However, most of these have limitations. For instance, the templating technique requires high temperature calcination to remove the template, resulting in possible collapse of the tubular structure [35]. For hydrothermal methods, the nanostructures are not able to assemble into closely packed oriented structures, which limit their use in photoelectrochemical applications. Only the anodisation of Ti plate using fluoride-containing electrolytes creates densely packed vertically aligned TiO_2 nanotubular arrays, similar to those generated without fluoride on an aluminium surface [1, 36-54]. Such closely packed vertically aligned arrays of nanotubes with uniform diameters are mechanically strong and suitable as electrodes for applications in

photoelectrochemistry. Their one-end open morphology makes them suitable for controlled drug release.

A native oxide layer a few nanometers thick exists on all non-noble metals in most oxygen containing environments. Approaches to growing thicker TiO_2 layers include anodic or thermal oxidation [55]. The general understanding of the anodisation of titanium in fluoride electrolytes is that an oxide layer is formed on the anode surface. This is called a barrier type (pore free) film. As the oxide film gets thicker it acts as a barrier to the flow of ions and electrons, hindering the oxidation process until it stops. The electrical field then decreases from the surface of the oxide film to the oxide/metal interface. The effective anode bias at the oxide/metal interface is almost zero, so the maximum oxide thickness is achieved. The maximum thickness obtainable per volt is only a few hundred nanometers [56]. The almost constant value of thickness per volt suggests a linear relationship between the barrier thickness and anode bias. Aqueous solutions of sulfuric, phosphoric or acetic acid [57] are some of the electrolytes capable of forming barrier type (pore free) TiO_2 films.

The passage of an anodisation current through fluoride-containing electrolytes causes the development of nanoporous and nanotubular titania layers perpendicular to the titanium metal substrate. In the presence of fluoride ion, a field directed dissolution of TiO_2 causes thinning of the oxide barrier layer, the oxide layer results in an immediate further oxidation and the formation of etching pits, which are then developed deeper into nanotubes. Under controlled conditions, these can be formed as self-organised, closed packed tubular arrays [58].

Fluoride anions readily facilitate dissolution of both titanium and titanium dioxide to give $[TiF_6]^{2-}$ anions which are stable in water.

Solutions containing hydrofluoric acid are particularly effective at dissolving titanium and its oxide which can result in very thin porous structure. The dissolution of the metal oxide layer at the solid/liquid interface is also directed by the anode bias (positive bias) which attracts the F^- anions towards the Ti plates and creates porous structure. By changing the electrolyte to a chloride-containing solution (fluoride free) applying and driving a high voltage across the circuit, bundles of TiO_2 nanotubes (i.e. not self-organized) have been prepared [50, 55] in a procedure known as rapid breakdown anodisation. In such cases, the high voltage is necessary as the complexing ability of chloride is lower than that of fluoride.

The successful generation of TiO_2 nanotubes is a direct consequence of the competition between the oxidation and dissolution processes. An organic solvent (ethylene glycol) based electrolyte containing F^- and H_2O is typically used for creating TiO_2 nanotubes in order to balance the kinetics of anodisation and dissolution. The purpose of the small amount of water is to form an oxide layer at the TiO_2/metal interface. Therefore, water molecules have to penetrate through the barrier layer, which defines the structure of the pores (diameter and close packing). Thus, higher contents of water will lead to faster oxidation and higher fluoride concentrations lead to a faster dissolution. So the anodisation rate and tubular structure can be in general controlled by changes in the concentration ratio of water and F^- and other associated parameters, such as solution temperature, anodisation current density and voltage bias. Details of the chemistry of the growth process are discussed below.

The creation of the anodic oxide layer under an applied electric field (Eqn. 1.1) is known as field assisted anodic oxidation, as opposed to the field assisted dissolution of oxide, caused by the presence of fluoride anions [59]. Eqn .1.1 illustrates the oxidation process.

$$Ti + 2H_2O \rightarrow TiO_2 + 2H_2 \quad \textbf{Equation 1.1}$$

$$TiO_2 + 6F^- + 4H^+ \rightarrow TiF_6^{2-} + 2H_2O \quad \textbf{Equation 1.2}$$

The formation of fluoro-complexes in the electrolyte is aided by the electric field, which moves fluoride anions toward the metal and Ti^{4+} toward the electrolyte. In order to maintain active oxidation ions such as Ti^{4+} and O^{2-} need to move through the anodic film. The presence of fluoride anions in the electrolyte, allows the creation of channels through which current can flow freely and keeps the oxidation process active [60]. The persistent dissolution (Eqn. 1.2) of the barrier layer continuously reduces its thickness but its regeneration by oxidation is just as relentless (Eqn. 1.1). As a result, nanotubes grow at maximum rate when the oxidation rate at the metal/oxide interface equals the rate of chemical dissolution at the oxide/electrolyte interface. The chemistry behind the complex growth of titania nanotubes and the side reactions that influence the final morphology will be discussed in a later chapter. Models and mechanisms of titania nanotube formation will also be explained.

Schmuki and co-workers [1, 61] recently proposed a more specific description of the growth of porous/tubular titania. They concluded that the growth of the porous/tubular oxide is defined by the diffusion of ions within the pores and the electrolyte.

1.1.4 Study of Anodisation Parameters

The creation of a TiO_2 nanotube is affected by the applied voltage [2], the electrolyte concentrations [62] and the anodisation temperature [63]. Both the oxidation and dissolution rates are determined by the process parameters. For instance, greater resistances in thicker barrier layers can be overcome by increasing the applied anodisation voltage or increasing the electric field by reducing the distance between electrodes. Water concentration can directly affect the oxidation rate while the flouride concentration affects the dissolution rate. At higher dissolution rates, thinner nanotubes are formed at a higher rate. The thickness of the barrier layer underneath the pores/tubes is constantly eroded by dissolution but also constantly regenerated by oxidation, determined respectively, by the applied anodic electric field and water concentration. The temperature can also affect the growth rate and tube morphology of the anodised nanotubes. The control of the parameters involved in the anodisation is the key to achieving highly ordered titanium dioxide nanotubes.

1.1.4.1 Anodisation Voltage

The effects of anodisation voltage (V) are related to the growth factor (f_g). When a valve metal is used as an anode, the barrier layer formed by oxidation impedes the current. The thickness (d) of the oxide layer depends on the applied voltage bias. With a higher voltage, a thicker layer of oxide can be formed at a higher rate. As a result, for anodic growth of oxide nanotubes, the underlying thickness of the oxide layer is proportional to the applied voltage [2]. In general, a larger diameter nanotube can be created by use of the higher anodisation voltage [1]. This can be quantitatively described as shown in eqn. 1.3.

$$OD = 2 f_g V \quad \text{..... Equation 1.3}$$

f_g is the growth factor for anodic oxides and OD is outer diameter.

The parameter f_g is a constant for Ti metal which is defined as eqn 1.4.

$$f_g = d/V \quad \text{..... Equation 1.4}$$

where, d is the maximum oxide thickness at an applied voltage V.

The OD is equal to the sum of the inner diameter (ID) and twice the wall thickness W. Therefore,

$$OD = ID + 2W \quad \text{..... Equation 1.5}$$

The experimental results show that f_g is 1-5 nm/V for TiO_2. Figure 1.3 schematically shows tube dimensions, outer and inner diameters, wall thickness and barrier layer thickness. The measured nanotube outer diameter is a function of anodisation potential.

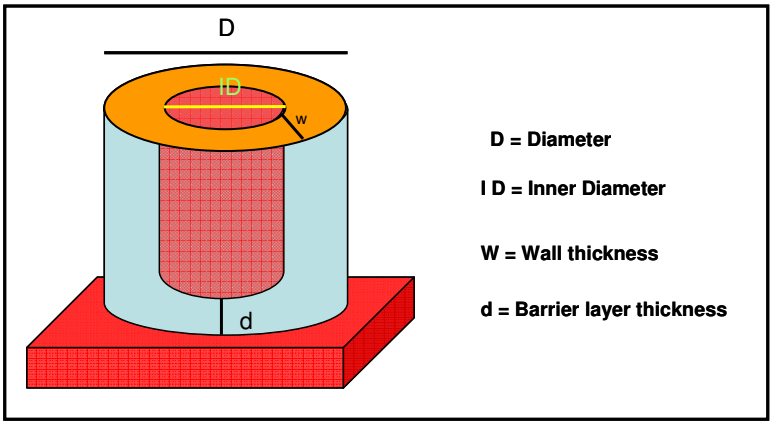

Figure 1.3 Tube dimensions, outer and inner diameters, wall thickness and barrier layer thickness of TiO_2 nanotubes.

Equations (1.3 and 1.5) summarise the relation between these parameters. Combining (Equn.1.3 and 1.5) we get:

$2 f_g V = ID + 2W$ ..... **Equation 1.6**

From eq.1.4 $f_g V = d$,

So, eqn. 1.6 can be transformed as:

$2d = ID + 2W$ ..... **Equation 1.7**

Combining 1.7 with 1.4 we get

$d = \frac{OD}{2}$ ..... **Equation 1.8**

Eqn. 1.8 shows that the outer diameter of the nanotube equals the maximum thickness of the oxide barrier layer. A higher voltage creates a thicker barrier layer and nanotubes with larger diameter.

In this project, we use the anodisation voltage to control the diameter of nanotubes in two steps to create both double wall nanotubes and nanobottles.

Together with the thickness of the barrier layer, the applied voltage also affects the ionic current, [64, 65] formed by moving ions in the electrolyte. The relationship between anodic current density (*j*) and anodizing potential has been discussed for most of the valve metals [50],

$$j = \alpha \cdot e^{(\beta.F)}$$ ..... **Equation 1.9**

α and β are constants and F is the field strength across the oxide.

The field strength F across the oxide film can be estimated from the change in potential across the oxide, ΔU and the oxide thickness d [64]:

$$F = \Delta U / d$$ ..... **Equation 1.10**

Thus the ionic current at given voltage can be described in Eqn. 1.11

$$j = \alpha \cdot e^{(\beta.\frac{\Delta U}{d})}$$ ..... **Equation 1.11**

The electric field linearly decreases with thickness, and from Eqn. 1.11 we see that the current decays nonlinearly with film thickness [64, 65].

While the system is under a constant applied voltage, the increasing oxide thickness steadily decreases the electric field strength within the oxide. As a result, the anodisation current decreases rapidly and the oxidation process slows down, and becomes self-limiting. In other words, the declining field strength leads to the growth of a compact oxide layer with a limited thickness that is proportional to the applied voltage.

1.1.4.2 The Distance between the Electrodes

In an organic electrolyte, the pore diameter (the inner diameter of the tube) is affected by the working distance between anode and cathode. With increasing working distance, the pore diameter decreases. This is accompanied by a significant drop in the current as the resistance of the electrolyte increases. As a result, the drop in the effective

potential across the oxide layer is reduced and pore diameter is reduced also [66]. With a higher anodisation current at shorter working distance, the temperature of the electrolyte increases gradually during the anodisation and so the mobility of ions in electrolyte increases, giving a larger pore diameter.

1.1.4.3 Electrolyte

The water content of the electrolyte is regulated by use of either aqueous or organic-based media. This one parameter plays a crucial role in the growth of anodised titiania nanotubes through the management of oxidation and dissolution rates. At higher water concentrations, the ion mobility is higher, in comparison with pure organic electrolyte, so an improved dissolution rate can be achieved. The nanotube growth rate is proportional to the dissolution rate near the bottom of the nanotube. However, fast dissolution at the top of the nanotube limits the final tube length. Therefore, it is necessary to manage the appropriate water concentration. For ammonium fluoride in ethylene glycol [38, 67], the water concentration should be in the range from 1 to 5%. With less than 1 vol. % water in the electrolyte compact oxide layers are formed; with more than 5 vol. % water tube ripples restrict the homogenous tube walls and regular arrangements of the tubes. Moreover, with increasing water content in the electrolyte the barrier layer thickness at the bottom of the tube increases and this leads to increases in the outer and inner diameters.

1.1.4.4 Fluoride Concentration

Fluoride concentration not only affects the pH but regulates the dissolution rate. The fluoride concentration should be minimal but it must be high enough to ensure a high growth rate and regular ordering of the tubes [62]. In order to maximise the

nanotube growth rate, the dissolution rate needs to match the oxidation rate. Increasing the fluoride concentration also increases the ionic conductivity of the electrolyte and this gives a larger nanotube diameter. The effect of the fluoride concentration on the growth of TiO_2 nanotubes is shown in chapter 3.

1.1.4.5 pH

The dissolution rate of the anodic oxide is increased in an acidic environment and so the pH of the reaction solution is extremely important. The use of fluoride salts (some of which show basic hydrolysis) instead of hydrofluoric acid lowers the dissolution rate of the anodic oxide. Sreekantan *et al* [68] controlled the rate of nanotube formation by controlling electrolyte pH. They reported that at pH 3, the rate of formation was 23 nm min^{-1}; at pH 5, 15 nm min^{-1}; and at pH 7, 8 nm min^{-1}. Thus electrolytes with lower pH give faster growth rates due to faster dissolution at the oxide-electrolyte interface. However, the true growth rate at lower pH might due to dissolution at the top of the nanotube which affects the final length of the tubes.

1.1.4.6 Temperature

Temperature can also affect the morphologies of the titanium oxides during anodisation [63]. Low temperatures reduce the rate of dissolution, ion mobility, and therefore the diameter of the nanotubes. Lowering the temperature to 2 $^{\circ}$C appears to inhibit the dissolution rate and hence tube growth in aqueous and organic based electrolytes [69]. The decrease in the electrolyte conductivity decreases the anodic voltage and therefore the nanotube diameter. In this thesis, we report that by use of a variable temperature, two step, anodisation, we have successfully created nanobottles for controlled drug delivery.

1.1.5 The Development of the Anodisation Method for Creating TiO_2 Nanotubes

The anodisation conditions were developed gradually as understanding of the growth mechanism increased. Although quantitative measurements of oxidation and dissolution rates are still incomplete, a qualitative understanding of the mechanism is well established. Historically, the synthesis of TiO_2 nanotubes by electrochemical anodisation was developed through four major steps.

1.1.5.1 The First Generation of TiO_2 Nanotubes (using Aqueous Electrolytes)

Zwilling and co-workers were the first to generate self-organized porous TiO_2 by use of a Ti-based alloy in an acidic, fluoride-based aqueous electrolyte [70]. The thickness of the oxide layer obtained by this method was limited to approximately 0.5 µm. Similarly, Gong *et al* fabricated self-organized nanotube arrays with a maximum nanotube length of 500 nm from an aqueous dilute HF electrolyte [71]. Later, it was realised that the length of the first generation of nanotubes was limited by the acidic electrolyte, which gives a high dissolution rate at the top of nanotubes and restricts further growth [72]. Dissolution of the TiO_2 limits the effective thickness of the oxide layer.

1.1.5.2 The Second Generation of TiO_2 Nanotubes (using Buffered Solutions)

In the second generation of TiO_2 nanotubes, the length of the tubes was increased to 3 µm by controlling the pH of the electrolyte [73, 74]. Hydrofluoric acid was replaced by fluoride salts, so the dissolution of TiO_2 was reduced and the thickness of the film reached up to 3 µm. The use of a buffer solution was explained by Macak *et al* [75]. When the pH at the pore bottom is lower than that at the top of the tube, which is

under a protective higher pH due to the use of ammonium fluoride/ammonium sulphate as a buffer, longer nanotubes are generated. The lower pH at the bottom of the nanotube is a direct consequence of anodic oxidation of Ti by water, which consumes oxygen atoms and leaves a H^+ rich environment. This accelerates the thinning of the barrier layer. The reactions at the bottom of the nanotube make it almost impossible to quantitatively measure the pH variation.

1.1.5.3 The Third Generation of TiO_2 Nanotubes (using Polar Organic compounds)

The third generations of nanotubes comprise smooth tubes with no ripples along the walls. The tubes were prepared in water-free, organic electrolytes where the dissolution of oxide is minimized [76]. Many organic solvents, for example glycerol and ethylene glycol, have been used as electrolytes. [43, 77] and nanotubes as long as 70 µm with a maximum outer diameter of 180 nm have been made [76]. The key to the successful growth of a high aspect ratio nanotube array is to decrease the water content in the electrolyte. This results in a decrease in the rate of dissolution of the oxide layer. Here, the aspect ratio is defined as the ratio between the tube length and the inner diameter, as estimated directly from SEM images. Nanotubes up to 1000 µm have also been achieved using ethylene glycol as an electrolyte [59]. Grimes used a polar organic electrolyte in order to enhance the extraction of Ti^{4+} from the metal and inhibited the growth of the barrier layer at the metal/oxide interface by use of large cations in the fluoride salts [59, 78].

1.1.5.4 The Fourth Generation of TiO_2 Nanotubes from (Non-Fluoride, Acid Base Electrolytes)

The fourth generation of nanotube array was obtained from non-fluoride based electrolytes. The aim was to explore the possibility that fast anodisation would give nanotubes with a wide range of aspect ratios and morphologies. Nakayama and co-workers [79] reported the production of titania nanotubes as bundles rather than regular arrays. They used various electrolytes based on acids such as oxalic, formic, hydrochloric and sulfuric acid. A significant amount of carbon was detected in the nanotubes formed from each of the organic acids. The growth of TiO_2 nanotubes by fourth generation methods occurred at the edge of the titanium surface, where there was usually a higher density of defects to give active reaction centers for the formation of the oxide layer. This layer is critical for focusing the electrical field, once dissolution is initiated.

1.2 Titanium Dioxide: A Broad Range of Applications

Fujishima and Honda [80] discovered the photocatalytic water-splitting ability of a titanium dioxide electrodes under UV and visible light and researchers have dedicated several papers to the understanding and development of the many promising applications in photocatalysis, photovoltaics and water splitting. These are summarised below.

1.2.1 TiO_2 in Photocatalysis

TiO_2 is one of the most efficient photocatalysts for the degradation of both organic and inorganic pollutants in water. Under illumination by UV light, organic matter can be decomposed through oxidation processes and mineralised into CO_2 and water. The accepted photocatalysis reaction mechanism is shown in Figure 1.4 [81].

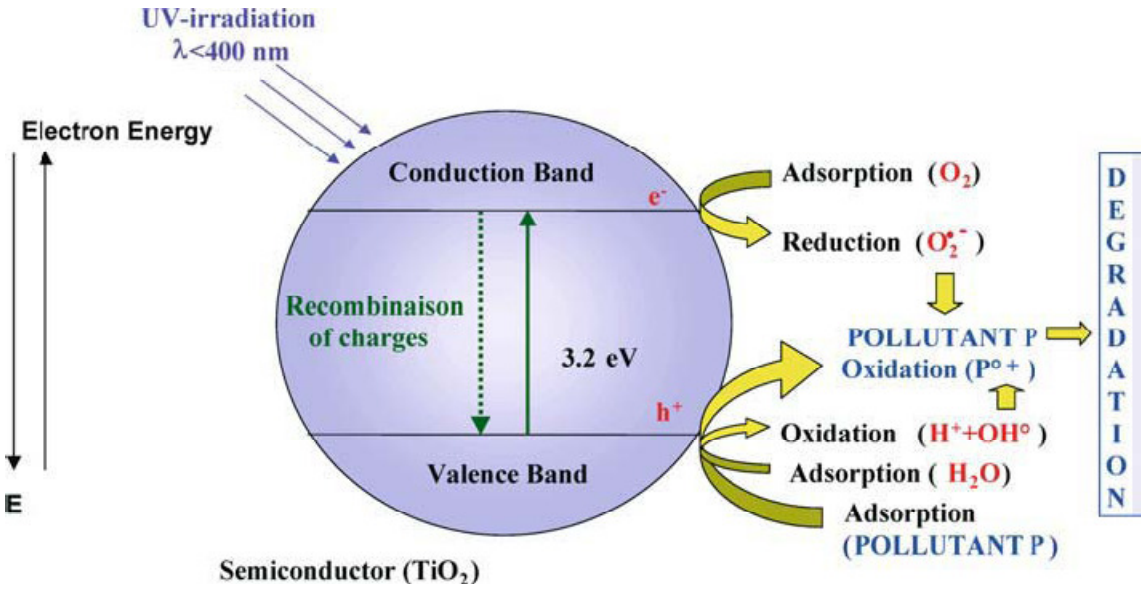

Figure 1.4 The principle of photocatalysis by TiO_2 [81]. The band gap is 3.2 eV.

Upon absorption of photons with energies higher than the band gap, (3.2 eV), electrons are excited from the valence band (VB) into the conduction band (CB) and an electron-hole pair is created [82]. These photoexcited charge carriers can become trapped in metastable states, recombine, or migrate to the surface to react with adsorbed molecules. In an aqueous environment, the photogenerated electron-hole pairs participate in reactions with adsorbed water molecules, surface hydroxyl groups and

dissolved molecular oxygen, to generate hydroxyl and highly-reactive superoxide radicals.

Although the mechanism of photocatalytic oxidation varies from one pollutant to another, the superoxide ($\dot{O}_2^-$) and, in particular, hydroxyl radicals ($\dot{O}H$) are recognized as active reagents in the degradation of organic compounds on a TiO_2 surface. These radicals can be formed by molecular oxygen and water through scavenging of the electron-hole pair [83]. The following equations (1.12-1.16) illustrate the formation of these radicals.

$$TiO_2 + h\nu \rightarrow e^- + h^+ \quad \textbf{Equation 1.12}$$

$$O_2 + e^- \rightarrow \dot{O}_2^- \quad \textbf{Equation 1.13}$$

$$H_2O + h^+ \rightarrow \dot{O}H + H^+ \quad \textbf{Equation 1.14}$$

$$\dot{O}H + \dot{O}H \rightarrow H_2O_2 \quad \textbf{Equation 1.15}$$

$$H_2O_2 + \dot{O}_2^- \rightarrow \dot{O}H + OH^- + O_2 \quad \textbf{Equation 1.16}$$

The superoxide radical is formed by reduction of adsorbed O_2 (Eqn 1.13) and the hydroxyl radical is formed by the oxidation of water (Eqn 1.14). The hydroxyl radicals may combine to form hydrogen peroxide (Eqn 1.15). The hydrogen peroxide can consume the superoxide radical and convert it to the hydroxyl radical (Eqn 1.16). It is the oxidative power of superoxide and hydroxyl radicals that breaks the C-C and C-O bonds in organic molecules.

The photocatalytic activity of a semiconductor depends on the properties of light absorption and the recombination rates of electron-hole pairs. It also depends on the surface reduction and oxidation rates by the excited electron and its positive hole. The minimum excitation energy from valence to conduction bands determines the reductive power of the excited electron which has to be higher than the $\dot{O}_2/O_2^-$ redox potential. The potential of valence band maximum has to be lower than the water oxidation potential. The difference between the electron-hole potential and the H_2O/O_2 redox potential determines the driving force for reduction and oxidation. The optimum condition is achieved when the reduction and oxidation rates are more or less equal.

Natural TiO_2 has three polymorphs; anatase, brookite, and rutile. Anatase and rutile show photocatalytic activity whereas brookite does not. Although the anatase phase forms at lower temperatures, with slightly higher band gap, it shows a much higher photocatalytic activity than rutile [81]. The positive holes produced in both phases are sufficiently deep in the VB, to give similar oxidative power; however the reducing power of anatase is greater than that of rutile because the bottom of its CB lies at lower energy sits closer to the negative position (Figure 1.4). Also, as anatase forms at lower temperatures, it usually has higher surface area than rutile. For heterogeneous gas/solid reactions, larger surface areas lead to faster reaction rates. The differences in band structure along with the increased surface area of anatase are understood to be the two main reasons for the greater photocatalytic activity of anatase.

Li *et al.* also hypothesized that TiO_2-containing a mixture of anatase and rutile phases would show even better photocatalytic activity because any kind of solid-solid

interface is a key structural feature facilitating charge separation and hindering recombination [84]. Mixed-phase TiO_2 nanocomposites indeed show enhanced photocatalytic efficiency [7].

Heating to high temperatures generally enhances crystallinity but also induces aggregation of small nanoparticles and decreases the surface area [83, 85]. For TiO_2 nanotubes high annealing temperatures decrease the surface area by sintering, and forming rutile, which results in a collapse of the tubular film. Evidently, several physical properties of TiO_2 nanomaterials need to be taken into account in order to optimise photocatalytic activity.

1.2.2 Water Splitting by TiO_2 Photocatalysis

A low-cost photoelectrochemical system would make possible the efficient harvesting of solar energy by electrolysis of water to generate hydrogen as an energy source, replace fossil fuels, and substantially decrease the release of the greenhouse gas carbon dioxide. Because the electrochemical potentials for water oxidation and proton reduction lie within the band gap of TiO_2, the photogenerated electrons in the conduction band can be used to reduce protons and generate hydrogen gas.

TiO_2 nanostructures have been studied as photoelectrodes for water splitting [86-90], and could have significant economic and environmental advantages [91, 92]. When an electron-hole pair is generated by photon excitation, the hole interacts with molecules close to the catalyst's surface and the electron moves to the cathode (Pt electrode). This system can be used for the photocatalytic electrolysis of water into hydrogen and oxygen. The excitation of electrons across the band gap of TiO_2 is

activated by only a small fraction of the energy from the sun due to the wide band gap of TiO_2, although in general, visible light has enough energy to split water into hydrogen and oxygen. Therefore, doping of anodised TiO_2 nanotubes [93] is required to reduce the band gap so that visible light can also be absorbed.

1.2.2.1 The Mechanism of Hydrogen Production by a Photoelectrochemical Cell (PEC)

The mechanism can be described by 5 steps [94]:

1- Absorption of light. A semiconductor can absorb light with energy greater than a threshold determined by the band gap (E_g).

2- Excitation of electrons from the valence band to the conduction band, leaving the valence band with hole on the photoanode (Eqn. 1.12.)

$$TiO_2 + hv \rightarrow e^- + h^+ \quad \text{Equation 1.12}$$

Here, h is Planck's constant and v is the frequency of the light.

3- Charge separation and migration. Electrons pass through the photoanode to the back-side electrical contact and holes to the interface between the photoanode and electrolyte. These electrons and holes can be used to drive redox reactions. The energy of the bottom of the conduction band edge measures the reductive strength of the electrons in the semiconductor and the energy of the top of the valence band is a measure of the oxidative power of holes in the semiconductor [95].

4- The oxidation of water can be achieved at the photoanode by holes.

$$2h^+ + H_2O_{(aq)} \rightarrow 2H^+_{(aq)} + {}^1\!/_2\, O_{2(gas)} \text{..... Equation 1.17}$$

5- H^+ ions move from the photoanode to the cathode through the electrolyte. However electrons move from photoanode to cathode through the external circuit, leading to the reduction of H^+ ions into dihydrogen gas at the cathode.

$$2H^+ + 2e^- \rightarrow H_{2(gas)} \text{..... Equation 1.18}$$

The overall reaction of the photo-electrochemical cell (PEC) is

$$2hv + H_2O_{(liquid)} \rightarrow H_{2(gas)} + {}^1\!/_2\, O_{2(gas)} \text{..... Equation 1.19}$$

This reaction takes place when the energy of the photon absorbed by the photoanode is equal to or larger than the threshold energy E_t,

$$E_t = \frac{\Delta G^\circ}{2N_A} \text{..... Equation 1.20}$$

ΔG^0 is the standard free energy (per mol) of reaction = 237 kJ/mol (when the activity $a_{H+} = 1$).

N_A is Avagadro's number = 6.022×10^{23} mol^{-1}

Then we get

$$E = hv = 1.23 \text{ eV} \text{..... Equation1.21}$$

According to (Eqn. 1.21), electrochemical decomposition of water is possible when the electromotive force of the cell (EMF) is equal to or greater than 1.23 V. But constant

electrolysis in general requires 1.5 V to overcome the impedance of the PEC and activation potentials at both anode and cathode.

1.2.2.2 The Efficiency of TiO_2 in a PEC: Problems and Solutions

The energy conversion efficiency from solar to hydrogen by photocatalytic water-splitting is limited by the recombination rate of electron-hole pairs, the fast backward reaction, and the frequency of visible light.

Upon recombination the excited electron returns to the valence band without reaction with adsorbed species. The recombination of photoinduced electron-hole pairs therefore reduces the overall quantum efficiency of the photocatalyst [96]. Due to the dissipation of energy by recombination, luminescence can be employed to measure the release of radiation and rates of recombination. Recombination is mainly at the surface where it competes strongly with the photocatalytic process.

Doping is one of the techniques used to promote electron-pair separation, reduce recombination and enhance photocatalytic activity. Hole scavengers, or electron donors, [97] have been added to TiO_2 to reduce the recombination rate. These react irreversibly with the photogenerated VB holes, thus improving the electron-hole separation. Because electron donors are consumed in the photocatalytic process, continuous replenishment of electron donors is required to maintain hydrogen production.

Hydrocarbons are widely used as electron donors for photocatalytic hydrogen production. They can be oxidized by VB holes and the remaining strongly reducing CB electrons can reduce protons to dihydrogen molecules. Ethylenediaminetetraacetic acid (EDTA), ethanol, lactic acid, methanol and formaldehyde have been examined and

proved to be effective in the enhancement of hydrogen production [98]. A qualitative study was carried out by Nada *et al* on the effects of various electron donors on the production of hydrogen [99]. The order of improvement of hydrogen production was: EDTA>methanol>ethanol>lactic acid.

The low efficiency can be caused by the back reaction between hydrogen and oxygen. This problem can be avoided by separating the evolution of hydrogen and oxygen. It has been reported that the separate evolution of H_2 and O_2 can be achieved by use of a two-compartment cell equipped with platinum electrodes and a cation exchange membrane [100].

The band gap of TiO_2 is about 3.2 eV, so only 4% of solar radiation energy is available for hydrogen production. If the band gap is reduced by doping, about 40% of the visible solar spectrum can be harvested [101]. Doping by alkaline earth metals and transition metals has been widely investigated. Choi *et al* [102] carried out a systematic study of the photoreactivity of TiO_2 doped with 21 different metal ions. They found that doping with metal ions could expand the photoresponse of TiO_2 into the visible spectrum. Since metal ions are incorporated into the TiO_2 lattice, impurity energy levels in the band gap of TiO_2 contribute to the reduction of band gap. In general, the impurity energy levels introduced by cations are near to the CB of TiO_2.

Although the fine details are still under discussion, doping by non-metallic elements can also improve the activity of TiO_2 towards visible light. Carbon and nitrogen doping seems to be particularly effective. Substiutional doping with nitrogen is believed to exclusively change the valence band structure. The presence of nitrogen

could narrow the band gap of the titanium dioxide, and promote photocatalytic activity [103]. Alternatively the presence of nitrogen simply stabilises oxygen vacancies and this enhances visible light efficiency [104, 105]. In general, such non-metal dopants form impurity energy levels near the valence band, due to their electronegtivity so that the oxidative power of the photoexcited hole is effectively reduced.

1.2.3 Photovoltaic Application

A photovoltaic (PV) cell produces direct-current related to the amount of light it receives. TiO_2 nanostructures offer opportunities to enhance the efficiency of solar energy capture and to reduce the overall cost [23, 80, 106]. Nanocrystalline TiO_2 electrodes are important in photovoltaics, since they offer large surface area with a controlled morphology. To enhance the absorption of visible light, an organic dye is often used to sensitise the TiO_2 electrode. A schematic presentation of the construction and the principles of a dye sensitized solar cell (DSSC) is presented in Figure 1.5 [16].

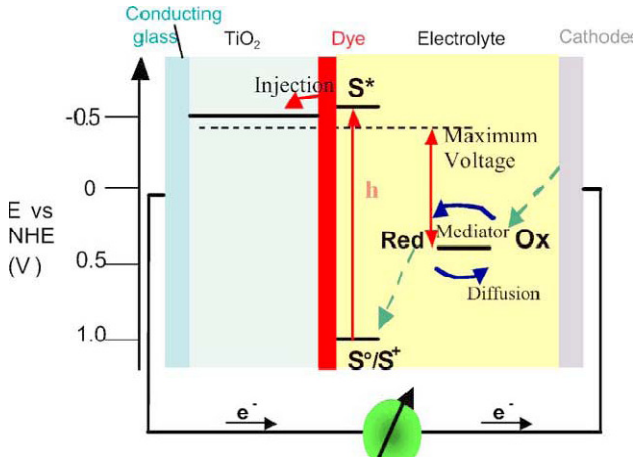

Figure 1.5 Principles of a dye-sensitized solar cell containing nanocrystalline TiO_2 [16].

The cell core consists of a nanocrystalline TiO_2 film coated with a monolayer of dye capable of charge transfer. An organic hole conductor, usually in the form of a redox electrolyte forms the next key component before the opposite electrode and the outer circuit to make electrical power. The nanocrystallinity of the TiO_2 semiconductor gives a mesoporousity that enables a large amount of dye to be adsorbed over the large surface area [9]. Upon exposure to sunlight, electrons are readily released from the sensitising dye, into the conduction band of the TiO_2. Recombination of the conduction band electron with the adsorbed dye is prevented by the redox couple in the electrolyte, which re-generates the reduced dye monolayer and allows the injected electron to move around the circuit to produce directcurrent electricity. The redox couple iodide/triiodide is a popular system for use in DSSCs. The iodide is oxidised by the hole in the dye and regenerated by the reduction of triiodide at the counterelectrode. The voltage generated under illumination corresponds to the difference between the Fermi level of TiO_2 and the ground state of the organic dye. Therefore, a dye-senstised solar cell can generate electrical power under illumination by light, without any major chemical transformations.

Both commercial nanoparticles and nanotubes have been used in DSSCs but higher charge collection efficiencies were achieved from nanotubes rather than nanoparticles [107]. This is possibly due to a better charge mobility along the nanotubes; for nanoparticles the charge transport is limited to hopping between particles [108].

1.2.3.1 Solar Energy for photoexcitation

As solar light passes through the atmosphere, the spectrum is attenuated by the absorption of molecules such as oxygen, water, ozone, methane, carbon dioxide etc. The absorption increases with the thickness of the atmosphere. The parameter d_o is the thickness of the atmosphere normal to the earth's surface. The optical path length of solar radiation across the atmosphere at an incident angle (α) is given by $d = d_o / \cos \alpha$. The ratio d / d_o is called the air mass factor (AM) [109]. Therefore, an AM 1.5 means that the spectrum is measured for light travelling 1.5 times farther than direct solar light before reaching the surface of the earth. For moderate weather an AM of 1.5 may be assumed; this corresponds to an incident angle of 48.2° relative to the surface normal and gives a mean irradiance of 100 mW cm^{-2} (= 1.0 sun). Figure 1.6a illustrates the air mass model.

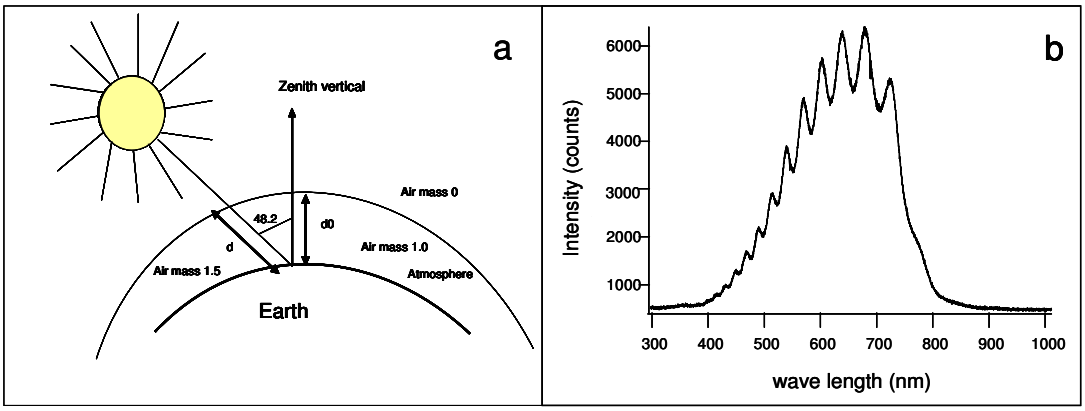

Figure 1.6 (a) The air mass factor [109], (b) the xenon Lamb spectra.

In our experiments, a focused 300 W xenon arc lamp with a parabolic reflector was used as excitation light source with a focused illumination spot area of 1 cm^2. The

spectrum of a xenon lamp Figure 1.6b is very close to that of sunlight and the power measurements were calibrated. The power for the xenon lamp was 50 mW.

1.2.3.2 Current-Voltage (*I-V*) Classification

The photoexcitation of TiO_2 for water splitting was studied for a PEC with a xenon lamp light source. The photocurrent was recorded as a function of electrochemical potential relative to the reference electrode. The two most important parameters for such current-voltage studies are the open-circuit voltage V_{OC} and the short-circuit current $I_{SC.}$ V_{OC} is the maximum voltage from a PEC at zero current and I_{SC} is the current when the voltage across the cell is zero. Figure1.7 shows a typical *I-V* curve showing the short-circuit current and the open-circuit voltage, together with a calculated power spectrum. Under both open and short circuit conditions, the output power becomes zero, since the power is defined as:

$$P = I \times V \quad \text{.....Equation 1.22}$$

The maximum power is expected at a voltage between 0 and V_{oc}.

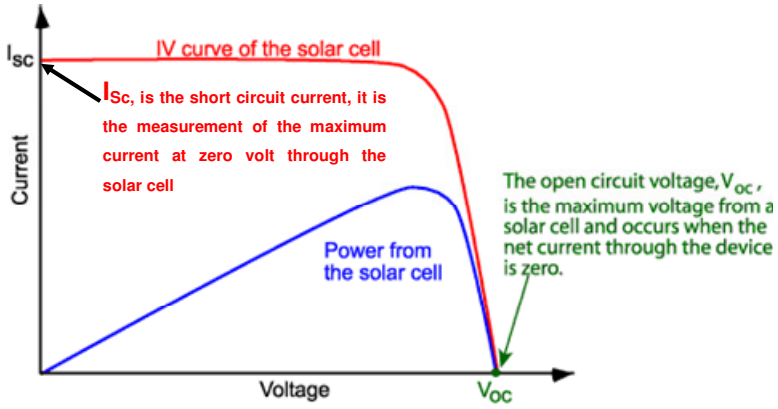

Figure 1.7 Short circuit current, open circuit voltage and power from a general solar cell.

1.2.3.3 Fill Factor

The maximum current and voltage from a solar cell are defined as the short-circuit current and the open-circuit voltage. However, under both these conditions, the power of the solar cell is zero. The fill factor (*FF*), represents the electrochemical efficiency of the PEC. It is defined as the ratio of the maximum power from the solar cell to the product of V_{oc} and j_{sc} , $j_{sc} = I_{sc} / a$

where a is the area of the electrode. It can be calculated from the curve as shown in Figure 1.8

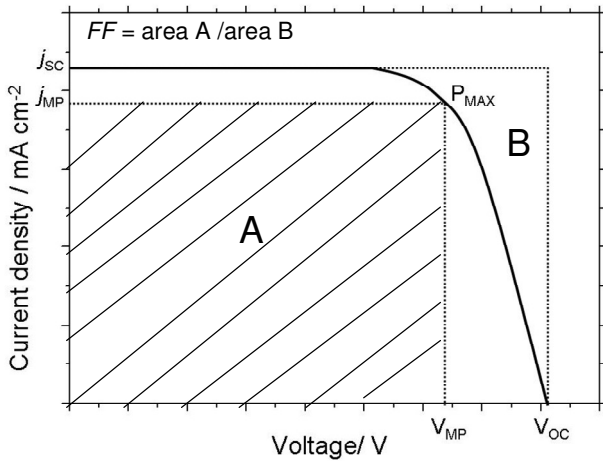

Figure 1.8 Fill factor; short-circuit current (j_{sc}), open-circuit voltage (V_{oc}) and maximum power (P_{max}), V_{MP}, is the voltage at maximum power and the j_{MP} is the current density at maximum power.

The *FF,* measured from the area of the largest rectangle which will fit into the current-voltage (*I-V*) curve, corresponds to the maximum output power. It is always less than 1. The closer the *FF* is 1, the greater the electrochemical efficiency.

1.2.3.4 The Efficiency

The performance of different PECs may be compared by their photoefficiencies. The efficiency (η) is the ratio of the energy output from the solar cell to the input energy from the source illumination. Global solar cells are measured under AM1.5 conditions and at a temperature of 25 °C. Solar cells designed for a space use are measured under AM_0 conditions (*i.e.* for the solar radiation in space). The efficiency depends on parameters such as the absorption spectrum, the temperature of the solar cell and the intensity of the incident sunlight. The parameters of efficiency measurements must be controlled in order to compare the performance of different solar cells. The solar cell efficiency can be calculated as a fraction of the incident power which can be converted to electricity and is defined as:

$$P_{\max} = V_{OC} \times I_{SC} \times FF \quad \text{..... Equation 1.23}$$

The efficiency is defined as the ratio of the maximum power output ($P_{\max}$) to the power input (P_{in}), so the equation 1.23 becomes:

$$\eta = \frac{V_{OC} \times I_{SC} \times FF}{P_{in}} \quad \text{..... Equation 1.24}$$

η is the efficiency; V_{oc} is the open-circuit voltage; I_{sc} is the short-circuit current; and FF is the fill factor. The $V_{OC} \times I_{SC} \times FF$ corresponds to the maximum output power.

1.2.4 Drug Delivery

As the anodised nanotube has one open end, it can be used to carry drugs as a capsule for drug delivery. Moreover, the tubes may be filled with magnetic particles such as magnetite Fe_3O_4 and guided to desired locations. These tubes can also be coated

with proteins that can recognise viruses or cells which result a self-guided drug delivery. By use of suitable passivating molecules, the drug delivery can also be guided electrically (using voltage induced catalysis) and the drug release can be controlled by UV light, or X-ray, radiation for *in vivo* treatments through living tissue [110].

Song *et al,* [111] proposed the use of amphiphilic tube layers in a payload filling and release mechanism. These tubes had a hydrophobic cap to protect nanotubes loaded with hydrophilic drugs. The hydrophobic cap could be removed by photocatalytic oxidation, allowing aqueous body fluids to enter the tubes and flush out the desired drugs. Peng *et al* measured the kinetics of drug release. They found that the effective elution time controlled by the nanotubes varies with the size of the substrate molecules. Diffusion of small molecules takes some weeks and diffusion of large molecules perhaps a month [112].

1.3 Other Applications of TiO_2

In recent years interest in highly sensitive, selective and stable hydrogen sensors has increased rapidly [113, 114]. Metal oxide semiconductor-based gas sensors are simple and cheap to make [115]. Hydrogen sensors based on TiO_2 nanotubes show a superior H_2 response in air under bias conditions. It is believed that the selectivity towards hydrogen is directly related to the nanotube diameter. A smaller tube diameter gives higher sensitivity.

A thin layer of Pd was evaporated on to the surface of the TiO_2 film to form a device containing three layers; Pd, oxide film, and Ti at the base of the electrode [116]. The sensor output was determined by measuring the conductance through the TiO_2. This

specimen responded to 0.8 % H_2 in air or N_2 within a temperature range of 25-250 °C under bias condition. However, in a field application, the sensor can be easily contaminated. Nevertheless, after almost complete contamination by substances such as motor oil, the sensitivity can be restored by exposure to UV light. The 'self-cleaning' is due to the oxidation of organic contaminants by photo-generated electron-hole pairs on the TiO_2 surface. Approximately 2 wt% H_2 can be stored in TiO_2 nanotubes and 75% of the hydrogen stored can be released by reducing the pressure to ambient conditions [117].

TiO_2 is used also in self-cleaning building materials, antiseptic paints and coatings, the purification of air, and the decontamination of water from bacteria, organic compounds and viruses [118]. In addition, it is used in skin and stomach anticancer treatments [119].

Another important application of TiO_2 is in lithium ion batteries (LIB). The charge that can be stored, can be increased by reducing the dimensions of the TiO_2 from the bulk, through nanowires to nanotubes and nanoparticles [120]. A further increase in capacity can be achieved by the addition of carbon on TiO_2 or by loading the high capacity materials like RuO_2, SnO_2, ZnO and silicon onto the TiO_2 matrix to form composite materials [121].

1.4 Thesis Aims

In this study, the aim was to gain knowledge and understanding of the growth mechanism for TiO_2 nanotubes in order to achieve two targets: to control the

morphology of the nanostructures and to increase the performance of TiO_2 nanotubes in a range of applications.

The growth mechanism of TiO_2 nanotubes has been studied by time-dependent SEM, XPS and transient anodisation current analysis. Models to describe the growth process quantitively have been established. Understanding of the growth mechanism and precise control of the anodisation process are necessary to manipulate the morphology of TiO_2 nanotubes. The results of the catalytic behavior of hydroxide species on the initial porous growth are presented and the possible mechanism of localized anodisation is discussed. In a time-dependent scanning electron microscopy (SEM) study, the correlation with the transient current under potentiostatic conditions is also quantitatively analysed. This quantitative analysis, which has not previously been described improves the understanding of the early stages of the growth of anodic titanium oxide.

Two types of pre-pattern viz mechanical and EBL patterns have been developed and used on Ti surfaces in order to generate TiO_2 nanotubes with a new morphology.

The performance of nanotubes as a photocatalysts has been studied in a PEC for water splitting. Novel nanotubes have also been created, in order to demonstrate the influence of tube morphology on drug release kinetics.

We demonstrate a range of methods to control the morphology of the TiO_2 nanotubes for use in equipment for photocatalytic water splitting and in manipulation of the kinetics of drug release.

The challenge in the control of tube morphology through mechanical stirring and the magnetic effect is in the control of the shape of the vortex and the ion transportation. Nevertheless, we have proved that it is possible to control the morphology of nanotubes by direct manipulation of the ion flow direction.

Chapter 2 Experimental

2.1 Abstract

In this chapter the experimental set-up is described. Details of the anodizing unit and the material analysis techniques are presented. The general principles of electron microscopy (SEM and TEM), powder XRD and EBL are also summarised. Information, on the pre-treatment of Ti plates, including polishing and patterning, is given in later chapters of this thesis.

2.2 Sample Preparation

All chemicals used in this work were from sigma Aldrich. High purity titanium plates (0.5mm, 95%) were ultrasonicated in acetone and rinsed in DI water. The titanium samples were polished to a mirror-like surface with diamond pastes of 6, 3 and finally 1 μm. Between these steps the plates were ultrasonically cleaned in ethanol to remove residues. Finally the samples were cleaned by sonicating in acetone, then isopropanol, followed by rinsing with deionised water. For reuse the discarded film on the sample was removed by dissolution TiO_2 in a mixture of 1 wt% H_3PO_4 and 0.1 wt% HF (solution A) in the ultrasonic bath.

2.3 Anodising Unit

The anodisation was performed in a home-made electrochemical cell using clean Ti plates as cathode and anode. The anodizing voltage and electrode separation were kept constant. The surface area exposed to the electrolyte was about 2.0 cm^2. The

experiments were performed at room temperature or low temperature under aerated non-stirred conditions.

The transient anodisation current was recorded by a USB data logger (U12, Labjack). The experimental setup is shown in Figure 2.1.

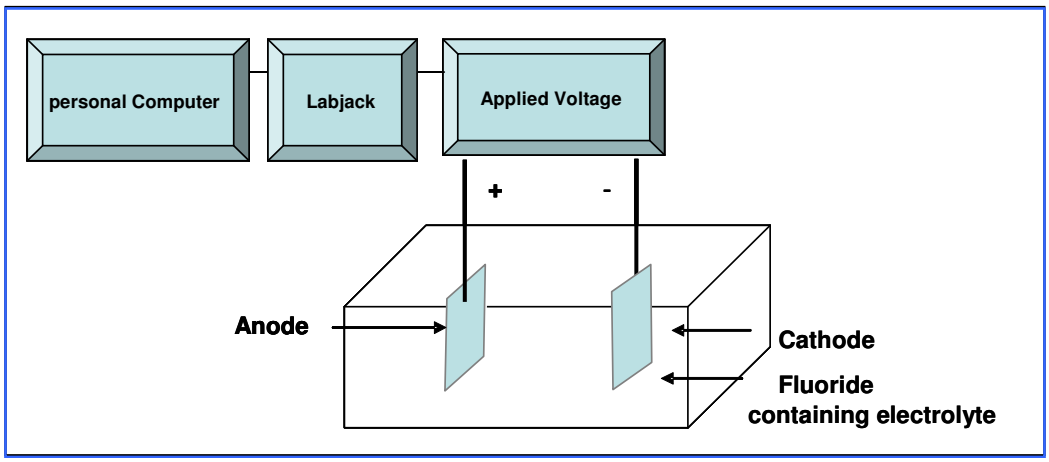

Figure 2.1 The anodizing unit with a two-electrode cell and applied voltage remotely controlled by a PC.

A power supply capable of operation as a constant voltage or constant current source was used for anodisation while the current was monitored by a personal computer (PC) through the USB data logger.

2.4 Characterisation by Electron Microscope Techniques

Most morphological information of as-prepared and annealed films was obtained by scanning electron microscopy (SEM) and transmission electron microscopy (TEM). Crystalline phases were characterised by TEM and by X-ray diffraction. Chemical information was obtained by X-ray photon spectroscopy (XPS) and energy dispersive

X-ray diffraction (EDX). Annealing was in the air to induce crystallisation. The following sections provide an overview of these techniques. Electron microscopy is like optical microscopy. However, instead of using photons, SEM uses a high-energy beam of electrons to interact with the atoms that make up the sample, producing signals, which contain information about the sample's surface composition and topography. The electron beam displays wave-like properties; a beam of 30 kV corresponds to a subnanometer wavelength so it can be used to extend the resolution of an optical microscope (~1 μm), which is limited by the wavelength of visible light. SEM and TEM are absolutely essential techniques in characterising the morphology and structure of nanomaterials. TEM is crucial in the examination of the early formation of the tubes during the anodising process, whereas SEM is essential in measuring the diameter and length of nanotubes in the later stages. In addition, TEM was used to identify the local crystal structures in the anodic film with selected area diffraction (SAED). Both techniques have been used extensively throughout this project to better understand all aspects of the titanium dioxide specimens. By using high operating voltages (200 kV), transmission electron microscopes can achieve a consistent resolution of the order of typical interatomic spacing in crystalline solids (0.15-0.5 nm). The TEM at Sussex has a limited resolution due to the low acceleration voltage (100 kV).

2.5 Scanning Electron Microscopy (SEM)

The development of SEM began in 1935 with the work of Max Knoll at the Technical University in Berlin. He placed a specimen within a modified cathode ray tube and scanned it with 100 μm electron beam with a diameter between 0.1 and 1 mm. Nowadays electron beam diameters of 3-10 nm are used [122].

In 1938 Manfred Von Adrienne, working in his private laboratory in Berlin, published an important theoretical paper which clearly explained the principle of SEM. Von Adrienne added scan coils to a transmission electron microscope that also possessed demagnifying lenses to produce an electron beam of a relatively small diameter. The instrument was really a scanning transmission electron microscope. However, the principle of scanning a small-diameter electron beam over the specimen was established. In Berlin the Second World War resulted in a break in the development of the scanning electron microscope [122].

In 1942 Zworykinn, Hiller and Snyder in United States developed the first scanning electron microscope that could study bulk specimens [122]. They recognised that secondary electron emission from the specimen surface illuminated with a high energy electron beam could be used to create topographic contrast. They used an electron multiplier detector to collect the secondary electrons at a bias of +50 V. An electron beam was focused by three electrostatic lenses with a diameter of 50 nm. The images that were obtained were noisy by today's standards, but they did confirm that the scanning electron microscope was practicable.

The modern SEM was developed by Sir Charles W. Oatley [123] and his students at Cambridge University in England from 1948 to 1961. The electron beam diameter was reduced to 20 nm, thus increasing signal to noise ratio. In 1965, the Cambridge Instrument Company was an immediate success and won the Queen's award for technology in that year.

In SEM, in contrast to TEM, it is inelastic scattering which provides information on the specimen to be analysed (inelastic scattering is dominant when the energy of the electron beam is in the range 10-30 kV). As the primary electron beam interacts with the sample, electrons lose energy either by scattering or absorption which take place within a defined specimen interaction volume that is 100 nm to around 5 μm into the surface, depending on the electron beam energy, the density of the specimen, and the atomic numbers of the atoms in it. A schematic view of an SEM instrument is shown in Figure 2.2.

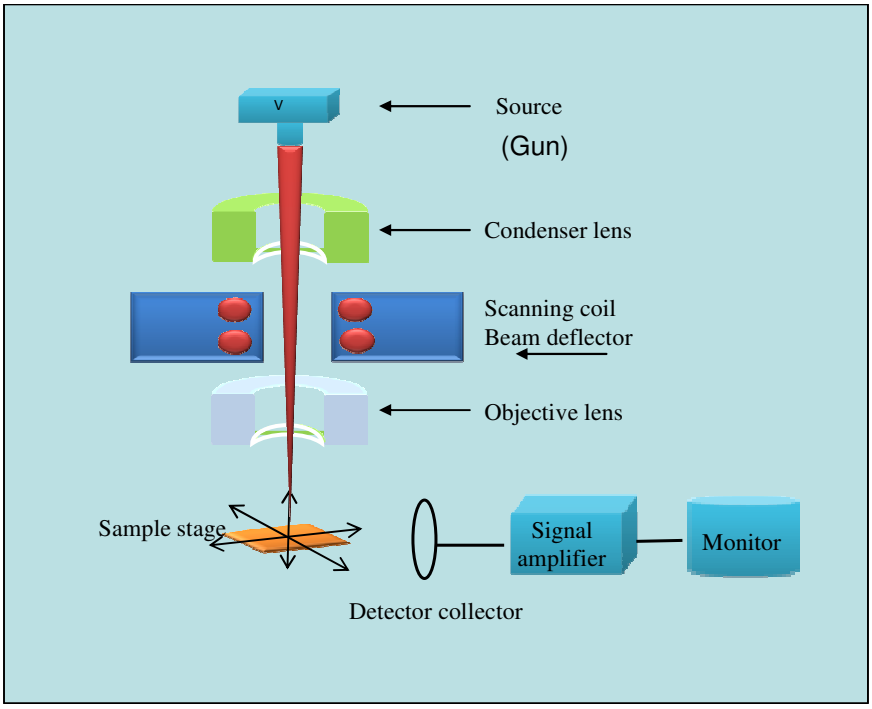

Figure 2.2 The scanning electron microscope

Various signals can be collected after inelastic interactions. Most commonly, detectors collect secondary electrons (providing information on the topography of the

surface), back-scattered electrons (showing the composition of the surface) and X-rays (giving elemental analysis of the sample).

A high energy electron beam is generated from the electron gun, accelerated at 10-30 kV and finely focused by a system of condenser lenses and a probe lens, on to the sample. The electromagnetic probe lens in SEM fulfils a similar function to the objective lens in TEM (its dimensions determine the resolution of the microscope), but, being placed above the specimen, it does not participate in the collection of the signal from the sample. As the beam is scanned over the sample by the action of scanning coils which deflect the beam horizontally and vertically (in the x and y directions), signals provided by secondary and back-scattered electrons are collected. This information is projected as an image on to a screen.

A full understanding of the effects of the machine variables is the key to producing the best SEM image of a specimen. Some important variables are; stigmatism, working distance, accelerating voltage and condenser lens current. Adjustments to the image can be made by changing these variables.

A scanning electron microscope needs to compromise between the need for a fine, probing, electron beam and the need to limit scattering, which increases with higher voltages. As a result, SEM operates within the range 1-30 kV and is consequently restricted to a maximum resolution of approximately 2 nm. In both TEM and SEM instruments, an electron gun (source) is used to generate a high energy electron beam by either thermionic emission from a W filament or field emission from a LaB_6 cathode

[124]. The electron beam is accelerated and focused through several electrostatic and electromagnetic lenses before reaching the sample.

In order to prevent the electron beam from being scattered by residual gas, to stabilise the electron gun, and to minimise beam-induced contamination of the sample, both systems are operated under a vacuum, of between 10^{-6} and 10^{-10} torr.

The electron beam-sample interaction signal is displayed on a viewing screen before a final image is produced. Although the principles are the same there are differences between SEM and TEM in the method of operation. In TEM the objective lens is used to focus the primary interaction signal before the image is enlarged by another set of imaging lenses. In contrast, in SEM a focused electron probe is used to scan the sample and a detector collects the resultant interaction signal as the electron beam moves. These variations allow the two techniques to yield vital information about the morphology and structure of the material being investigated.

2.5.1 Stigmatism and Resolution

The word stigma derived from Latin, means spot or point. The spot that is scanned over the sample needs to be as round as possible and is controlled by the stigmator control. A distortion of filament shape, a dirty aperture or contamination in the lenses, may cause distortion of the electron beam spot into an oval. Such distortion causes a reduction in resolution. An additional electromagnetic field is needed to compensate for such distortion [122].

2.5.2 Working Distance and Resolution

The distance between the final condenser lens and the sample to be analysed is called the working distance. A spherical aberration of the imaging system may be due to the geometry of the electromagnetic lenses but it can also be affected by the working distance. The electrons that travel at the inside of the electron beam are refracted less than those on the edges. The distance they have to travel exaggerates this difference, which creates more than one focal point to give an enlarged spot with unclear edges. A shorter working distance reduces adverse effects of spherical aberration, as it shrinks the spot striking the sample and improves the final resolution [122].

2.5.3 Working Distance and Depth of Field

The depth of field describes the distance within the sample that appears focused. The working distance greatly affects the depth of field. At a short working distance the depth of field is reduced because the sample is scanned with a wide cone of electrons. At a greater working distance the cone of electrons becomes narrower and the depth of field is increased. The relationship is illustrated in Figure 2.3. However, use of a longer working distance compromises the resolution, as discussed in section 2.5.2.

The features of a sample dictate the balance between distance and depth of field required to create useful images. A sample with large topographical variation may need a greater depth of field, achieved through a greater working distance, but may not have the optimum resolution. A relatively flat sample on the other hand can give better resolution as the depth of field is less important and a shorter working distance can be employed [125]. The optimal working distance for the Jeol 820 SEM is between 8 and 10 mm.

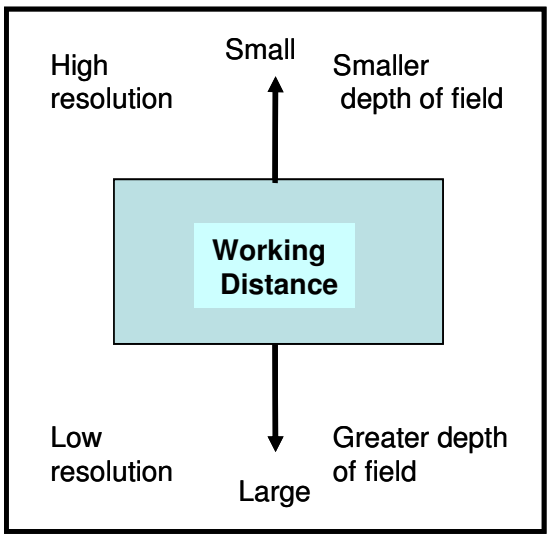

Figure 2.3 The effect of working distance on the depth of field and the resolution [125].

2.5.4 Accelerating Voltage and Resolution

The high voltage applied to the filament is used to accelerate the electron beam. The combination of this high voltage with the heating current causes electrons to leave the filament. An accelerating voltage of between 5-30 kV is typically used in SEM imaging. The advantage of a higher accelerating voltage is that it decreases the spherical aberration of the system and thereby increases resolution. However, a higher acceleration voltage increases the beam-sample interaction and can cause charging effects for insulating and semi-insulating samples. The greater energy of the electrons increases the interaction volume between beam and specimen and reduces the resolution, particularly for samples with low atomic number such as biological specimens. Figure 2.4 describes the influence of accelerating voltage on the resolution of the image [122, 125].

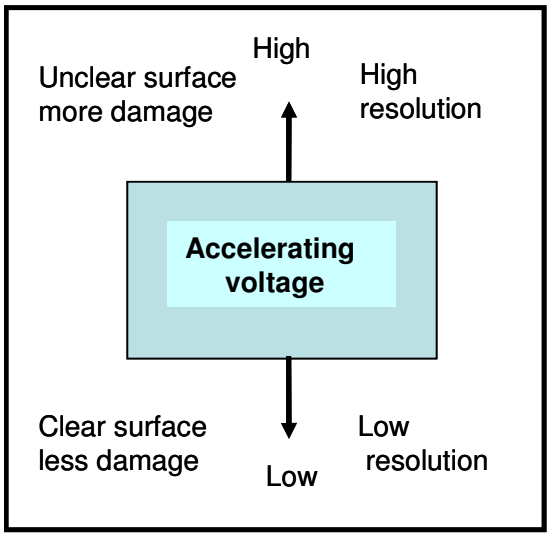

Figure 2.4 The influence of accelerating voltage on the image resolution [125].

In addition, it is important to consider the probe current setting; Figure 2.5 shows the relationship between probe current and image resolution.

Usually, in order to achieve high resolution, a low probe current with a low probe diameter is required. The influence of the probe current on the probe diameter is determined by the space charge effects, originating from repulsive interactions between electrons. High acceleration voltages reduce space charge effects. In general, it is necessary to select a probe current suited to the magnification and observation conditions (accelerating voltage, specimen tilt, etc.) as well as the specimen.

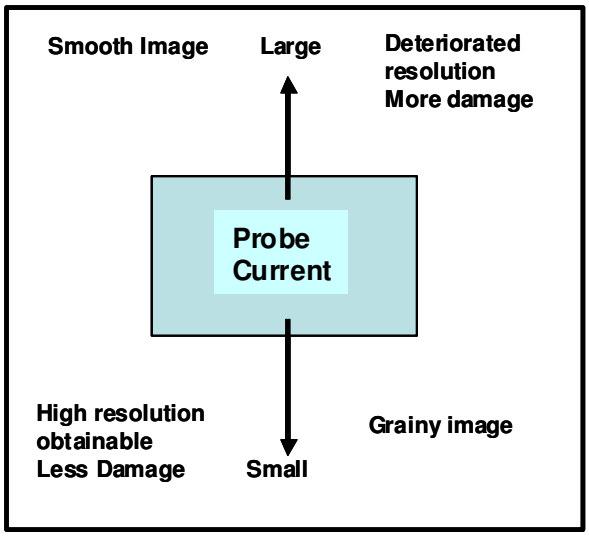

Figure 2.5 The relationship between the probe current and the resolution [125].

2.5.5 Preparation of SEM Specimens of Anodised TiO_2

A voltage between 10 and 30 kV was used for the measurements, with a various working distances. For example, for top-view imaging a working distance between 8 and 10 mm can be used. However, working distances of 15-18 mm can be used for the side views (tilted samples). At higher voltages higher resolution can be achieved from the reduction of spherical aberration. Nevertheless, the interaction volume is also increased at higher voltages; resulting in a loss of resolution. Therefore, a compromise has to be made.

Both conducting and non-conducting specimens can be examined by SEM. The final image is affected by the negative charge from the electron beam, which accumulates when using nonconductive sample. These effects appear either as abnormal contrast or as abnormal lines, which cause shifts within the image. Almost all biological samples are nonconductive, so to obtain good images it is necessary to coat them with a thin layer of metal (such as gold) or carbon, making the surface conductive. Samples like metals and most semiconductors are conductive and can be examined without

coatings. For TiO_2 samples, no obvious charging effects were observed so no additional coatings (for example Au) on titanium nanotubes arrays were required.

2.5.5.1 The Secondary Electron Image (SEI)

Various signals are generated within SEM by sample-beam interaction. These include secondary electrons, back-scattered electrons, characteristic X-rays, light (cathodoluminescence), specimen current, and transmitted electrons. A range of surface properties can be extracted by studying these signals.

The SEI is the most commonly used signal in SEM. Secondary electrons are low energy electrons (typically 10-300 eV) which are emitted from less than 10 nm deep within the excited surface layer and therefore provide topographic details of the surface. A secondary electron is generated through a Auger process. When an atom is illuminated by a high energy electron beam, it is ionized by losing an electron at core level. The relaxation of an upper level electron causes the emission of another electron. This electron is called an Auger electron and it is captured by a scintillator that converts the electron beam intensity to fluorescent light that is captured by photomultiplier. A detector is kept at a “post acceleration voltage” of 1 kV to collect the secondary electrons and to exclude primary elastic electrons. This is the principle of secondary electron detection. In a back-scattering process, the elastic electron is scattered by the sample. The number of secondary electrons generated depends on the tilt angle of specimen and is greater at a greater angle. The image is typical of shadowless illumination, as it is created by the collection of electrons emitted in all directions. Also, the high depth of field achievable by SEM allows one to obtain three-dimensional perspectives of the analyzed specimen.

The intensity of the back-scattered electrons is related to the density of the sample and the atomic number of the atoms in it. It is therefore gives additional contrast due the difference in atomic species.

The highest resolution in SEM (1-2 nm) is achieved under optimal conditions (working distance, accelerating voltage) working in the secondary electron image mode.

2.6 Energy Dispersive X-ray Spectroscopy (EDX)

In addition to secondary electron and back scattering electron detection, SEM can also be used to identify elements based on X-ray fluorescence. A hole is created at the core level in atoms by excitation by the high energy electron beam. The relaxation of an electron in a higher level to the hole in the core level causes the emission of X-rays. The energy of the emitted X-ray is specific for each atom and can be used to determine chemical composition. The intensity of such fluorescence is proportional to the amount of the element in the sample. In this project we use a combination of secondary electron and X-ray fluorescence to characterize the nanostructured samples.

2.7 Transmission Electron Microscopy (TEM)

Morphological investigations have also been carried out by TEM by use of a Hitachi-7100 instrument, which is operated with a tungsten filament and a voltage range of 40-120 kV. The sample preparation for TEM involves the removal of the anodic layer from titanium metal followed by mechanical cracking by a pair of special tweezers. Very small sections of material were separated from the anodic film and directly mounted in a double-layer 200 mesh copper grid. The sections mounted were usually thin enough to permit good quality transmission of the electron beam. The

transmission electron microscope forms a true image of the specimen, as does the light microscope. The best image is formed when the specimen is illuminated with electrons or light photons and with some of the radiation absorbed by the specimen. The condenser aperture restricts the size of the beam to reduce unnecessary illumination of the specimen, since electron beams damage materials to some extent. The sample itself has to be very thin (around 100 nm) so that most of the electrons can pass through it without significant inelastic scattering [126]. Figure 2.6 shows how a TEM instrument works.

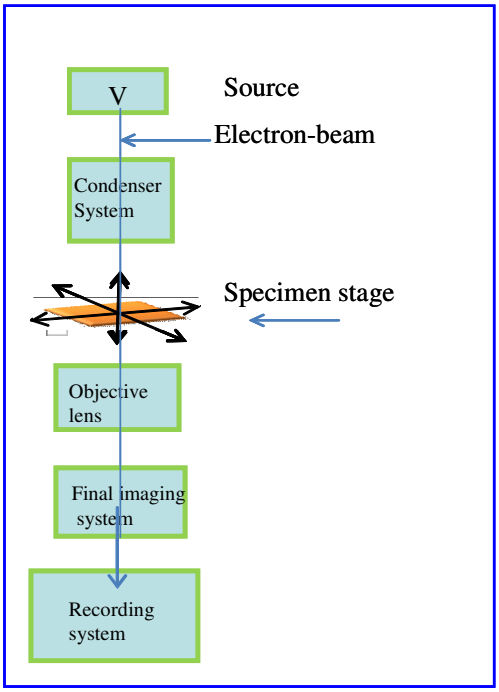

Figure 2.6 The transmission electron microscope.

2.8 X-Ray Diffraction

Crystal structures of nanomaterials can be identified by use of an X-ray diffractometer. Diffraction techniques depend on the interference between waves reflected from the periodic arrangement of atoms within the crystal [127]. For powder

diffraction, the spacing between sets of crystal planes is characterised by a specific diffraction angle. Figure 2.7 shows the geometry of an X-ray diffractometer. The setting of the detector follows the diffraction angle which is determined by the spacing between the layers. The Bragg equation (Eqn 2.1), relates the diffraction angle θ at which intensity can be observed to the spacing d between the planes for a specific X-ray wavelength.

$$n\lambda = 2d \sin\theta \quad \text{..... Equation 2.1}$$

where, λ is the wavelength of the X-rays, typically about 100 pm (1 pm = 10^{-12} m).

d is the spacing between the planes in the atomic lattice, θ is the angle between the incident ray beam and the scattering planes.

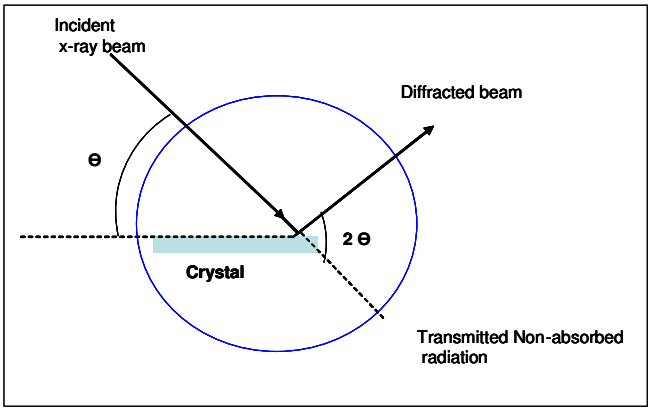

Figure 2.7 X-ray diffraction by the crystal lattice.

In this project, a Simens D500 X-ray diffractometer, with Cu-K_α radiation of wavelength 1.54056 Å was employed for the characterization of the anodized samples such as polygonal and circular nanotubular arrays. The detector angle is measured relative to the incident X-ray beam. The D500 allows a θ/2θ scan, in which both the

incident and detector angles relative to the sample plane are changed simultaneously. In a second mode, the incident angle can be fixed while the detection angle is changed. For the normal powder sample analysis, we use a $\theta/2\theta$ scan, and for a thin film sample, we fix a small incident angle (θ = 4º) and move the detector. With a small incident angle, the X-ray beam samples a shallow depth into the material so the procedure is suitable for thin film analysis. For anatase and rutile, the unit cell vectors (*a*, *b* and *c*) and the symmetry of the crystal determine the spacing of individual crystal planes. Table 2.1 lists the Miller indices, *d* spacing, diffraction angle 2θ and relative diffraction intensities of low index crystal planes [128]. The XRD data for anatase and rutile were taken from a standard spectrum [129]. This standard data was used to determine the crystal phases of TiO_2 nanotubes. The typical thickness of the anodised TiO_2 was >1 µm and both $\theta/2\theta$ and 2θ scans were used.

Table 2.1 Shows anatase and rutile diffraction patterns [128].
Anatase

h	*k*	*l*	*D*	*2Θ*	*I*
1	0	1	3.5163	25.308	100.0
1	0	3	2.4307	36.950	6.5
0	0	4	2.3786	37.790	20.3
1	1	2	2.3322	38.571	7.4
2	0	0	1.8921	48.046	28.2
1	0	5	1.7001	53.884	18.1
2	1	1	1.6662	55.071	17.8
2	1	3	1.4931	62.115	3.1
2	0	4	1.4808	62.690	13.9
1	1	6	1.3642	68.754	6.2
2	2	0	1.3379	70.302	6.8
2	1	5	1.2646	75.051	10.5
3	0	1	1.2505	76.049	9.8

Rutile

h	*k*	*l*	*D*	*2Θ*	*I*
1	1	0	3.2477	27.440	100.0
1	0	1	2.4875	36.078	46.0
2	0	0	2.2965	39.196	7.1
1	1	1	2.1873	41.239	18.0
2	1	0	2.0541	44.049	6.5
2	1	1	1.6874	54.323	56.0
2	2	0	1.6239	56.634	16.5
0	0	2	1.4795	62.750	7.8
3	1	0	1.4524	64.057	8.1
3	0	1	1.3598	69.001	19.6
1	1	2	1.3464	69.795	9.8
3	1	1	1.3038	72.425	1.0
2	0	2	1.2437	76.534	2.2
2	1	2	1.2005	79.827	1.1

2.9 The photoelectrochemical Cell (PEC)

Photoelectrolysis is a broad term describing semiconductor-based water splitting by the use of a photoelectrochemical cell (PEC) [14, 19, 94, 100, 130-132]. In my experiments a 300 W xenon arc lamp was used as a light source. A platinum electrode was used as the counter electrode and a saturated Ag/AgCl electrode was used as a reference electrode. The 100 ml of 1M KOH solution in DI water acted as the electrolyte during water electrolysis. A USB controlled potentiostat (EA163 from eDAQ) was used to control the electrochemical potential and to measure the photocurrent. The setup of the PEC is illustrated in Figure. 2.8. A lens was inserted between the photoanode and the light source to focus the beam size to 1 cm^2. Substrates formed with TiO_2 nanotubes arrays with different morphologies and crystal structures were used as a photoanode. In this study two different TiO_2 nanotube morphologies, circular and polygonal, were investigated to examine their potential applications in the PEC water splitting.

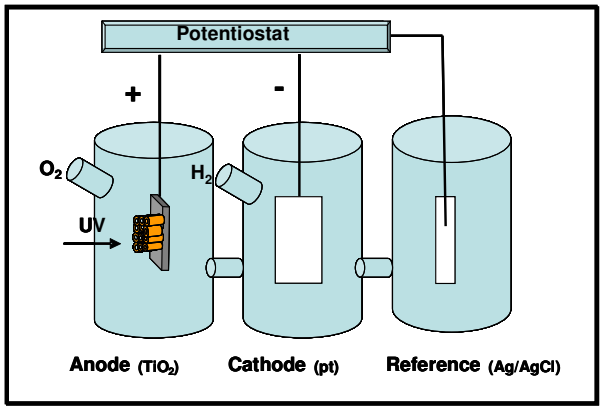

Figure 2.8 Water splitting cell with TiO_2 nanotubes (polygonal and circular) as a photoanode, platinum cathode and Ag/AgCl reference electrode. Hydrogen forms at the cathode. Oxygen forms at the anode. The electrolyte is 1M KOH.

Upon light illumination, hydrogen ions migrate in the electrolyte and electrons in the external circuit [94]. Gaseous oxygen evolves at the photoanode and the hydrogen ions move to the cathode through the aqueous electrolyte (internal circuit). Simultaneously, electrons, generated as a result of photoexcitation at the anode, are transferred over the external circuit to the cathode, resulting in the reduction of protons into gaseous hydrogen. Both the anode and cathode are connected to the EA163 potentiostat through stainless steel crocodile clips.

2.10 Annealing

The TiO_2 nanotubes prepared by anodisation normally contain some residual organic solvent and are generally amorphous. The formation of specific crystal phases is critical to improve charge carrier mobility and to reduce recombination. The anodised samples were therefore annealed to certain temperature. The residual organics are removed at temperatures above 260 °C. The annealing of the anodised titania film was studied with SEM, TEM and XRD, followed by PEC water splitting measurements. The nanotube arrays were annealed in a tube furnace (CARBOLITE PAT 3081) 100 °C to 650 °C with heating rate of 20 °C/minute for 2 hours and then allowed to cool at approximately 20 °C/minute.

2.11 Electron Beam Lithography (EBL)

In electron beam lithography (EBL) a finely focused high-energy electron beam is used to write a defined pattern across a surface covered with a photoresist. Our EBL involved the use of the Jeol 820 m SEM instrument, in which the sample can be manually moved in both *X* and *Y* directions with a readable resolution of 0.5 µm.

A modern dedicated EBL system would control the movement of the electron beam with automatic PC software. From such systems, researchers have used this technique to write patterns with widths of just a few nanometers in a layer of photoresist on polished silicon substrates [133]. With our manual control; we were limited to simple linear and square patterns, but there were sufficient for our purpose.

Photoresist materials are organic compounds whose chemical properties change when they are exposed to UV light due to breaking of chemical bonds. When the exposed region becomes more soluble in the developer, the organic compound is called positive resist. In other words, "whatever shows, goes." The mask, therefore, contains an exact copy of the pattern which remains on the wafer. For example, polymethylmethacrylate (PMMA) is one of the common positive resists [134].

When the exposed region becomes less soluble in the developer, the compound is called a negative resist (for example SU-8). For instance, polystyrene [135] is used as a negative photoresist and all solvents that can dissolve un-exposed polystyrene can be used as developers. It is often used in applications where a permanent resist pattern (one that is not strippable, and can be used in high temperature and pressure environments) is needed for a device [136]. Upon exposure to UV light, negative resists convert into polymer that is not easy to break up and remains on the surface after exposure. The developer solution removes only the unexposed portions. If a photo mask is used, an inversed (or photographic "negative") pattern is transferred.

The differences between photoresists [136] are summarized in Table 2.2.

Table 2.2 Differences between the photoresists [136].

Characteristic	Positive	Negative
Adhesion to Silicon	Fair	Excellent
Relative Cost	More Expensive	Less Expensive
Developer Base	Aqueous	Organic
Minimum Feature	0.5 μm and below	± 2 μm
Step Coverage	Better	Lower
Wet Chemical Resistance	Fair	Excellent

Our lithographic process involved three steps. First, by the exposure of positive resists to the electron beam, two fine-lined patterns were drawn on to PMMA to form a grid. Secondly, the resist was developed with a mixture of methyl isobutyl ketone (MIBK) and isopropanol (IPA). The anodisation process was then carried out on the patterned titanium plates.

Chapter 3 A New Approach to the Catalytic Growth of Anodised TiO_2 Nanotubes

3.1 Abstract

In the present work a Ti plate was pre-covered with hydroxide islands using acid treatment. With time-dependent SEM observations, I was able to show that the initial etch pits are exclusively located at the interface between the hydroxide islands and Ti substrate. This leads to the postulate that Ti^{3+} at the interface between hydroxide and the Ti substrate plays a significant role at the early stage of anodisation. There is significant rearrangement of hydroxide coated islands following the formation of nanotubes. The presence of the hydroxide eliminates the release of O_2 gas during the anodisation. The variation of the current with time shows four distinct stages in the growth process. It was found that a cubic equation fits the increase in the current after the initial exponential decay. A dissolution process has also been identified towards the end of the anodisation. Anodisation parameters such voltage, fluoride concentration, stirring and the effect of magnetic fields have been investigated.

3.2 Introduction

Titanium dioxide is one of the most widely studied oxide semiconductors due to its photocatalytic activity [3, 12, 51], biocompatibility [137] and stability in water [13]. Moreover, modifying the microstructures and controlling the electronic structure of the

TiO_2 can potentially improve the efficiency of its application in photovoltaic devices [47, 51, 138-140].

TiO_2 nanotubes are of great interest among the various known titania nanostructures. To date, the most effective way of creating vertically aligned TiO_2 nanotubular arrays is by anodizing a Ti plate, in a similar manner to the process for fabricating anodic aluminium oxide (AAO) [141], but using different electrolytes containing fluoride [2, 12, 37-39, 51, 142, 143]. Successful attempts have been reported to control the geometry, the diameter [143, 144], length [140, 145], wall thickness [146] and even the external structures of the aligned nanotubes [147] by manipulating the anodizing conditions. More recent efforts have been focused on establishing the growth mechanism with the aim of fine tuning the nanotube morphology. Microstructural studies of AAO and anodic titanium oxide (ATO) have been performed in order to understand this mechanism [147].

Qualitative description [143] and quantitative modelling of the electric field distribution [148] and growth process [149] have also been established. However, knowledge about the early stages of pore growth in AAO and ATO is still very limited [150].

3.3 Experimental Details

Samples were prepared as described in chapter 2 section 2.2. Hydroxide islands were created by dipping polished Ti plates in an acid solution (solution A), for 5 min, followed by sonicating in DI water for 4 min. H_3PO_4 was used to adjust the pH of the solution to 1.5, and F^- was added to initiate the formation of a hydroxide layer. A longer

dipping time forms a much rougher surface, 4 min contact with the solution was optimal to achieve an appropriate density of hydroxide islands.

The anodisation was performed in a home-made electrochemical cell with a clean Ti plate as cathode. The electrolyte contained 0.6 wt% ammonium fluoride (analytical grade) and 2 wt% DI water. The anodizing voltage was kept constant at 60 V DC with an electrode separation of 65 mm. The surface area exposed to the electrolyte was about 2.0 cm^2. The experiments were performed at room temperature under aerated non-stirred conditions.

The current-time profile was recorded using a USB data logger (U12, Labjack). The formation of a hydroxide catalytic layer and the evolution of TiO_2 nanotubes were monitored by SEM (JSM 820M, Jeol) and TEM (Hitachi-7100), operating at 100 kV. X-ray photoelectron spectroscopic data were recorded with a 12 keV bias and 10 mA emission current. The 2p signals from the clean Ti sample were used to calibrate the equipment.

3.4 Results and Discussion

Figure 3.1 shows the typical morphology of anodized Ti in electrolytes containing fluoride. The SEM images show the circular cross sections of the nanotubular arrays (a) from the top, (b) from the bottom and (c) from the side. The nanotubes are open at the top (Figure 3.1a) and closed at the bottom with an average outer diameter of 120 nm. In Figure 3.1b a dark region is visible in the middle of each nanotube probably reflecting the hollow tubular structure. Similar images were observed by Chen *et al*, recently [151]. The profile view (Figure 3.1c) shows that the straight nanotubes have almost

equal length of approximately 2.5 µm. The TEM image, (Figure 3.1d) gives the detailed morphology of the individual nanotubes with a smooth wall structure.

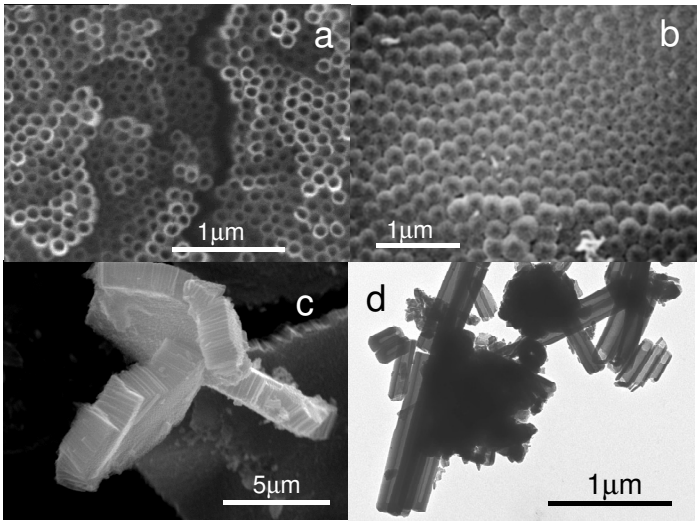

Figure 3.1 SEM images of the (a) top view (b) the bottom view and (c) side view of TiO_2 nanotubular arrays. The layer was grown on a Ti substrate pre-treated with an acid (solution A) in water for 5 min followed by 45 min anodisation in water for 5 min followed by 45 min anodisation in ethylene glycol containing 0.6 wt% ammonium fluoride and 2 wt% water. The TEM image (d) shows the internal structural details of the same nanotubes.

In the following sections, we focus on the mechanism of the early growth of TiO_2 nanotubes.

3.4.1 Creating the Catalytic Hydroxide Layer

After fine mechanical polishing of the Ti plate with 100 nm diamond paste, the surface has a mirror finish. Ultrasonic cleaning of the polished sample with isopropanol and water has no effect on the surface. At this stage, the sample is extremely hydrophobic. The SEM image in Figure 3.2a shows a typical example of such a surface,

which is very smooth with a low density of defects. The defects are dominated by polishing grooves with a width of 100 nm.

When the polished sample is dipped into the acidic solution (solution A) gas bubbles are formed on the surface. These are attributed to H_2; its evolution is accompanied by the oxidation of the Ti. SEM images in Figure 3.2b and 3.2c show the evolution of the surface morphology, recorded after 30 sec and 90 sec in contact with the acidic solution. The acid-induced Ti corrosion and the formation of hydroxide island, on the smooth surface can be clearly identified. After 90 sec, the surface became extremely rough. The sample was then rinsed with DI water and cleaned in water in the ultrasonic bath for 5 min. The morphology of the surface at this stage is shown in Figure 3.2d.

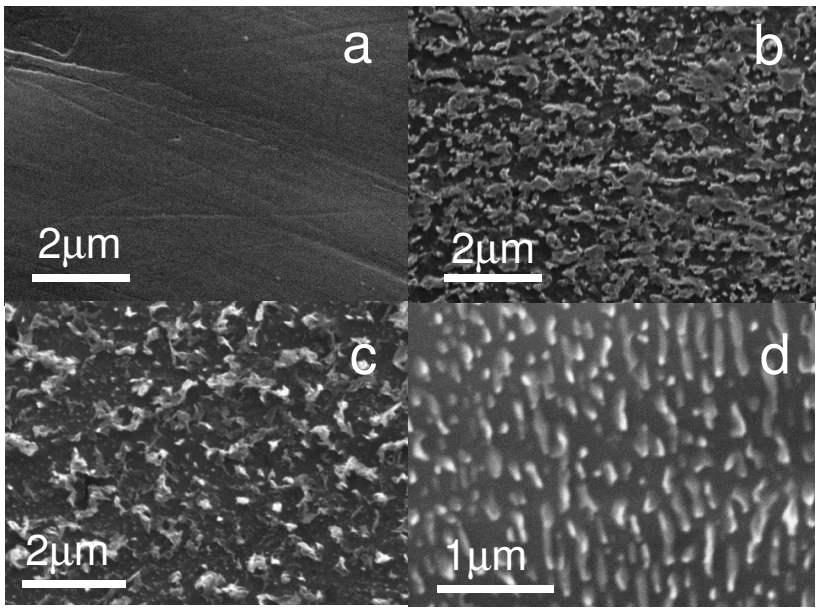

Figure 3.2 (a) The polished Ti sample, (b) the surface after 30 s acid treatment, (c) after 90 s acid treatment and (d) after acid treatment for 90 s followed by ultrasonic cleaning in water.

Many smooth discrete islands are formed with regular size and shape, possibly in the form of titanoic acid [TiO_x $(OH)_{4-2x}$]. The XPS study, shown in Figure 3.3, shows two components in the O 1s peak with binding energy at 531.5 and 530.1 eV, attributed to from hydroxide and oxide respectively. No significant fluorine 1s XPS signal is found at 584.8 eV. The spectra have been fitted to a linear background and a linear combination of Gaussian and Lorentzian peak shapes, similar analysis have been made by of these TiO_2 nanotubes [152]. However, we have noticed that the relative intensity of the hydroxide against the oxide is much higher on our acid-treated surface than that found on other TiO_2 nanotubes [152].

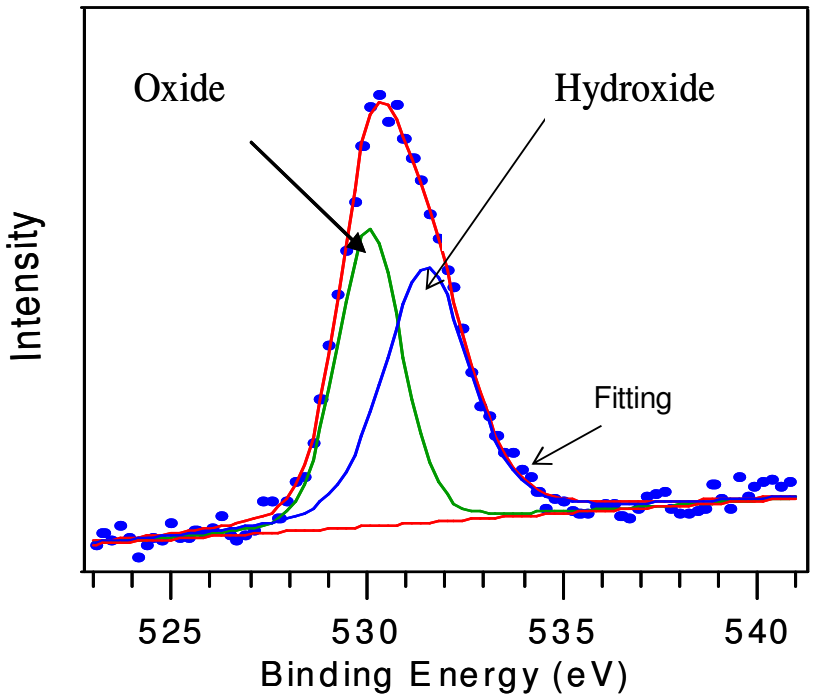

Figure 3.3 O 1s XPS spectrum of the acid-treated Ti sample.

During the anodisation, a photoimage was taken of a Ti anode containing both acid treated and polished parts, as seen in Figure 3.4. It seemed that the polished part in

general was very shiny compared with the grey part that had been dipped in acid. During the anodisation, O_2 bubbles were visible on the polished sample (right side) but the acid-treated part had no O_2 bubbles. Instead a rapid colour change was observed. This colour change indicates the immediate formation of a thin oxide film which has a thickness similar to the wavelength of visible light (400~1000 nm). The rapid growth suggests that the preformed hydroxide island from acid treatment catalytically accelerate the anodisation.

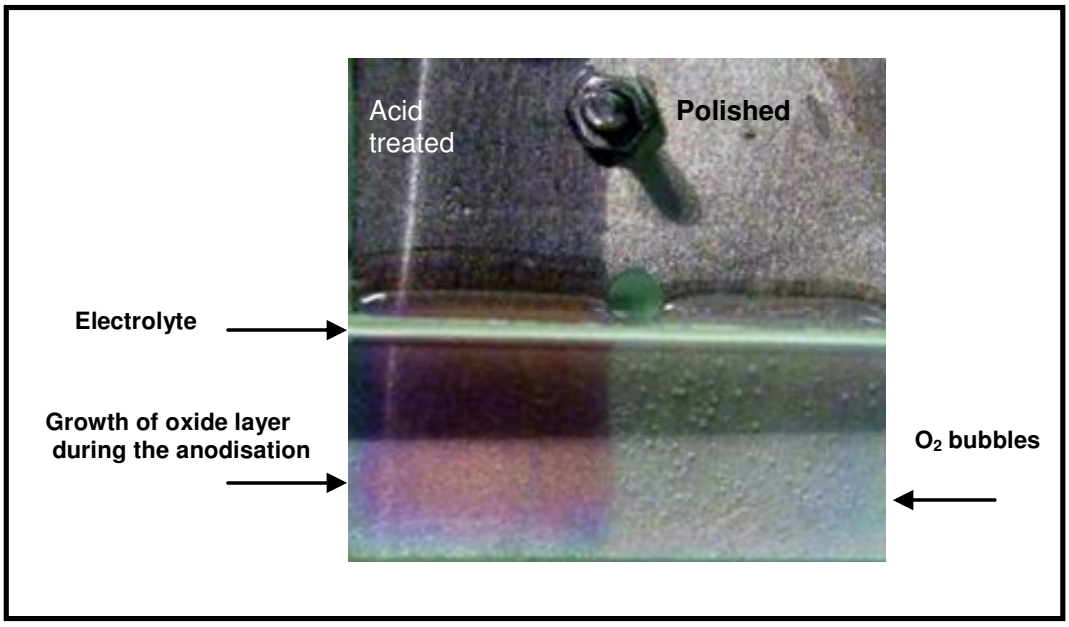

Figure 3.4 The photoimage of polished and acid-treated parts of a Ti sample. Half the sample was dipped into the electrolyte.

3.4.2 Contact Angle Measurements

The acid treatment was also monitored by contact angle measurements shown in Figure 3.5 as a function of time in the acid solution at room temperature. A low contact

angle indicates a highly hydrophilic surface. A polished titanium plate was dipped in solution A and the water contact angle was measured after each dip after 15 s. The experimental part of the contact angle measurement will be described in detail in chapter six. The polished Ti plate has the highest contact angle of 62˚. The measured water contact angle decreases rapidly in the first 20 sec of dipping and reaches its minimum after 3 min of dipping. By then, a complete covering of the surface with Ti hydroxide has been formed.

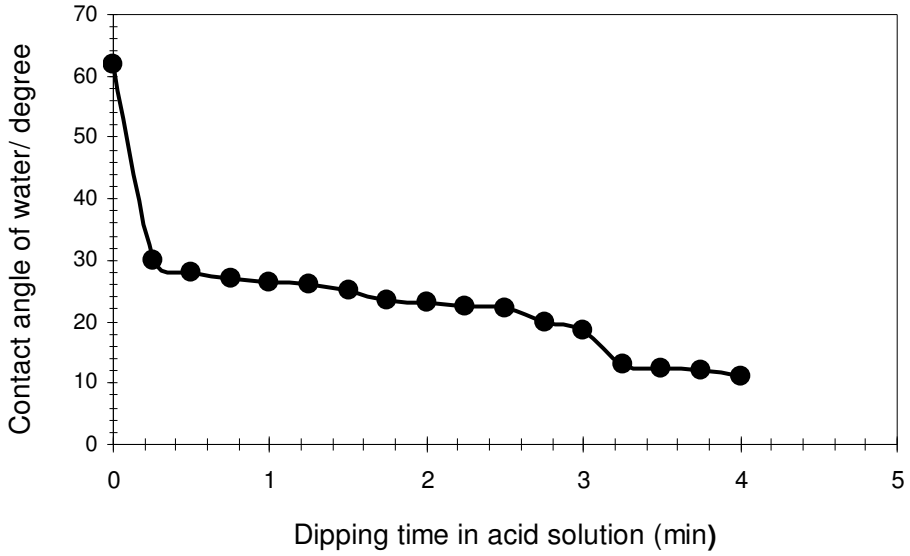

Figure 3.5 The effect of the dip time in acid solution on water contact angle.

Dipping in the acid solution forms hydroxide layers which are hydrophilic. A schematic diagram of this phenomenon is shown in Figure 3.6. The hydroxide on the titanium surface; changes the surface properties from hydrophobic to hydrophilic, so the contact angle decreases.

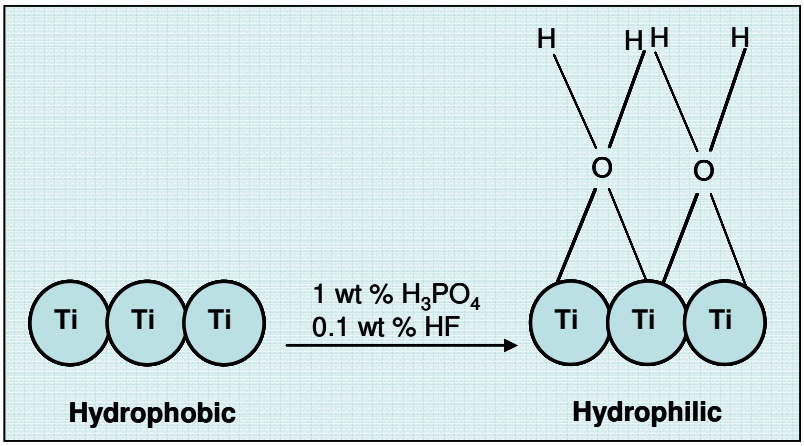

Figure 3.6 The suggested mechanism of the titanium surface wetting.

3.4.3 Time Dependent SEM Study at Different Stages of Anodisation

In order to understand the effect of preformed hydroxide islands on the growth of nanotubes, we monitored the evolution of the sample morphology at each stage of the anodisation. Figure 3.7 shows a sequence of SEM images taken from acid treated plates anodized for different lengths of time. Each sample was prepared individually but under identical conditions. As shown in Figure 3.7a, fine etch pits were formed as early as 45 s into the anodisation. The etch pits were exclusively located at the boundaries between the preformed hydroxide nano-islands and the thin metal oxide film formed in the anodisation. This suggests that the activation energy for creation of the etching pits is low. The shapes of some etch pits follow the profile of the islands rather than being perfectly circular. The oxidation of Ti and dissolution of oxide are faster than on the clean metal surface.

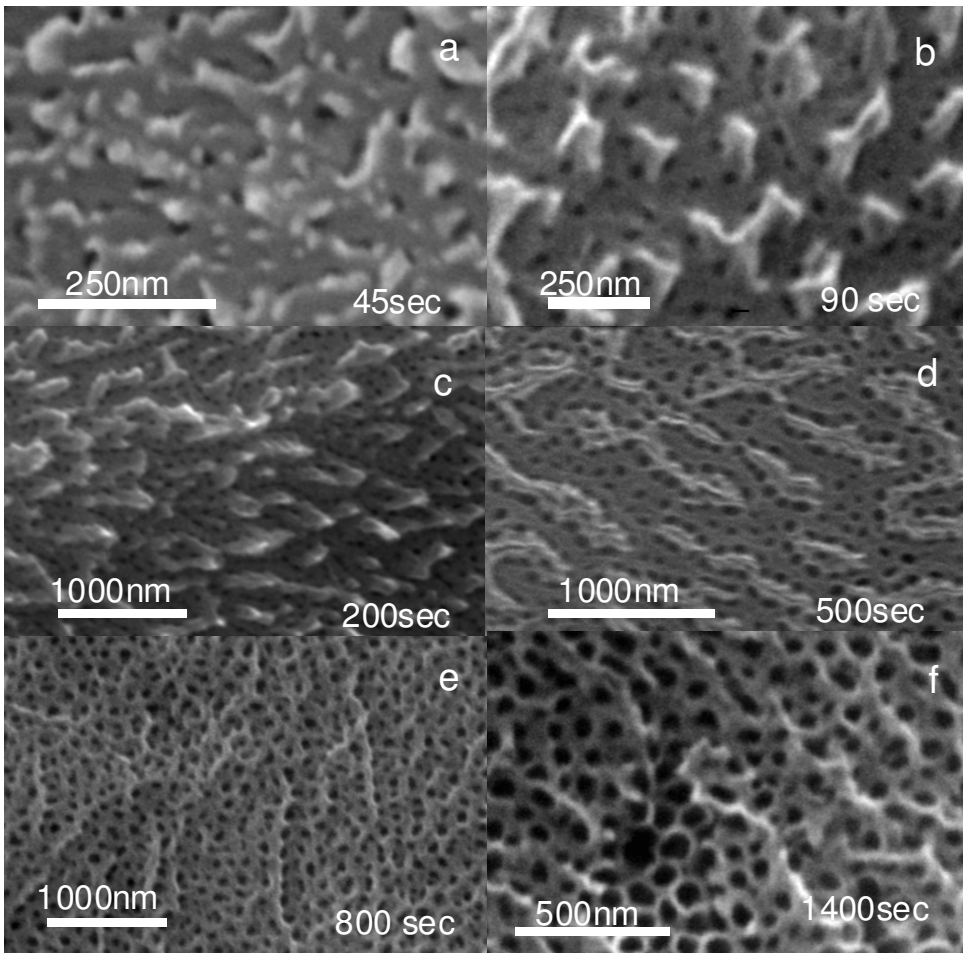

Figure 3.7 SEM images from an acid-treated Ti plate anodized for different times.

One of the possible mechanisms for this pattern of etching is that subvalent cations such as Ti^{3+} associated with oxygen vacancies are concentrated at the interfaces between metal and metal hydroxide. The oxidation of Ti^{3+} to Ti^{4+} has a low polarization potential so it is kinetically favourable. The oxidation of Ti^{3+} to Ti^{4+} requires oxygen species from dissociation of water, as in equation 3.1.

$$Ti_2O_3 + H_2O \xrightarrow{-2e} 2TiO_2 + 2H^+ \quad \text{Equation 3.1}$$

Such oxidation increases the local concentration of H^+ which promotes the dissolution of formed TiO_2. Alternatively, the presence of hydroxide islands gives an inhomogeneous distribution of the electric field. The field at such interfaces is much

stronger than that on the flat surface and drives the initiation of the etch pits. Such a focused field could attract F^- anions moving towards the hydroxide island on the anode. In contrast on a polished Ti plate, there is no such hydroxide island and electrochemical potential is directly applied across the metal/electrolyte interfaces. The electrochemical process is dominated by the electrolysis of water and the formation of O_2 gas on the anode surface. The anodisation efficiency is much lower than that on acid-treated surfaces.

The ability of F^- to form soluble species, such as TiF_6^{-2}, leads to permanent chemical attack on TiO_2 (dissolution) and prevents passivation by titanoic acid $TiO_x(OH)_{4-2x}$ precipitation. Figure 3.7b shows the SEM image of the surface after 90 s anodisation. The density and diameter of the etching pits have increased while some etching pits start to develop in the areas between the hydroxide islands. At this stage, the average pore diameter is about 30 ± 8 nm (averaged over 65 pores). Nevertheless, the shape of the pore is still irregular. Further anodizing creates more etch pits with slightly increased diameter, 40 ± 8 nm, as shown in Figure 3.7c. More significantly, as the dimension of the nanopore increases, the number of such pores decreases between 200 and 500 s. This suggests that there is a merging of nearest pores as they become bigger. At 1400 s, an almost perfect distribution of nanotubes can be observed on some parts of the image (middle bottom). To further understanding of the growth behavior of the TiO_2 nanotubes, the diameter and number of pores, together with the oxide film thickness as a function of anodisation time were also measured from the SEM images, shown in Figure 3.8a and b.

It is clear that, in the early stage of anodisation, both the film thickness and the pore diameter increase linearly with time, and the number of pores reaches its maximum value of 180 μm^{-2} at 250 s, as shown in Figure 3.8a. This gives quantitative evidence of the merging of the pore structures. After 1200 s, nanotubes with the maximum diameter are achieved, which indicates the transition from nanopores to nanotubes. Combining this profile for the number of pores together with that for the pore diameter, one can slow that the maximum surface area is achieved around 250 s. The oxide film thickness was measured from the cross sectional view of the SEM image. Here, we are only able to identify the overall thickness rather than detailed information, such as oxide barrier layer thickness and nanotube length. Nevertheless, it is worth mentioning that the thickness of the oxide film increases almost linearly for 1200 s from the beginning of the anodisation, after that the growth rate gradually decreases, shown in Figure. 3.8b. This could be due to the slowing of the oxidation rate at the bottom of the nanotubes or increasing dissolution at the top. Since the anodisation current does not show a significant decrease, we can conclude that the decrease in the growth rate is likely to be the result of dissolution.

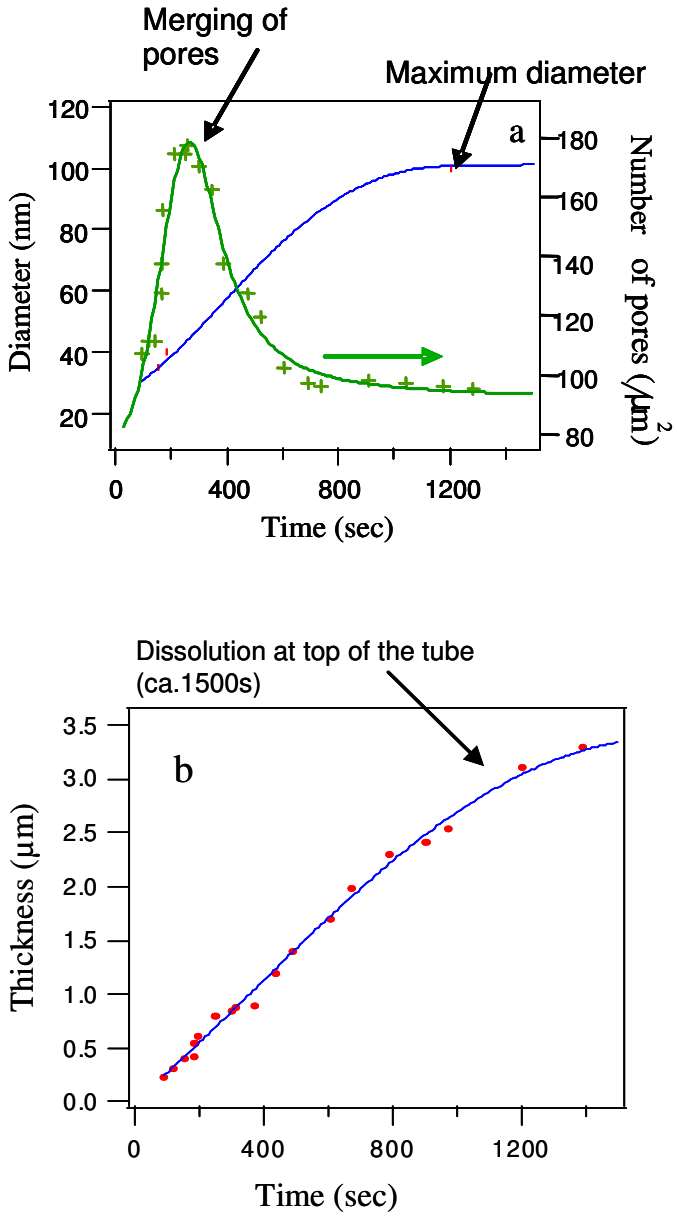

Figure 3.8 (a) The number of pores (green, crossed line) and diameter of pores (red, dotted line) as a function of anodisation time; (b) the oxide film thickness as a function of anodisation time.

The growth of nanotubes is illustrated in the schematic diagram Figure 3.9. Formation of etch pits started after 45 s after anodisation began. The number of pits

increased as they increased in size. SEM showed (Figure 3.7b and c) that these etch pits increased in size after 90 s of anodisation. At 500 s, the etch pits and hydroxide islands start to merge into a larger islands (Figure 3.7d).

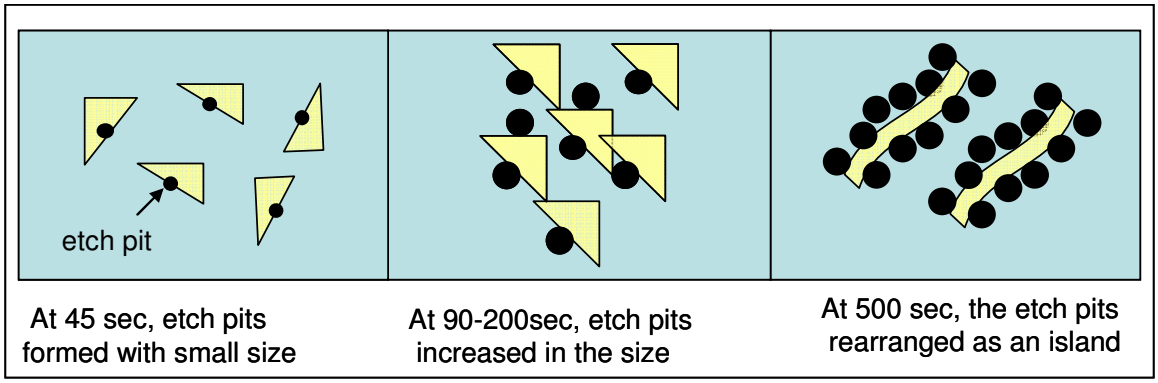

Figure 3.9 Rearrangement of the etch pits by the rearrangement of hydroxide islands.

3.4.4 Change of Current during Anodisation

With a constant DC voltage of 60 V the current was recorded as a function of time. Curve A in Figure 3.10a shows a typical current profile during anodisation of a freshly polished sample (sample A, without acid treatment). Curve B corresponds to the current profile for a sample covered with hydroxide islands (sample B). For sample A, at the beginning of the anodisation, a large current accompanied by evolution of O_2 bubbles on the anode was observed (also shown in the photo in Figure 3.4). The current dropped sharply within 9 s, then remained steady at about 35.0 mA, and decreased to 20.0 mA at 450 s. The release of O_2 gas bubbles was diminished by then. Therefore, it is reasonable to assume that electrolysis of H_2O makes significant contribution to the initial anodisation current. The initial evolution of O_2 gas indicates that direct oxidation of the metallic Ti is not very effective because of the overpotential for H_2O electrolysis.

Similar field enhanced water dissociation during formation of anodic aluminium oxide (AAO) has been studied by a computational chemical method [153].

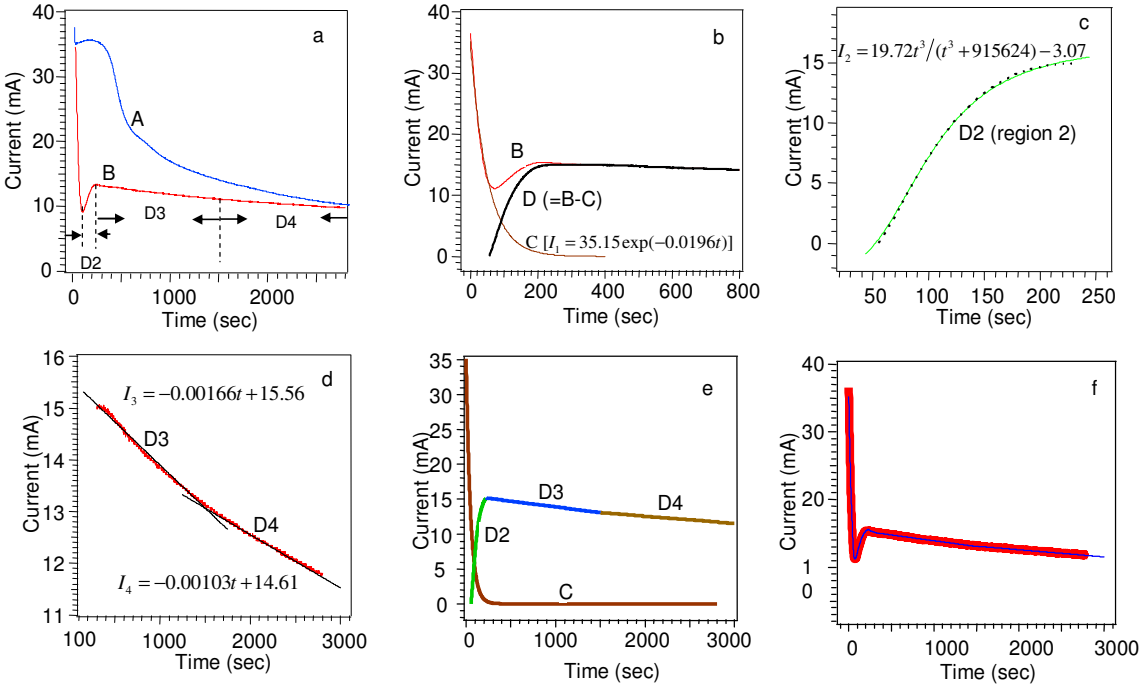

Figure 3.10 Anodisation current as a function of time. (a) Curve A (blue) from polished Ti; curve B (red) from acid-treated Ti. Anodizing regions are also indicated. The current behavior from the acid treated sample is analyzed in (b) with the exponential decay (curve C, brown) fitted at the leading edge of the current drop (curve B, red) and the residual current (curve D, black). (c) The increased current (black dot) is fitted with a cubic function (D2, solid, green). (d) The residual current decay (red) is fitted with two linear functions (D3 and D4, black). (e) Summary of four best fitting independent functions. (f) Overall curve fitting (blue) overlapped on the experimental current curve (red).

The process is more important in formation of anodic titanium oxide ATO, because the OH^- can stay in the nanotubes for a longer time and even form a double-layered wall [147, 148]. The involvement of multiple competitive reactions in the initial anodisation process makes it impossible to build a quantitative model for the time-

dependent behavior. During the first 450 s, an oxide layer is gradually developed and the anodic voltage drops within this oxide layer. This leaves a much lower anodic bias for H_2O electrolysis at the oxide/electrolyte interface. Meanwhile, the oxide layer allows migration of oxide anions so the ionic conductivity increases. The overall current becomes stable at this stage. In this region, the nature of conductivity changes from electronic to ionic.

The O_2 gas evolution is completely eliminated on the acid-treated sample B, as can be seen in Figure 3.4. Thus, the contribution of water electrolysis in the anodisation current is minimized. Sample B gives a current-time plot that is very different from that of sample A as, shown as curve B in Figure 3.10a. The typical transient current curve can be separated into three regions. In the first part, the current shows an exponential decay within 68 s down to 11.2 mA, as a compact oxide layer is formed. In the second part, the decay is followed by a short up-turn of the current to 15.5 mA, which can be generally described as the result of the growth of pores with increasing surface area. Finally, the current shows a steady decrease to 11.6 mA at 2800 s, indicating the growth of nanotubes. Although similar current profiles have been reported previously by several groups [154, 155], to the best of our knowledge, this is the first time that the catalytic role of hydroxide islands has been identified. More importantly, without the interference of water hydrolysis, the anodisation current is dominated by the migration of oxide anions associated with the formation of nanostructures. Only under such controlled conditions does it become possible to model the anodisation process.

For a quantitative understanding of the three regions of the current behavior recorded from sample B, the current curve was fitted by three independent functions,

with defined physical parameters. The three regions have been identified as involving the initial formation of an oxide barrier layer (0 s < t < 68 s), the formation of a porous structure (68 s < t < 250 s) and the elongation of the nanotubes (250 s < t < 2800 s). The behavior of the initial current (I_1) can be described by an exponential decay function, equation 3.2:

$$I_1 = a.\exp(-bt) \quad \text{.....} \quad \textbf{Equation 3.2}$$

where t is the anodisation time and the parameter a corresponds to the initial anodisation current and b defines the curvature of the decay process. Both a and b are related to the electrolyte concentration, surface area, working temperature, anodizing voltage, electrode separation and more importantly, the growth rate of the oxide layer. Specifically, the initial anodisation current, a, is determined by the ionic conductance of the electrolyte solution and should be linearly proportional to the electrode surface area and anodisation voltage but inversely proportional to the electrode separation. The rapid decay of anodisation current is due to the increase in the barrier thickness. Parameter b represents the rate constant for the growth of the oxide barrier layer. The quantity a/b defines the area under the current exponential decay curve, which corresponds to the total charge, Q, used during the formation of the initial oxide layer. The surface area of the Ti electrode, S, the oxide layer thickness, T, and the measured parameters a and b from the current time curve are related by:

$$Q = \int I_1 dt = a/b = S \times T \times 4e/V_c \quad \text{.....} \quad \textbf{Equation 3.3}$$

where e is the electron charge and V_c is the volume of each TiO_2 molecule, about 31.2 $Å^3$. The quantity $S \times T \times 4e/V_c$ represents the charge used for creation of an oxide

layer with a volume of $S \times T$. The best matching of the exponential decay is shown in curve C in Figure 3.10(b) with parameters a = 35.15 mA and b = 0.0196 s^{-1}. The surface area (S) of this sample is about 5 cm^2 (both sides). Using equation (3.3), we can estimate the maximum thickness of the metal oxide as about 175 nm, which gives a growth factor of 2.9, higher than that previously reported by Schmuki [156]. The difference may be attributed to the fact that the maximum oxide thickness could be achieved only at the equilibrium condition at which the anodisation current is reduced to zero. With previous experimental data and observation methods [156] such an equilibrium could not be physically achieved. In conclusion, by quantitatively analysis of the exponential decay of the initial anodisation process we have been able to extract the true growth factor without the limitation of achieving an equilibrium condition.

The creation of the pore structure at a very early stage increases the anodisation current by increasing the surface area. By assuming that the pores are hemispherical, the surface area, $S(t)$, as a function of time is described in equation 3.4:

$$S(t) = S(0) - N\pi r^2 + \left({}^{4}/_{2}\right)N\pi r^2 \quad \textbf{.....Equation 3.4}$$

where $S(0)$ is the initial flat surface area, N and r represent the number and the radius of the pores at time t, $N\pi r^2$ corresponds to the loss of the flat circular area and $(4/2)N\pi r^2$ corresponds to the addition of the hemispherical pore surface area. It is statistically reasonable to assume that both the number of pores (N) and the radius of the pores (r) increase linearly with time (t). In other words, $N = nt$ and $r = mt$, where n and m are proportionality constants dependent on the growth behavior. The assumption

satisfies the initial condition that at t = 0 s, N = 0 and r = 0 nm and allows equation (3.4) to be rewritten as a function of time:

$$S(t) = S(0) - nt\pi(mt)^2 + (4/2)nt\pi(mt)^2 = S(0) + nt\pi(mt)^2 = S(0) + Lt^3 \quad \text{.....} \quad \textbf{Equation 3.5}$$

where $L = n\pi m^2$.

The increase in surface area shows a cubic dependence on the anodisation time. and reaches a maximum value when the porous cross sectional area $N\pi r^2$ is approaches the initial flat surface area, $S(0)$. This leads to a simple conclusion that the maximum anodisation surface area equals $2S(0)$, double the initial surface area. To reflect the cubic dependence at the initial stage, as well as the maximum surface area, we propose a three-parameter saturated cubic formula, equation (3.6), to describe the increase in the anodisation current, based on the assumption that the anodisation current is proportional to the effective surface area at the electrolyte/oxide interface:

$$I_2 = ct^3/(t^3 + d) + e \quad \text{.....} \quad \textbf{Equation 3.6}$$

The factor d is introduced into the above equation so that when $t^3 \ll d$, the curve follows the cubic behavior, signifying the growth of porous structure, but for $t^3 \gg d$, the current becomes flat with a saturated value of (c + e) indicating that the maximum current, which is related to the maximum surface area is achieved. Here, e represents the initial current before the formation of the porous structure and c represents the maximum anodic current contributed by the increase in surface area. At the initial stage of increasing porous structure, $I_2 \approx ct^3/d$ + e. Compared with equation (3.5), it is clear that the combined parameter c/d is proportional to $n\pi m^2$, corresponding to the increase

in surface area. The time $d^{1/3}$ represents a critical time after which the rate of increasing of surface area decreases. In Figure 3.10b, the residual current, curve D, is calculated by subtracting the curve C from the measured curve B. The best fitting of this part of the process (curve D2, region 2) is shown in Figure 3.10c, with parameters c = 19.72 mA, d = 915 624 $(\text{sec})^3$ and e = −3.07 mA. With a similar saturated formula, instead of t^3, we have also tested the best curve fitting as a function of various powers of t. The standard deviations were 0.38, 0.25, 0.09 and 0.18 mA for least-squares fitting of functions of t, t^2, t^3 and t^4 respectively, so the cubic equation gives the best overall result. If the increase in surface area is dominated by the increase in the number of pores, the current will follow a linear relationship. Alternatively, if the process is dominated by the increase in pore diameter, it will follow a quadratic relationship. Under the experimental conditions described in this thesis the current *vs* time curve follows a cubic relationship, which suggests that both the number and the size of the pores increase in the anodisation, as shown also in the SEM observations (Figure 3.8). The curve D2 (region 2) passes 0.0 mA at about 55 ± 10 s, indicating the true starting point of pore formation Figure 3.10c.

While the effective anodisation area is increasing, the lengths of the nanotubes also start to grow. However, the influence on anodisation current is too small to be noticed at this early stage of growth. Once the surface area reaches a maximum, a slow decay of anodisation current is observed, as shown in Figure 3.10d (red). Careful examination of the curvature reveals subtle changes in the decay rate during the rest of the anodisation. We fit the current profile with an exponential decay curve as

$$I_3 = f_0 + f_1 \exp(-gt), \text{ with } f_0 = 9.5 \text{ mA}, f_1 = 6.2 \text{ mA and } g = 3.6 \times 10^{-4} \text{ s}^{-1}.$$

The parameter f_0 represents the steady (minimum) anodisation current. This gradual decay of the anodisation current was previously attributed to the effect of the limited ion diffusion and the concentration gradient within the nanotubes [1]. Here, the major error comes from the difficulty in identifying the leading edge of the linear decay of current, which might contain residual contributions from the initial exponential decay and continuous increasing of the surface area. The details of the growth mechanism that contribute to this exponential decay have been discussed with quantitative SEM analysis in section 3.4.3. It is clear that, although the diameter of the nanotubes increases gradually, the number of nanotubes reaches a maximum at about 200 s, so the total surface area is maximized at this time. This corresponds to the end of region 2 where the anodisation current peaks. Also, the length of the nanotubes increases almost linearly until about 1500 s. This causes the slow decay of anodisation current in region 3 to a steady current towards the end of the anodisation.

Figure 3.10e summarizes the three functions used to fit the three distinct regions of the anodisation process. The overall fitting of the experimental results (thick blue curve) is shown in Figure 3.10f with a standard deviation of 0.14 mA. For individual regions, C, D2 and D3, the standard deviations are 0.96, 0.09, and 4.0 mA respectively. The analytical error originates mainly from the D3 region, due to some extended contributions from region 2.

Comprehensive analysis of the time-current profile has allowed us to establish quantitative models based on growth mechanisms for each stage of the anodisation. This understanding enables us to control and optimize the anodisation to obtain specific nanotube morphology. For instance, nanotubes of larger diameter may be achieved by

current ramping in region 2. The analysis helps us to understand how the parameters, such as pH, fluoride concentration and temperature, are correlated with current density and the nanotube dimensions.

3.5 The Effect of Processing Parameters on Nanotube Morphology

The effect of various anodisation parameters, such as voltage, fluoride concentration, magnetic field and stirring, on tube morphology are presented here. The wetting behaviour of TiO_2 nanotube arrays (hydrophilic and hydrophobic) was examined by the measurement of the water contact angle. These parameters need to be controlled in order to manipulate the morphology of anodised titania nanotubes.

3.5.1 Influence of Anodisation Voltage on Tube Length

Figure 3.11 shows the effect of the variation of voltage on the tube length with fixed anodisation parameters including anodisation time, electrolyte fluoride concentration and working distance between the electrodes.

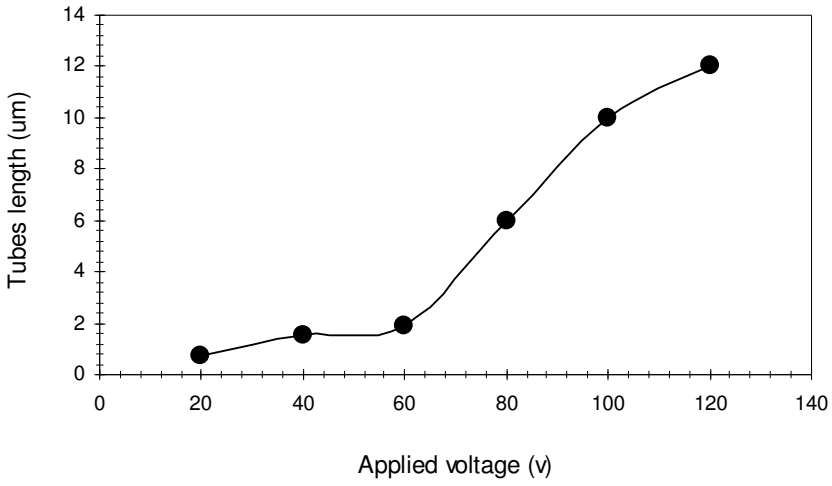

Figure 3.11 The effect of anodisation voltage on the length of the TiO_2 nanotubes at a fixed anodisation time of 1 hour.

A slow increase in the tube length was shown in the voltage range 20-60 V and a more rapid increase from 80-120 V. The increase at high voltages is attributed to formation of a thicker oxide layer. At lower voltages the oxide layer is thinner, so that the pores instead of tubes are formed. At high voltage fluoride anions are driven strongly towards the anode and this increases the etching process. Both oxidation and dissolution are maintained during anodisation. A higher anodisation current is also observed for higher applied voltages. This increases the electrolyte temperature from 25 ºC to 30 ºC, which significantly increases the ion mobility, anodisation rate and dissolution rate, and therefore the overall growth rate. The combination of these effects means that the growth rate is a non-linear function of anodisation voltage, as observed in Figure 3.11.

3.5.2 Influence of Anodisation Voltage on the Tube Diameter

The effect of voltage on the diameter has been studied by other groups [39, 157]. Their studies indicate that increasing the anodisation voltage increases the tube diameter. A linear relation between the voltage and diameter has been established, as described by $D = 2 f_g V$ [1], where f_g is the growth factor for anodic oxides (f_g = 1~5 nm/V for TiO_2). This relationship was given in 1.2.4.1 in this thesis. The high voltage drives an increase in etching by increasing the ion movement under the electric field. A study of the effect of voltage was carried out in the range 20-120 V (Figure 3.12).

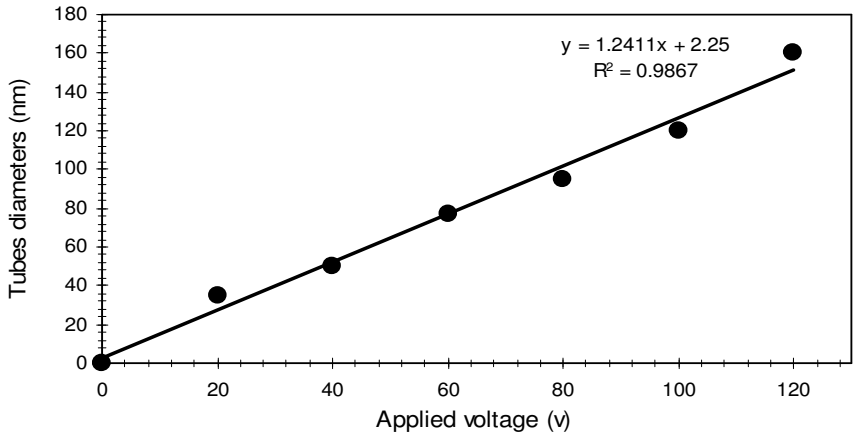

Figure 3.12 The effect of applied voltage on tube diameter at fixed anodisation time (1 hour.).

A linear increase in the diameter is achieved. The line passes through the point (0, 0) with a slope of 1.24 nm/V. Therefore, under our experimental conditions, the growth factor is 0.62 nm/V. The growth factor in our experiments is lower than those observed previously possibly reflecting the low electrolyte ion conductance (low NH_4F and water) and the choice of organic solvent (ethylene glycol).

3.5.3 Influence of the Fluoride Concentration on the Film Morphology

The study of fluoride concentration was carried out by using various concentrations of fluoride between 0.2-0.6 wt % in ethylene glycol and 2% DI water.

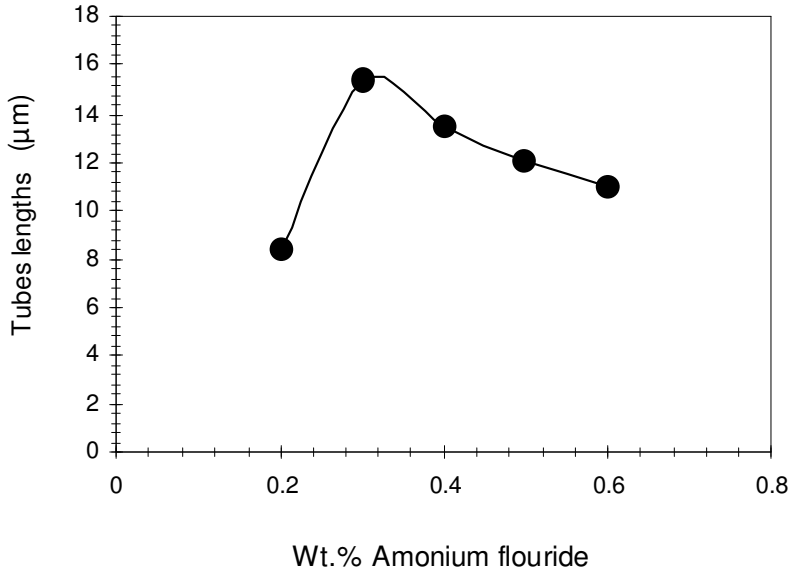

Figure 3.13 The effect of fluoride concentration on the tube length with anodisation voltage 60 V and anodisation time 1 hour.

The formation of pore or tube structures predominantly depends on the fluoride concentration at this fixed anodisation voltage and time. Electrolytes with 0.3 wt. % of ammonium fluoride give the longest tubes for a given anodisation duration. Increasing the fluoride concentration to 0.6 wt. % decreases the length of the nanotubes as more oxide dissolves at high F^- concentrations. Two examples of SEM images are shown in Figure 3.14.

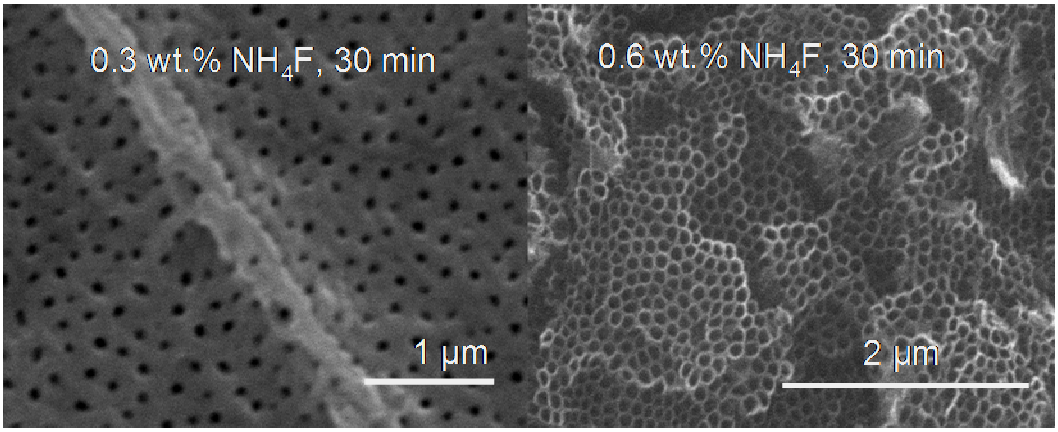

Figure 3.14 SEM images of TiO_2 nanotubes obtained with different fluoride concentrations.

For 30 min anodisation, only a porous structure was achieved with 0.3% ammonium fluoride, but good-quality nanotubes were formed with 0.6% ammonium fluoride. Faster oxidation/dissolution is expected for higher electrolyte concentrations. Similar results have been achieved by other researchers, who concluded that diffusion of fluoride into nanotubes was the rate-determining step [67, 143]. Overall, the high concentration of F^- has two effects: 1) it limits the length of nanotubes; 2) it gives good quality nanotubes. The first is determined by the dissolution rate in a vertical direction near the openings of the tubes. The second effect affects the dissolution inside the nanotubes which increases the tube inner diameter.

3.5.4 Control of Nanotube Morphology by Mechanical Stirring

In previous work stirring has been by the rotation of the anodic electrodes [158] or by use of a magnetic stirrer in the electrolyte during anodisation [143]. The formation of

TiO_2 nanotubes by a sonoelectrochemical method was found to be almost twice as fast as that from magnetic stirring [159].

We studied tube morphology by using a stirrer during anodisation. The electrodes (anode and cathode) were arranged vertically. The cathode was positioned below the anode and a magnetic bar placed above the cathode. The rotation of the bar was controlled by a magnetic stirrer underneath the electrolyte. The configuration is shown in Figure 3.15.

The purpose of adding a horizontal stirrer is to control the movement of electrolyte and ions. In a normal anodisation process, the F^- flow direction determines the orientation of the nanotubes. Therefore, we postulated that if the F^- anions could be controlled to move in a vortex by mechanical stirring, it should be possible to form nanotubes with spiral morphology. In such an inhomogeneous etching process, the flux of ions would follow the vortex towards the titanium electrodes.

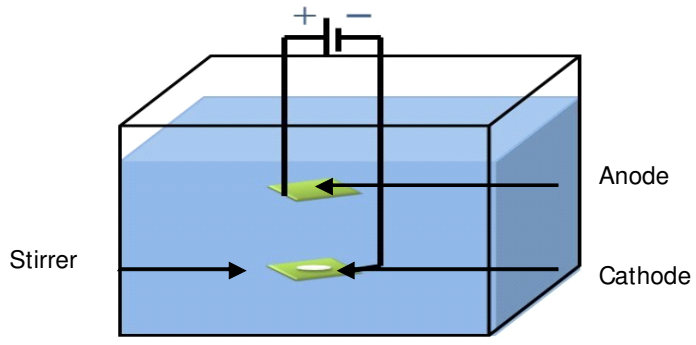

Figure 3.15 The anodisation unit used for studying the influence of stirring on nanotube morphology.

Figure 3.16 shows the vortex in the electrolyte during mechanical stirring. The movement of ions follows the movement of the electrolyte which controlled by the stirrer.

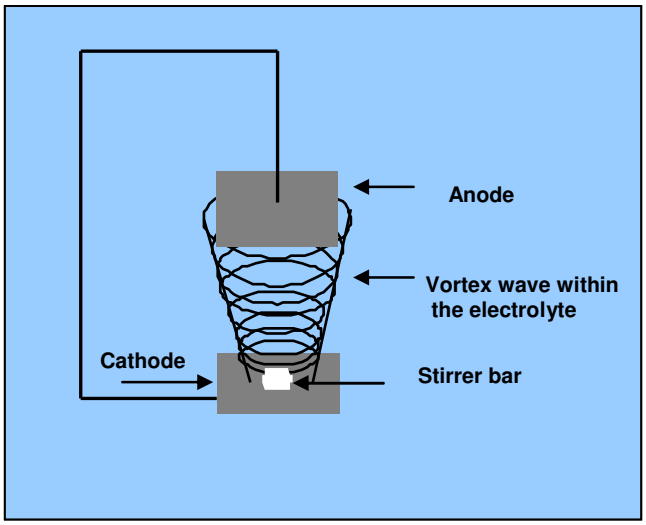

Figure 3.16 Vortex between parallel electrodes during anodisation.

Figure 3.17 shows the morphology of titania nanotubes produced by stirring for 1 hour, with applied voltage 50 V, a 6 cm gap between electrodes, and electrolyte with 0.6 % wt. fluoride. A stable vortex was achieved with a spin rate of 400 rpm. The distance between cathode and anode had to be adjusted to achieve a stable vortex. If the distance was too short, the vortex became unstable, and for longer distances, the vortex became less obvious.

TiO_2 nanotubes have smooth surfaces if they are anodised under steady conditions. With mechanical stirring, tubes with ripples on the wall can be made. These ripples are spaced evenly along the nanotubes. It is evident that there are large gaps between nanotubes. The creation of rippled nanotubes is a direct effect of the movement

of electrolytes and ions. In addition to the dissolution directed by the electrical field along the vertical direction, the dissolution in the direction perpendicular to the tube length is controlled by the mechanical stirring. The instability of the vortex is responsible for the creation of the ripples.

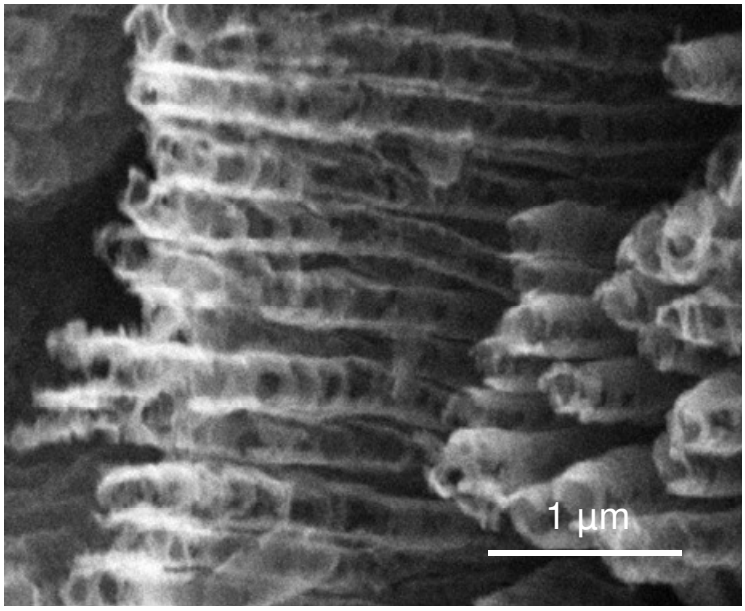

Figure 3.17 SEM image of TiO_2 nanotubes made with stirring during the anodisation.

The use of different stirring speeds alters the space between the rings on the tubes. Stirring facilitates the dissolution of the oxide layer by enhancing the diffusion paths so that the growth becomes faster as the force of the vortex pushes the ions into shorter diffusion paths. The strong vortex created during high speed stirring gives high density rings with small spaces between them, as shown in Figure 3.17.

With slower stirring, the vortex is more stable and the separation between rings larger. A typical example is shown in Figure 3.18 for a stir speed of 250 rpm. This gives

a separation between the rings of *ca*. 0.4 µm. Spiral shaped nanotubes can also be identified in Figure 3.18, but with densely packed rings it becomes difficult to identify the spiral shape of the nanotubes.

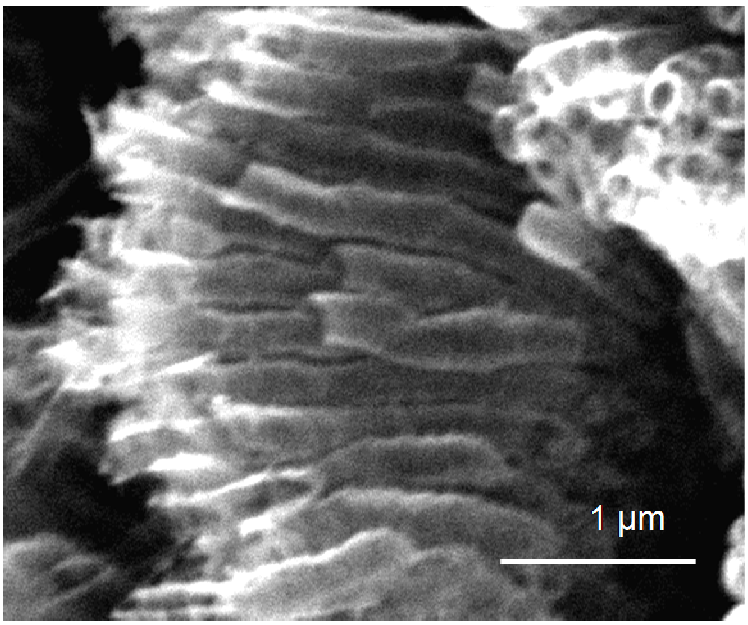

Figure 3.18 SEM image of TiO_2 nanotubes formed at slow stirring speeds. The distance between the rings is 0.4 µm.

The use of an electrolyte vortex not only creates spiral nanotubes, but also changes the overall morphology of the nanotube film. In unstirred electrolytes, a smooth layer of vertically aligned nanotubes is formed, but with mechanical stirring, bent nanotubes as shown in Figure 3.19 are usually formed. Therefore, the large scale morphology of the nanotube film can be affected by the moving electrolyte. Such effects of stirring are observed only for the area directly above the magnetic stirrer. Normal straight nanotubes are formed in other areas.

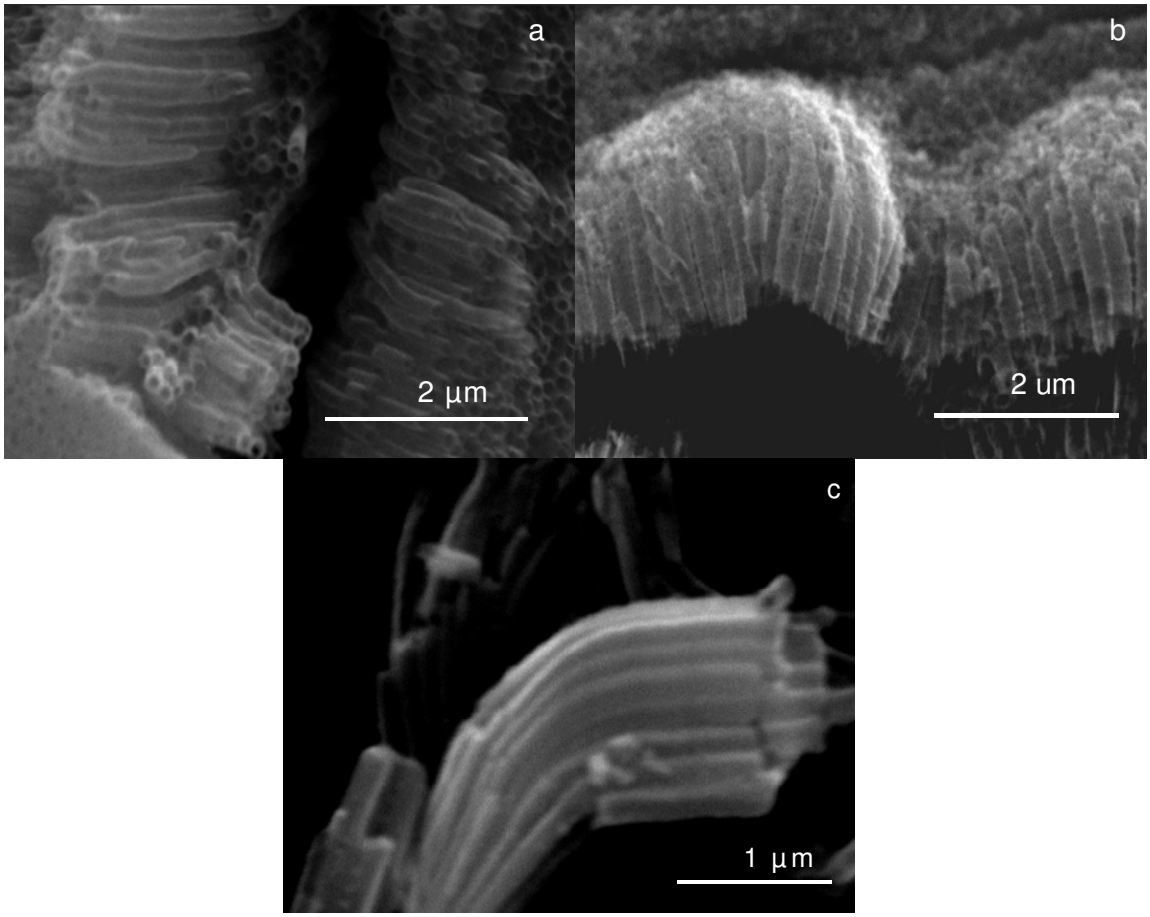

Figure 3.19 (a, b and c) SEM images showing TiO_2 nanotubes bent as a result of stirring during anodisation.

Stirring between the anode and the cathode (arranged vertically) results in a vortex in the electrolyte and the ions in this vortex move in the stirring direction. Bent tubes are produced. In other parts of the surface normal tubes are seen. The bending is increased when the speed of the stirring is increased.

3.5.5 Control of Nanotube Morphology by Magnetic Fields

An alternative to mechanical stirring is to use a magnetic field to manipulate the ion flow. A magnetic field was also used to control the formation of spiral nanotubes.

With a uniform magnetic field at an angle to the plate, the charged particles have a helical rather than circular motion. The helical motion of charged particles, such as F^- anions, can be derived from the classic Lorentz magnetic force.

According to classical mechanics, charged particles entering a uniform magnetic field at an angle θ undergo helical motion as described by equations (3.7) and (3.8). The pitch, P, and radius, R, for the helical motion of a particle of mass m and charge q, entering a uniform magnetic field of strength B, at an angle θ with velocity v are given by:

$$R = \frac{mv\sin\theta}{qB} \quad \text{.....Equation 3.7}$$

$$P = \frac{2\pi mv\cos\theta}{qB} \quad \text{.....Equation 3.8}$$

When $\theta = 0$, the radius of the spiral path of the charged particle is zero. Thus the field has to be non-parallel to the entry velocity, in order to create an effective helical pathway. In anodisation, it is believed that the applied anodic voltage on the Ti plate drives the fluoride anions moving perpendicular to the plate. Therefore the applied magnetic field has to be inclined to the Ti plate [160]. The morphology of the nanotube is determined by the dissolution of the TiO_2 barrier layer by reaction with F^- anions to give TiF_6^{2-}. We postulated that the morphology of the created TiO_2 nanotubes would reflect the helical motion of the F^- anion and that spiral nanotubes would be formed.

Figure 3.20 is illustrates the system used for anodisation with a field from a permanent magnet. The nanotubes were made by the standard anodisation process as

described in chapter 1. Polished Ti plates were used as both cathode and anode. They were immersed at 60 mm apart in an electrolyte comprising ethylene glycol (97.4 %wt), deionised water (2 %wt) and ammonium fluoride (0.2 %wt). A constant voltage (70 V) was applied between the electrodes for a period of 1 hour in order to allow the formation of TiO_2 nanotubes by anodisation. A series of permanent magnets (Nd, 2000-4000 Gauss, measured on the surface of the magnets by a Unilab magnetic flux density unit) at an angle θ behind the anode as shown in Figure 3.20.

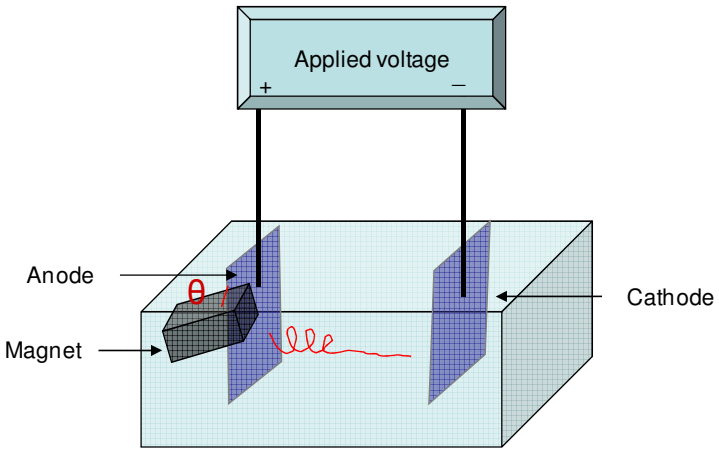

Figure 3.20 Anodisation with a magnetic field.

With SEM imaging, it was possible to analyse the effects of a magnetic field during the formation of TiO_2 nanotubes. Two main observations were made. First the morphology of the TiO_2 nanotube surface was changed upon application of the magnetic field as can be seen in Figure 3.21. As the angle between the magnetic field and the normal to the electrode surface increased, there was a shift from a well-aligned, ordered nanotube array, to a rougher surface structure with bundle-like clusters of nanotubes. The presence of the magnet field affects the trajectory of the F^- anions so that the TiO_2 nanotubes show extreme etching at the top, leading to tube thinning,

disorder and a bundled structure. It is suggested that helical nanotubes are formed initially but these are highly fragile due to their loosely packed nature. The erosion by fluoride of the fragile structures as well as the washing of the plate during preparation for SEM imaging cause the large amount of surface damage observed in Figure 3.21.

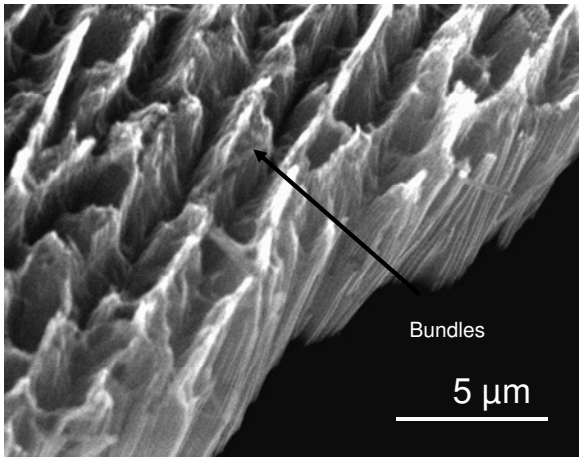

Figure 3.21 SEM image of TiO_2 nanotubes showing the bundle structure formed in the presence of a magnetic field.

The second important morphological effect of the magnetic field was to change the longitudinal structure of individual tubes. Figure 3.22 show that the application of the magnetic field caused a change from the usual ordered parallel packing to a fractured helical structure. An increase in magnetic field angle, θ, was accompanied by an increase in the density of the individual helical tubes with a reduced spiral pitch, as shown in Figure 3.22b. The tilting of the magnet for this experiment was about 60° from the surface normal.

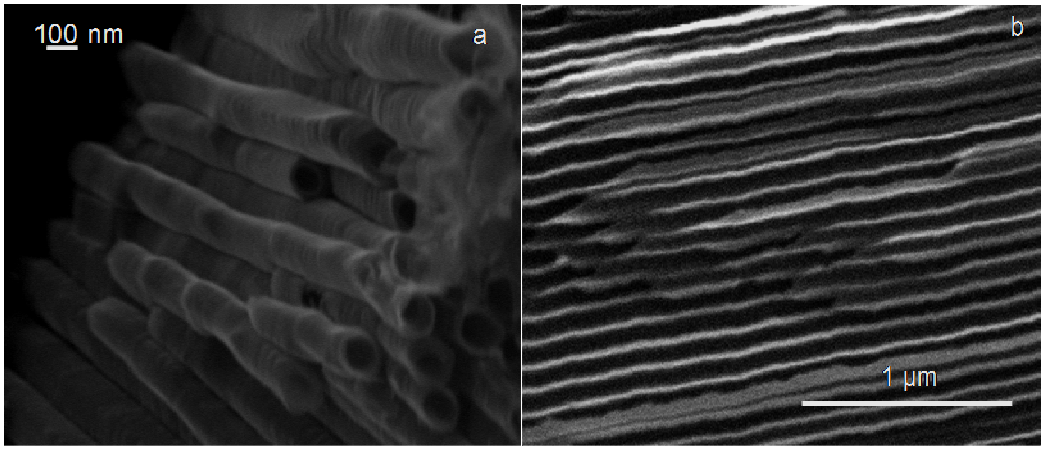

Figure 3.22 SEM images of TiO_2 nanotubes showing (a) the helical morphology of individual tubes and (b) the reduced spiral pitch when the magnetic field is about 60° from the surface normal.

At a tilting angle of 80°, bent tubes with the upper part helical, was formed shown in Figure 3.23.

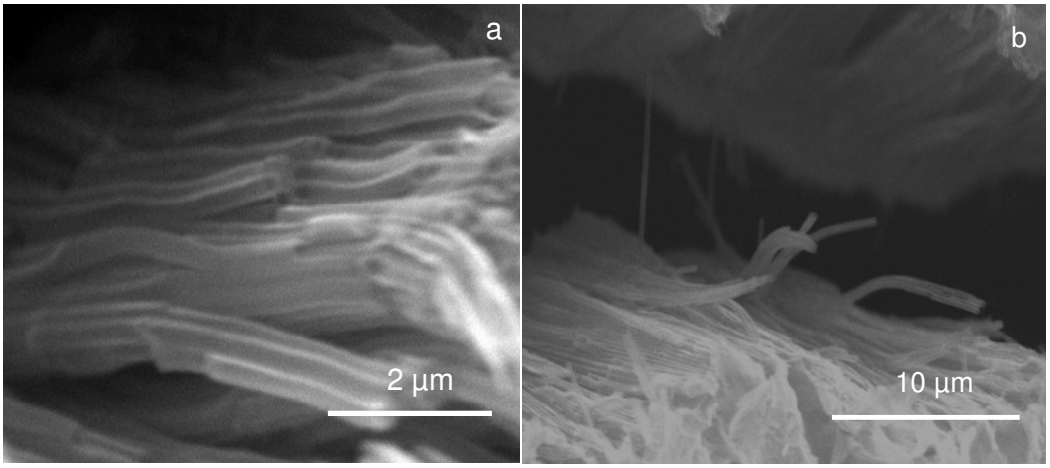

Figure 3.23 SEM images (a and b) of TiO_2 nanotubes showing bent tubes resulting from the application of a magnetic field at the titanium anode.

This non-linear nanotube morphology shows that the effects of the magnetic field were more important at high values of θ. Such bent titania nanotubular arrays were

created by both by use of mechanical stirring and by application of a static magnetic field. This suggests that the F^- anion trajectory is more important than the movement of the bulk electrolyte.

3.6 Conclusion

We have grown vertically aligned TiO_2 nanotubular arrays by anodisation of titanium in an electrolyte consisting of water, ethylene glycol and ammonium fluoride. Hydroxide islands were formed by dipping Ti plates into acid solutions and measurement of contact angles has confirmed that the acid-treated surface is hydrophilic. We have compared the anodisation current profiles of clean Ti and hydroxide-covered Ti, and shown the contribution of water dissociation in the anodisation current. The current-time profile shows four distinct stages. It was found that a cubic equation is appropriate to fit the current increase after an initial exponential decay. The dissolution process has been characterised. With hydroxide-covered Ti, the initial formation of etching pores was found to be exclusively at the interfaces between the hydroxide islands and the Ti substrate. Further anodisation increases both the diameter and the number of etching pits. The detailed influence of processing parameters, including anodisation voltage and solution concentration, on the nanotube morphology has been quantitatively studied.

Further manipulation of the morphology of TiO_2 nanotubes was achieved by use of mechanical stirring or by application of an external magnetic field. Separated nanotubes with rings and ripples were formed by mechanical stirring and spiral and bent nanotubes upon application of a magnetic field. Mechanism of these modified

anodisation processes have been discussed. Tubes with rings and gaps (voids) between tubes and bent tubular arrays were formed with both modifications. A bundle structure was formed upon application of a magnetic field.

Chapter 4 Formation of polygonal TiO_2 Nanotubes

4.1 Abstract

TiO_2 nanotubes with polygonal cross-section were formed on a prepatterned of Ti surface with scratches made mechanically by a ruler and sand paper. Rectangular patterns on a titanium plate were mechanically molded. Structural details were observed by close inspection of the cross section of the nanotubes and top-view by SEM and TEM. The tube length was slightly greater on prepatterned Ti surfaces than on non-patterned surfaces indicating that growth was enhanced by the pattern. This suggests that prepatterned grooves provide sites at which the activation energy is reduced so that the growth proceeds faster.

4.2 Introduction

Recently, titanium dioxide nanotubes on semiconducting surfaces have attracted much attention because of potential applications in photocatalysis. In fact, TiO_2 is now one of the most widely studied metal oxide semiconductors due to its superior photocatalytic activity; [1, 2] and its stability in water [3]. The properties of TiO_2 nanotubes depend on their shape, and size and the phases of the crystallites structure. Control of the morphology could improve efficiency and affect the electrical properties of devices. There are many reports focusing on the synthesis of TiO_2 nanostructures, such as rod [161], bullet [162], wire [163], diamond [162], cube [164], sphere [165] and needle [166]. Various TiO_2 nanotube shapes have been observed, eg. tapered rutile TiO_2 nanotubes with rectangular cross-sections made by hydrothermal methods [167].

However, to the best of our knowledge, the direct synthesis of TiO_2 nanotubes with polygonal shape by normal anodisation has not been reported. Compared with circular nanotubes, there three potential advantages of polygonal nanotubes that might lead to higher photo efficiency. First, the discontinuities in the tube wall could encourage formation of crystallised facets at low temperature. Secondly, in comparison with circular nanotubes, the void between polygonal nanotubes can be diminished with much better face-to-face contact. Thirdly, the inner diameter of a nanotube with polygonal cross-section is usually larger than that of a circular nanotube prepared under the same conditions. The first two of these characteristics of the polygonal nanotube can directly improve the charge mobility with better charge separation, while the third property can improve the transport of electrolyte in and out of the nanotube, with improved ion conductance.

Modern methods, such as photoelectron beam lithography [168], focused ion beam [169], self-assembled mono layers [170], channel stamping [171] and atomic layer deposition [172] can be used for forming patterns on metal surfaces. Many of these methods are expensive, complicated and might be restricted to samples of a particular size. Therefore there is a need for a low-cost method for formation of large patterns on TiO_2 surfaces. Herein, we demonstrate a facile mechanical patterning method and the effects on the morphology of anodised TiO_2 nanotubes.

4.3 Experimental Details

After samples were polished with diamond paste (as described in chapter 2 section 2.2), the plates were mechanically patterned. Rectangular patterns were created on the surface by gently gliding silicon carbide abrasive (1200 grit) paper in perpendicular directions. The patterned plate was cleaned ultrasonically in DI water. Anodisation was performed in an electrochemical cell using a clean titanium plate as the cathode. The electrolyte contained 0.6 % wt. of ammonium fluoride (analytical grade) and 2 % wt. water in ethylene glycol. The voltage was kept constant at 100 V with an electrode separation of 65 mm. The surface area exposed to the electrolyte was approximately 2 cm^2 at each electrode. The experiments were performed at room temperature under atmospheric conditions without stirring. The time-dependent current was recorded using a USB data logger (U12, Labjack). The same anodisation conditions were used to prepared circular nanotubes but without patterning of the Ti plate before anodisation. Titanium dioxide nanotubes were imaged using a scanning electron microscope (JSM 820M, Jeol) operating at 30 kV and a transmission electron microscope (Hitachi- 7100) operating at 100 kV.

4.4 Results and Discussion

Figure 4.1 shows SEM images of a mechanically patterned TiO_2 sample before and after anodisation. Figure 4.1a shows that the sample is smooth with some polish marks left by the diamond paste. A rectangular pattern is formed on the Ti surface by grinding it in perpendicular directions. Although the size of the rectangles is not controlled, the rectangular shapes are clearly visible from the trenches formed by the grinding, as seen in Figure 4.1b. The rectangular pattern influences the morphology of

anodised TiO_2 nanotubes, as the local electric field that controls the tube morphology follows the shape and size of the pattern. Figure 4.1c shows that the patterned is preserved during anodisation as bundles of nanotubes have formed on and off the trench. A larger scale SEM image reveals that the majority of the nanotubes have formed with polygonal cross-sections. The high resolution image in Figure 4.1d shows that a mixture of hexagonal, pentagonal and some irregular quadrilateral nanotubes had formed after anodisation for 2700 s.

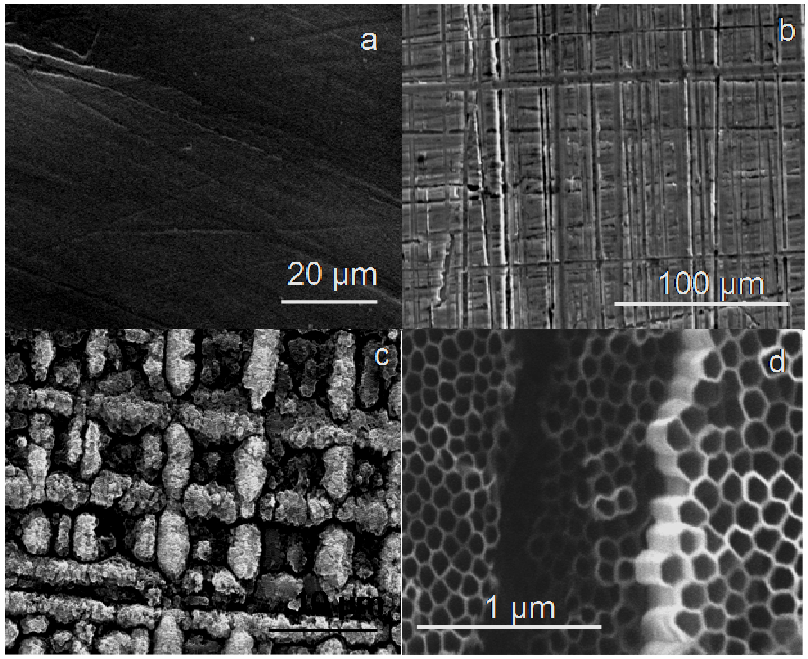

Figure 4.1 SEM images of a Ti sample before and after anodisation showing a) a polished clean Ti surface, b) the rectangular prepatterned Ti sample c) a large area of prepatterned sample after anodisation and d) a high resolution SEM image of polygonal TiO_2 nanotubes after 2700 min anodisation.

From a flat, non-patterned surface, circular nanotubes are normally formed with a void between the adjacent nanotubes. However, on the surface with a rectangular pattern, the flat tube walls are shared between adjacent tubes without voids.

4.4.1 Morphology Evolution during the Anodisation

The patterns created by the mechanical moulding can influence the tube morphology significantly at the early stage of the anodisation. To understand this, the shape of the tubes was monitored as a function of anodisation time. At an early stage, after 2700 sec of anodisation, the cross-sections of the tubes were nearly rectangular, as shown in Figure 4.2a. At this stage, the nanotube follows the morphology of the patterning on the surface, which is primary rectangular. Further anodisation, however, converts the rectangular nanotubes into the pentagonal and hexagonal shapes shown in Figure 4.2b. We assume that two factors affect the morphology: 1) the shape of the prepattern and 2) the distribution of the anodisation electrical field. Although the prepattern drives the formation of rectangular nanotubes, the field distribution of the bottom of the nanotube prefers to be circular nanotubes. Thus, initially rectangular nanotubes are formed and these gradually evolve through tubes of polygonal cross-section into circular nanotubes as the tube length increases.

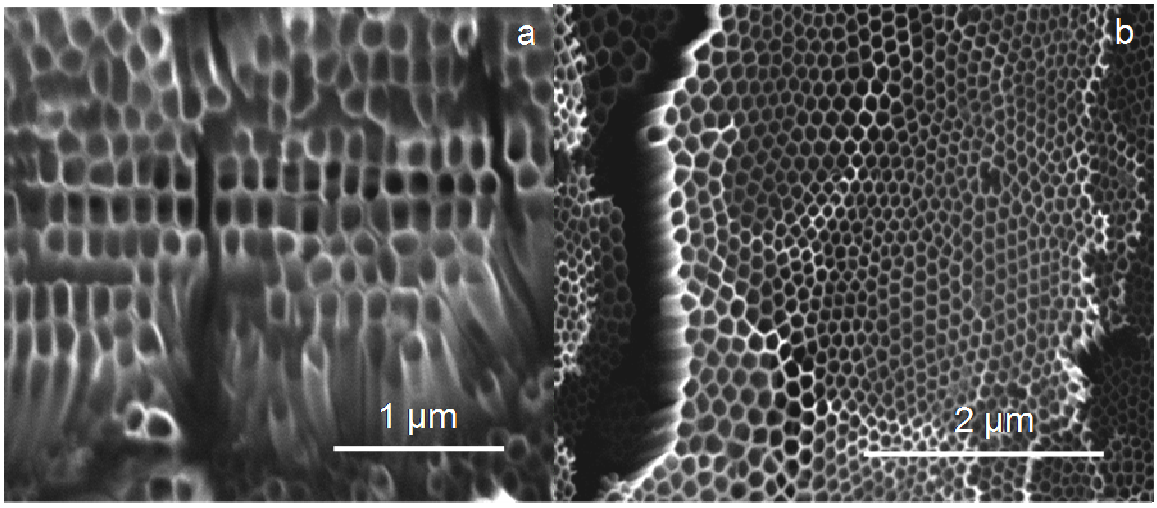

Figure 4.2 SEM images of TiO_2 nanotubes showing the conversion of the tube shape from (a) square to (b) polygonal during anodisation.

After anodisation for one hour under 100 V applied voltage, the diameter of hexagonal tubes reached 120-140 nm with an average length of 11 µm. The growth of polygonal TiO_2 nanotubes is faster than that of circular nanotubes. The typical tube length for a circular nanotube after 1 hour is about 10 µm, whereas for prepatterned surfaces a polygonal tube 11 µm long is achieved. The faster growth is also indicated by the rapid formation of nanotubes the porous structures connected with neighbouring tubes. This suggests that both vertical and horizontal growth rates for prepatterned surfaces are faster than those on non-patterned surfaces. The faster growth rate can be attributed to either a focused electrical field on the edge of the patterns and to the large tube diameter that facilitates mass transport of the electrolyte. We believe that at the beginning of the anodisation, it is the focused electrical field that causes the fast growth, whereas towards the end of the anodisation, the large diameter becomes the dominant factor. Quantitative analysis of these effects is difficult.

4.4.2 The Effect of Initial Surface Texture on the Growth Mechanism

When an oxide layer is formed on the titanium plate, the current rapidly decreases exponentially because the oxide layer prevents electronic charge from reaching the substrate underneath, as shown in Eqn 3.2. As can be seen from current-time curves (Figure 4.3) the initial anodisation current of a prepatterned plate is slightly greater than that of a non-prepatterned plate which gives circular tubes due to the larger surface area of the patterned surface. Both prepatterned and none prepatterned plates were polished thoroughly before anodisation. Oxygen bubbles on the titanium anode were associated with the initial high anodisation current.

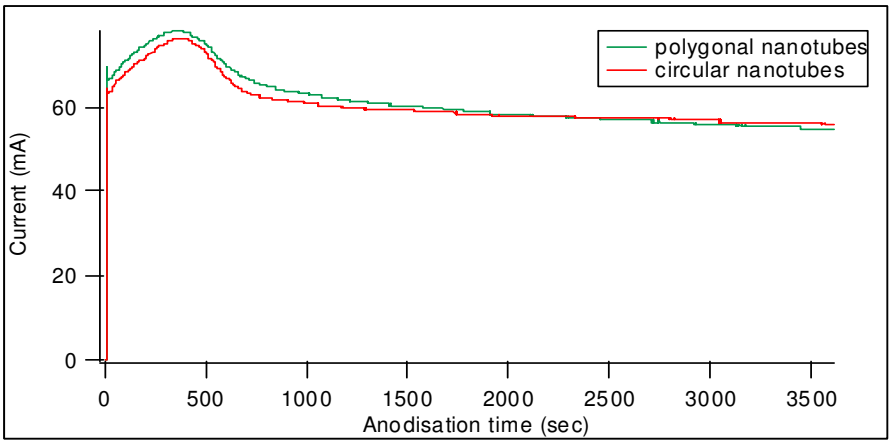

Figure 4.3 Current-time curves for prepatterned and non-patterned Ti plates.

4.4.3 Crystallinity of TiO_2 Nanotubes: Circular *vs* Polygonal

It was reported that after anodisation TiO_2, contains very small crystals of anatase [143]. The charge mobility within the nanotube is associated with the crystallinity of the TiO_2 phase. High photoefficiency is usually related to polygonal nanotube with crystallinity.

TEM has been used to determine the crystal phase of the titanium dioxide. The polygonal nanotube was annealed in air at 300 ˚C for 1 hour. A diffraction pattern from the wall of the nanotube is, shown in Figure 4.4b. The rectangular pattern is associated with the (101) face of the anatase phase and the bright diffraction pattern indicates a good-quality crystal structure.

The TEM image in Figure 4.4a also shows the folding edge along the walls of the polygonal nanotube. Both SEM and TEM images show no obvious voids or separation between adjacent nanotubes, so it can be concluded that the crystallised polygonal nanotubes share side walls, although they are only about 20 nm thick.

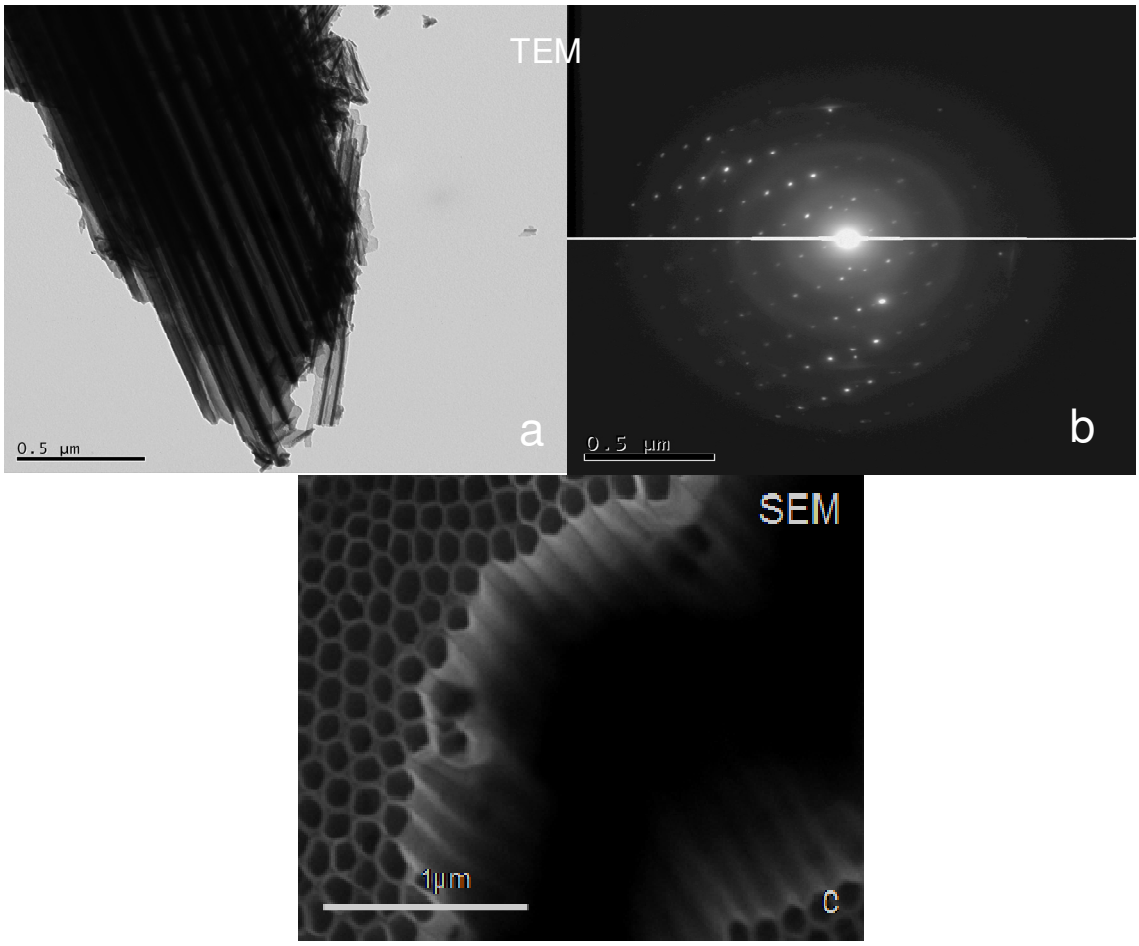

Figure 4.4 Polygonal TiO_2 nanotubes annealed at 300 °C (a) side view (b) selected area electron diffraction (SAED) taken by TEM and (c) cross-section taken by SEM.

4.5 Conclusion

In this study we used a prepatterned Ti surface to create polygonal nanotubes. At the early stage of anodisation, rectangular nanotubes are formed. These evolve into polygonal nanotubes after further anodisation. TEM and SEM observations have proved that the high quality polygonal nanotubes are formed at room temperature and SAED has proved that on the side wall of the nanotube can be observed by annealing the

sample at 300 °C. In contrast to circular nanotubes, the polygonal tubes share their side-walls with adjacent nanotubes.

Chapter 5 Control of the Morphology of TiO_2 Nanotubes by Patterning with Electron Beam Lithography

5.1 Abstract

The synthesis of rectangular nanotubes was achieved by patterning the surface by electron beam lithography (EBL) followed by anodisation. The EBL pattern plays a key role in achieving various TiO_2 nanotube shapes. Two-step anodisation on the line pattern with different electrolyte compositions gave tube-in-tube TiO_2 multiwall nanotubes.

5.2 Introduction

The shape of TiO_2 nanoparticles depends on how they are formed. For instance, by both alumina template and atomic layer deposition, nanotubes with wall thickness less than 3 nm have shown a wall-thickness-dependent blue-shift in optical absorption spectra [173].

A titania sol gel precursor with PMMA moulds gave thin films of titania with pores 35-65 nm diameter [174]. The PMMA mould was prepared by thermally infiltrating PMMA into anodic alumina templates. Both pore dimensions and depths were modifiable by control of the anodisation conditions. The limitation of this method was associated with the wet etching used for mould release from the master.

Control of the shape of nanopores and nanotubes has been reported by Masuda et al. [175]. They used a prepatterned silicon chip to transfer the patterns on to aluminium

which was anodised to create nanopores. By using hexagonal, triangular and square patterns, they successfully created hexagonal, triangular and square Al_2O_3 nanopores. Their work demonstrated the principle that prepatterning on a substrate could have a significant effect on the shape of the nanostructures formed during anodisation. On a Ti substrate, our mechanical patterned surface has also been shown to give polygonal and square TiO_2 nanotubes, as described in the previous chapter. However, the simplicity of the mechanical moulding method meant that control of the surface texture was very limited and the quantity and density of the square TiO_2 nanotubes was low. We therefore, decided to use electron beam lithography to try to grow square nanotubes over a large area.

For patterning small numbers of experimental devices, electron beam lithography has two attractive features. First, the mask fabrication is easy. Secondly, high resolution can be achieved by good control of process parameters, such as beam energy, current density and exposure time. The disadvantages of the EBL technique are that it is expensive and it is not suitable for large surface areas. In this work, we used EBL to prepattern Ti substrates to create titanium dioxide nanotubes of various shapes by controlling the parameters for both the EBL and anodisation processes. The patterns made possible the fabrication of TiO_2 nanotube arrays with rectangular shapes. These cannot be made without patterning. Self-ordering and the formation of double wall nanotubes were also observed. The guided anodisation process and the control of anodisation conditions are also discussed.

5.3 Experimental Details

Titanium plates were prepared following the method in chapter 2 section 2.2. The plates were then spin-coated with a solution of polymethylmethacrylate. Surface roughness is important to achieve adhesion between the plate and PMMA-coated layer and the desired roughness was created by etching the Ti with HF solution. Such etching in acid creates an appropriate density of isolated hydroxide islands as shown in section 3.4.

The PMMA solution was prepared by dissolving 5 wt % of PMMA in anisole. The preparation of a PMMA positive photoresist involved stirring the PMMA solution for at least 24 hours. The resist film was made by spin coating on to a Ti plate at a fixed speed of 1500 rpm for 40 s, to give a layer of PMMA with a thickness of 0.62 mm. The plate was then baked on a hotplate at 160 $^{\circ}$C for 60 s in order to remove solvent.

EBL uses a focused beam of electrons that can be controlled by the probe current, voltage and working distance to achieve the appropriate beam size. The pattern was formed by moving the sample (controlled by the X-Y sample stage) and the PMMA film was exposed to the electron beam. The exposed PMMA film was developed by dipping the sample into a mixture of methyl isobutyl ketone (MIBK) and isopropanol (IPA) for 2 min, followed by post baking at 60 ºC for 3 min on a hotplate in the air. This step removed residual developer, created a fixed film on the titanium surface and enabled the further anodisation of the specimen without loss of the polymer. If the baking temperature is too high, the PMMA melts (M.P. 120 ºC) and the pattern is distorted. After this stage, a pattern was formed on the titanium with the area exposed to

the electron beam free of PMMA and the sample was ready for anodisation to create TiO_2 nanotubes.

5.4 Results and Discussion

The concept behind using EBL to control nanotube morphology is that the small area in the pattern restricts the electric field distribution during the anodisation so the etching ions are forced to etch the titanium oxide according to the pattern. The parallel edges of the line pattern give rectangular or square-shaped nanotubes on the substrate.

In our work, we showed that rectangular TiO_2 nanotubes could be made in two anodisation steps. The first stage of the anodisation process on the line patterns was in an ice bath for 1 hour and the second at 22 ºC for 1 hour. After lengthening during anodisation, the tubes were converted into different shapes and finished with a polygonal shape, making time an important factor. In the following sections the parameters that affect the overall processes are discussed.

5.4.1The Thickness of the Resist

A thin polymer coating produces a narrow line. However, a thick layer of polymer is required in order to repeatedly anodise the same surface without removal of the coating. The thickness of the polymer determines the minimum electron beam exposure. In order to obtain the thinnest lines it is crucial to minimize the beam size by reducing the probe current. Taking this into consideration, the plate was spun twice with the PMMA solution (5%wt) to produce a layer thickness of about 0.62 mm. The plate was then baked on a hotplate at 160 ºC for 60 s in order to dry the sample before EBL.

5.4.2 EBL Parameters

EBL is a focused beam of electrons that can be controlled to form patterns with very small diameter pattern. The probe current was optimised at 2×10^{-9} A (2 nA) at an accelerating voltage of 30 kV. The focused beam of electrons was scanned over a polymer surface in parallel lines to form the desired pattern. The magnification was set to 100,000 X and the working distance was 7 mm. These parameters were those used to achieve the highest resolution on our Jeol 820M SEM. Because the sample stage was moved manually to form patterns, we were only able to produce grid patterns based on straight lines. The schematic diagram in Figure 5.1 illustrates the EBL process on a Ti substrate, which has been precoated with PMMA. Then after EBL the anodisation was carried out on the Ti substrate to create the TiO_2 nanotubes.

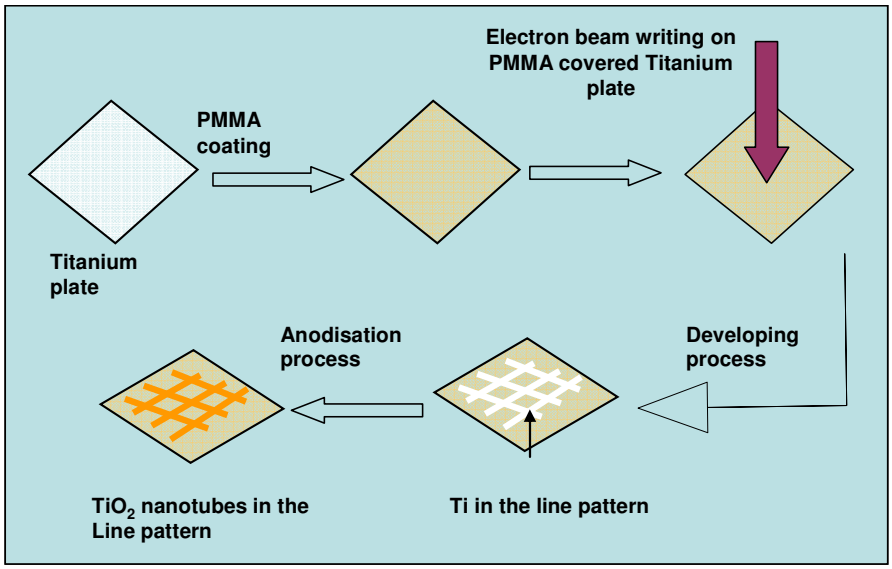

Figure 5.1 Schematic diagram showing the steps in the formation of a grid pattern by use of electron beam lithography followed by the anodisation of the patterned sample.

5.4.3 Development of Patterns

Exposure of PMMA to a high energy electron beam induces the scission of the chain of methacryliate monomers that constitute the resist material. It is generally accepted that the main process consists of the breaking of the main polymer chain, but other scission possibilities may also occur as seen in Figure 5.2 from [134]. For a positive photoresist like PMMA, the developing process selectively removes the exposed regions of the resist.

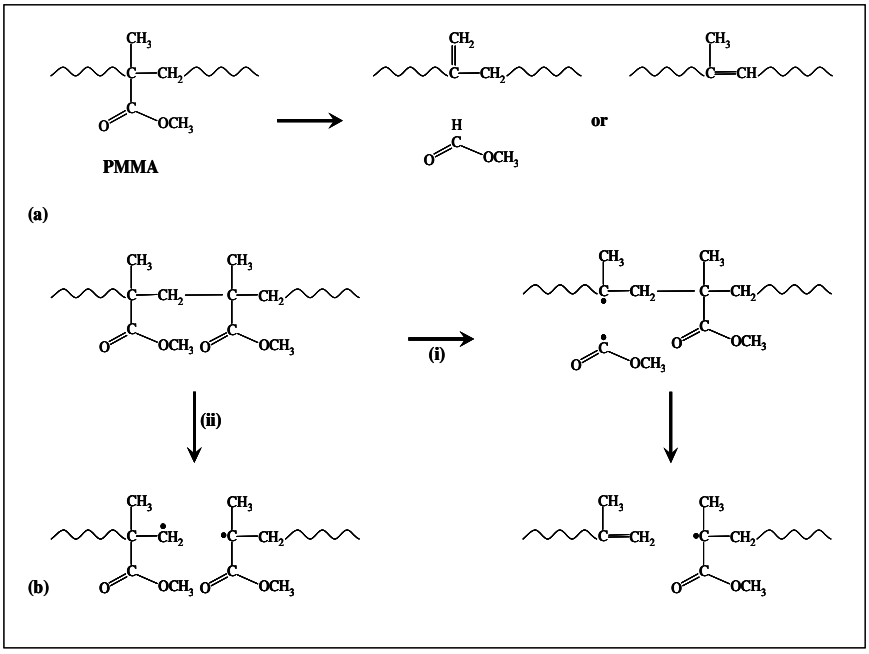

Figure 5.2 Developing process and chain scission of methacrylic polymer [134].

The general developer for PMMA is a mixture of MIBK and IPA [168]. However, because MIBK is a good solvent for PMMA it dissolves both the exposed (patterned) and unexposed (non-patterned) regions (at a much lower rate). Therefore there is significant thickness loss in the unexposed regions. In order to improve the lithography it is necessary to increase the dissolution selectivity between exposed and unexposed regions.

In this work, two types of developer solutions were tested. A mixture of MIBK and IPA, 1:3), and a mixture of isopropyl alcohol and deionised water (IPA: H_2O 7:3) were both found to be suitable for thick polymer layers. The role of IPA is to decrease the overall ‘‘development strength’’ of the developer. A solution of MIBK:IPA in 1:1 ratio causes significant loss of polymer thickness in the unexposed area. A mixture with MIBK:IPA 1:3 gives almost negligible thickness loss in the unexposed regions with moderate sensitivity and achieves high contrast and high resolution on the substrate surface. The MIBK: IPA solution gave sharper lines than IPA: H_2O so it was selected for use in this experiment. The developing time was 30 s followed by rinsing in IPA and deionised water.

5.4.4 Fixing the Polymer Film

Good adhesion between the titanium plate and the polymer is critical if a stable pattern is to be achieved during anodisation. This gives tubes on the plate carrying the EBL pattern whilst the parts of the surface covered with PMMA remain unchanged. If the polymer film detaches from the surface during the anodisation, the definition of the patterns is lost and titanium dioxide nanotubes form on both patterned and non-patterned surfaces.

Two procedures were adopted to improve the polymer film adhesion. First, the roughness of the titanium surface was increased by acid treatment with solution A as described in chapter 3 [176]. Secondly, by baking the plates in air at 60 ˚C for 3 min on a hotplate residual developer was removed and the coating was securely fixed to the titanium surface.

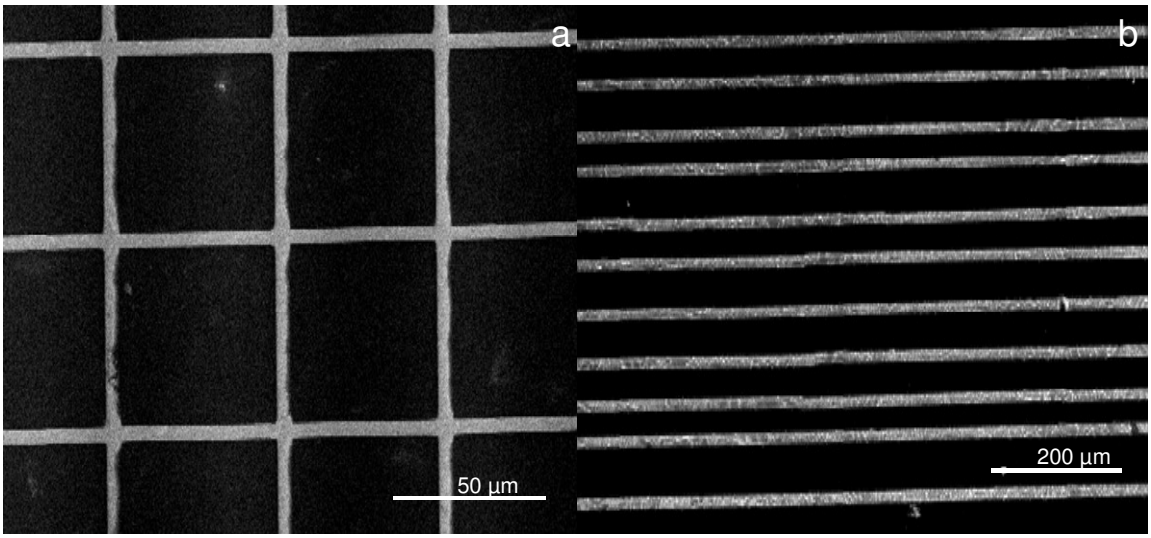

Figure 5.3 SEM images of (a) grid and (b) line patterns created by EBL on a polymer-coated titanium surface.

With the polymer firmly in place, grid and line patterns were made by EBL, as shown in Figure 5.3 (a and b) respectively. In Figure 5.3a the separation between lines is 60 µm and the line width is about 5 µm. Some defects can be observed due to the uneven development of the pattern. Figure 5.3b shows line patterns obtained by moving the sample horizontally. The overall length of the lines can be as long as 12 cm. The separation between lines is about 50 µm and the line width 5 µm.

5.4.5 The Effect of Line Width on Tube Shapes

Anodisation naturally produces circular nanotubes; other geometries rarely, if ever, occur. With patterned plates, the anodisation is restricted by the shape of the patterns so different tube shapes may be achieved. By investigation of plates having different line widths with a standardized anodisation procedure we concluded that the wider the line widths the less the effect on the morphology of the nanotubes. With low magnification, SEM showed that lines 10 µm wide gave circular nanotubes, as shown in Figure 5.4.

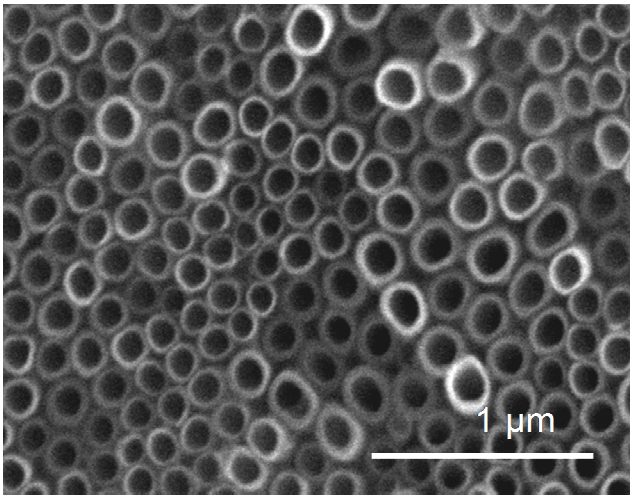

Figure 5.4 SEM image of circular TiO_2 nanotubes on a pattern with lines 10 µm wide.

In our method, the optimal line width of the pattern was about 5 µm. If the nanotubes have diameter of 150 nm or so, 30 nanotubes may be accommodated across one line.

Figure 5.5a shows the pore structures formed in the initial stage of the anodisation on part of a line pattern with a width of 4.77 µm. It seems that elongated etch pits were

formed. Rectangular TiO_2 nanotubes were obtained after 2 hours anodisation, as shown in Figures 5.6b and c.

The PMMA protected area can also be observed in Figure 5.5b, in which the line patterns are aligned horizontally. Both the outer and the inner boundaries of the TiO_2 nanotubes, shown in Figure 5.5c appear to be rectangular, instead of circular. There is no clear correlation between the direction of the line patterns and the orientation of the rectangular nanotubes, but such rectangular nanotubes can be produced only on prepatterned Ti samples.

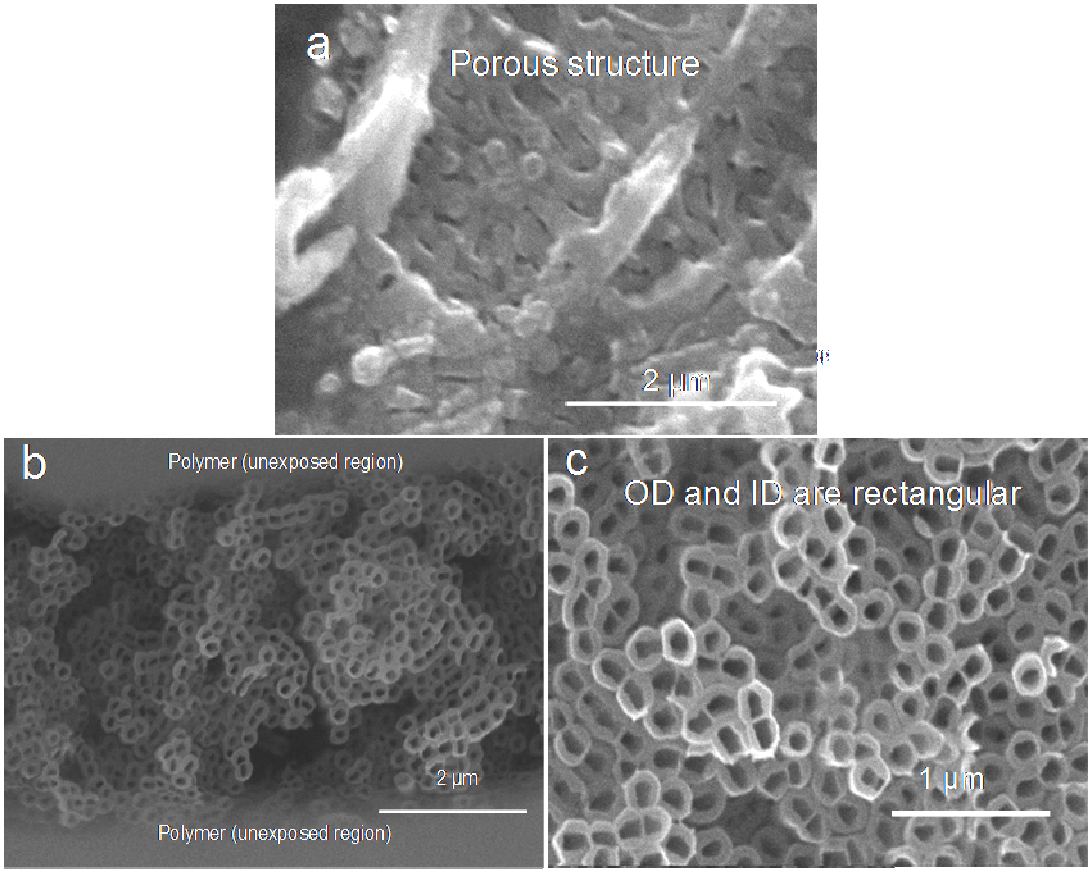

Figure 5.5 SEM images of (a) elongated pores produced on the line pattern (b) rectangular nanotubes formed on the line pattern after 2 hours anodisation in ice first then 2 hours at room temperature (c) top view of rectangular nanotubes in which the inside is rectangular.

The inner cross-sections of the nanotubes are mainly rectangular while the outer cross-sections are a mixture of polygonal and rectangular.

In this image, the average wall thickness is about 60 nm and the inner rectangular pores have dimensions 60 nm × 120 nm. The inner rectangular shape seems to be randomly oriented. The formation of such rectangular nanotubes is related to the formation of the initial elongated etch pits.

5.4.6 Changes in Titania Nanotube Shape during Anodisation

In order to further understand the effects of patterning on the morphology of TiO_2 nanotubes, a rectangular grid was generated by EBL with PMMA as photoresist. The grid pattern is shown in Figure 5.6. In the initial stage of the anodisation, pores of 30 nm diameter were formed within the lines of the grid pattern. In contrast to the parallel line patterns showed in section 5.4.4 some alignment of the pores can be clearly identified. The pores are aligned along a diagonal, at 45° to the line edges as shown in Figure 5.6. This pore structure was observed after anodisation for 1 hour in an acidic electrolyte containing 10 ml H_3PO_4, 1 ml of 4% HF and 100 ml of EG. The anodisation was carried out at low temperature (0-5 °C) to reduce the rate and to avoid widening of the nanopores.

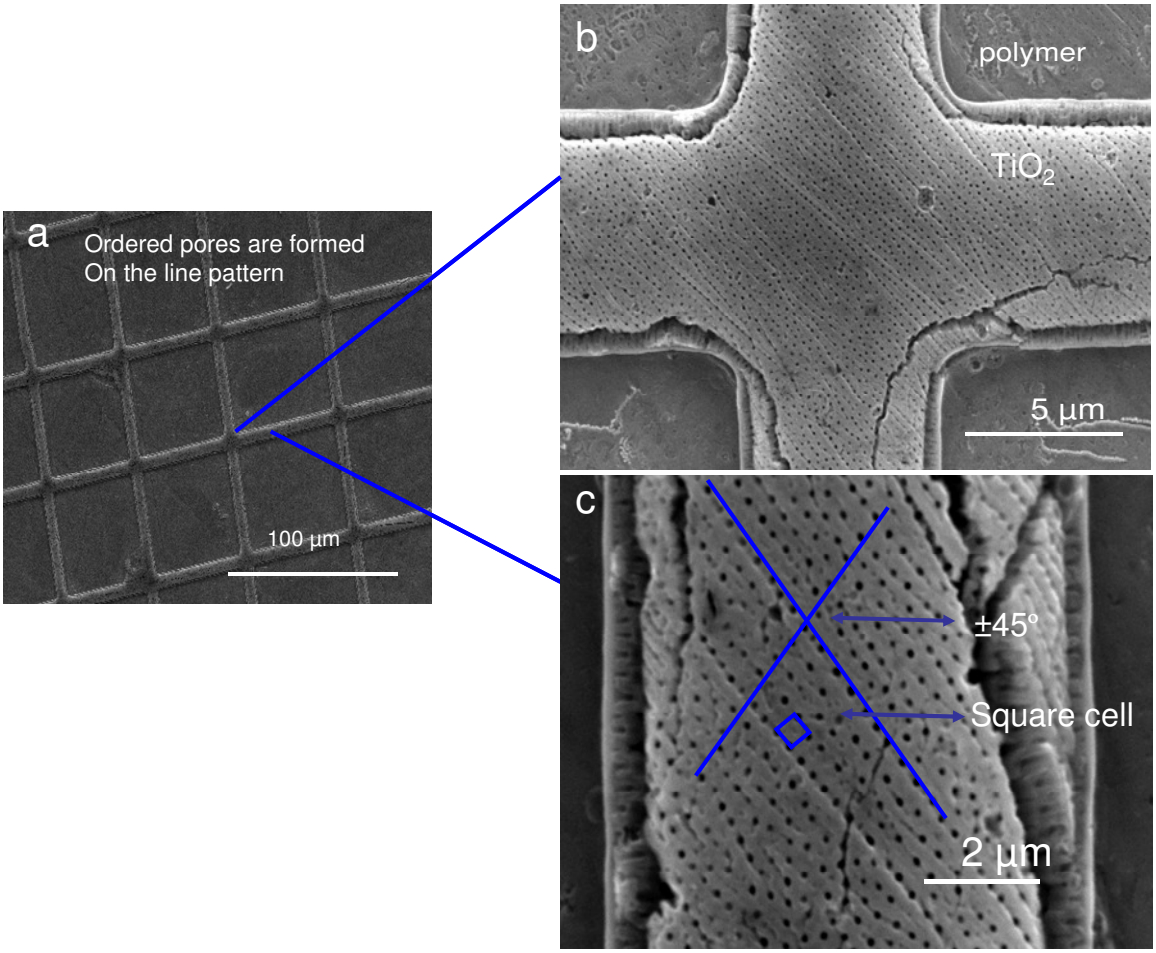

Figure 5.6 SEM images of TiO_2 nanotubes showing (a) the grid pattern (b) the self-ordered pores on the line pattern (c) the alignment of pores on the line pattern.

A comprehensive explanation for the 45° arrangement of the self-ordered tubes is not yet available in the literature. However, such ordering must be related to the interaction between pores and line edges of the pattern. One possible explanation is that there are weak repulsive interactions between the pores and line edges, as well as between the pores themselves. A maximum distance between pores is achieved with a diagonal alignment relative to the line edges. Further anodisation adds pores between and along these specific directions. The overall density of the pores is determined by the

anodisation voltage. Such repulsive interactions could be driven by the space charge interactions between F^- ions in the electrolyte, which are also responsible for the final ordering of the nanotubes. On a non-patterned surface with a large area, no edge effect exists and close packed hexagonal nanotube arrays are readily achieved. For patterned samples, the edge effect plays a significant role in control of the alignment and ordering of the nanotubes.

With further anodisation in the same acid electrolyte but at higher temperature the pores develop into nanotubes. As shown in Figure 5.7 highly ordered nanotube structures were formed on the pattern lines after further 1 or 2 hours anodisation at room temperature. As seen in the left panel in Figure 5.7, rectangular nanotubes are formed with thick walls after 1 hour at room temperature. Both the inside and the outside of the tube are rectangular. The location and distribution of the nanotubes are determined by the initial anodisation at low temperature shown in Figure. 5.6. After a further 2 hours anodisation, square nanotubes with large inner diameters are obtained while the outer diameter remains constant. It can be concluded that during anodisation, the outside tube morphology is formed first and this is followed by widening inside the nanotube. The most important observation is that the square nanotube morphology is preserved with a prepatterned sample. In contrast to the circular nanotubes, the walls between adjacent square nanotubes are shared and there is very little void in between the nanotubes. This can be clearly recognised from the image in the right panel of Figure 5.7. The anodisation rate on prepatterned surface is much less than that on non-patterned surface due to the lower effective exposed area, which reduces the anodisation current. With

high anodisation current, the electrolyte temperature increases and this accelerates the anodisation. The acidic electrolyte compensates for the reduced anodisation rate.

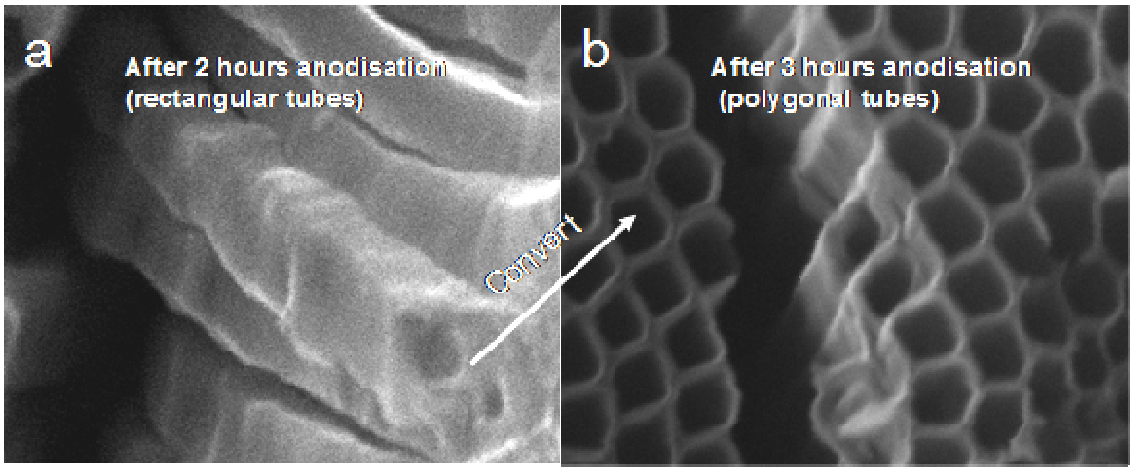

Figure 5.7 SEM images showing the change from (a) square to (b) polygonal TiO_2 nanotubes during the anodisation process.

In summary, the shape of the tubes could be controlled by surface patterning with EBL. The ordered nanopores observed at the initial stage of anodisation could be developed into square nanotubes. Further anodisation enlarged the inner diameter and reduced the wall thickness while the square morphology of the initial of the tube was retained.

5.4.7 The Formation of Multiwall TiO_2 Nanotubes

The diameters of the anodised nanotubes are determined by the anodisation voltages; the higher the voltage the larger the nanotubes. The voltage dependence is shown in Figure 3.12 in section 3.5.2 and is related to the thickness of the barrier layer. Thus by changing the voltage bias from low to high stratified layers have been generated [2]. Alternatively, the inner diameter of the nanotubes can be controlled by

altering the electrolyte temperature. The key problem for the two-step creation of multiwall nanotubes is that by increasing the voltage bias or electrolyte temperature in the second step, the nanotubes generated in the first step might suffer significant deformation, including enlargement of the inner diameter and breakdown by dissolution. Such deformation can be suppressed by either a reduction in the dissolving power of the electrolyte or by a protective organic layer coating.

In this study, we used a prepatterned Ti sample for two-step anodisation. On a prepatterned surface, the anodisation current was greatly reduced and the dissolution in the second step anodisation was reduced. In the two step process the first anodisation was with an electrolyte comprising 10 ml H_3PO_4, 1 ml of 4% HF and 100 ml of EG in ice (0-5 ˚C) and the second anodisation with an electrolyte comprising (0.6 wt% ammonium fluoride and 2 wt% (DI) water in 100 ml EG) at 22 ˚C. The low temperature anodisation created nanopores on the surface. The dissolution rate was maintained at low temperature by use of an acidic electrolyte. At low temperature, the ion mobility in the electrolyte is reduced and so is the electrolyte conductance. The effective voltage applied to the Ti sample is much less than the voltage bias, so that nanotubes with small diameters were achieved.

The second anodisation was carried out at room temperature with a neutral electrolyte. Multiwall tubes were formed within the line pattern. The SEM image in Figure 5.8a shows their morphology after 1 hour anodisation. Measured from the SEM image, the inner nanotube has an ID of 40 nm with a wall thickness of 35 nm, while the outer nanotube has an ID of 125 nm and a wall thickness of 30 nm. In many areas, the outer nanotubes are higher than the inner nanotubes. The difference is a direct result of

dissolution during the second anodisation. A gap between the inner and outer nanotubes is clearly observed.

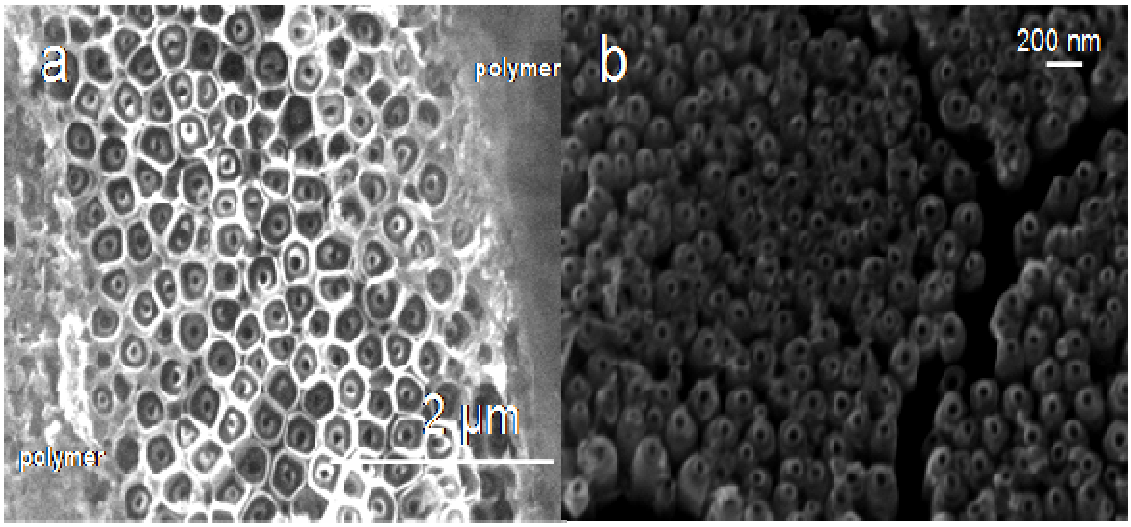

Figure 5.8 SEM images of TiO_2 nanotubes showing (a) multiwall nanotubes on a 4 μm wide line pattern. The top view of multiwall TiO_2 nanotubes shows the gaps between the tubes. In (b) the inner tube has grown, leaving the outer one as a shoulder.

With continuous anodisation for another hour, the height of the outer nanotube became lower than that of the inner nanotube, as shown in Figure 5.8b. The lip of the outer nanotube was lowered, the gap between the inner and outer nanotubes was diminished and the outer tube was left as a shoulder. This observation inspired us to create nanobottles with higher inner nanotubes as described in the next chapter.

The outer nanotubes in Figure 5.7a keep the polygonal and, in some cases square morphology. The alignment of tubes also remains the same as that of the initial pores in Figure 5.6. Such features directly reflect the influence of the prepatterning.

The current-time behavior was recorded (Figure 5.9) in order to understand the growth kinetics of multiwall TiO_2 tubes at different stages of anodisation. The current measured during the second anodisation was much higher than that in the first anodisation due to the temperature difference in the electrolyte. In the first step at low temperature, a rapid decay of current was observed at the beginning reflects the formation of an oxide barrier layer. The small anodisation current at low temperature is due to the low growth rate limited by dissolution. For the second anodisation at room temperature, a much higher current was observed, although there was no significant increase in surface area initially. Towards the end of the anodisation, the current increased, probably due to the combination of increased surface area as multiwall nanotubes were formed and increased dissolution rate at higher temperature. After the second anodisation the PMMA coating was intact.

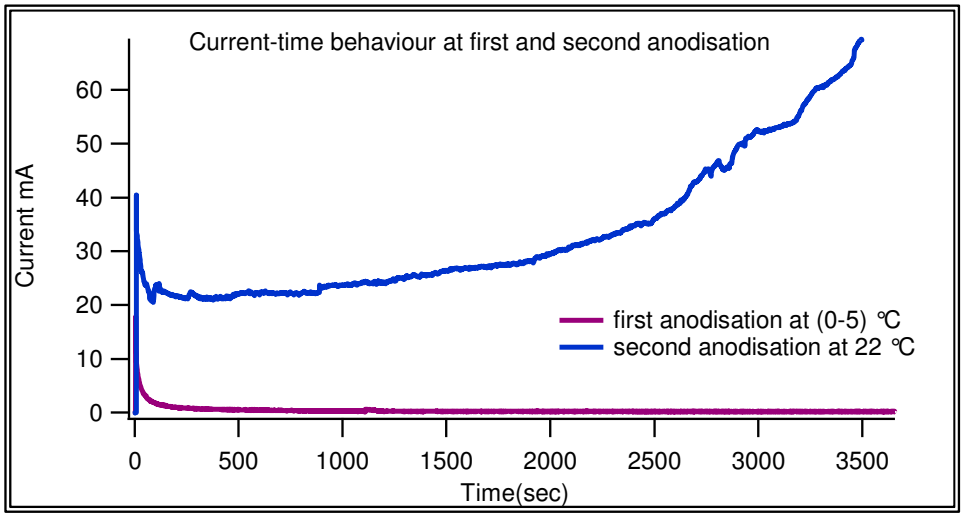

Figure 5.9 The transient current densities during the two-step anodisation for formation of multiwall nanotubes.

5.5 Conclusion

By use of a grid pattern obtained by EBL and a two step anodisation process both rectangular TiO_2 nanotubes and multiwall TiO_2 nanotubes can be obtained depending on the electrolyte composition in the second step. For an acidic electrolyte, the fast dissolution rate results in fast growth of square nanotubes. With a neutral electrolyte, slow dissolution results in slow growth and multiwall nanotubes are formed. The slower dissolution helps to preserve the inner nanotubes created by the first anodisation. The effects of the EBL patterning are two-fold. First, the area of exposed Ti surface is significantly reduced, which offers a better control of the anodisation process. Secondly the pattern influences the alignment and ordering of the final nanotubes.

Chapter 6 Production of Self-Ordered TiO_2 Nanobottles for Drug Release

6.1 Abstract

We report the preparation of TiO_2 nanobottles in which the inner and outer diameters vary from the tube mouth to the tube base. A two step anodisation was used to create the bottle neck and base separately by control of the anodisation temperature and voltage. We used a covalently bonded organic molecular monolayer coating to protect the neck. The experimental conditions for the formation of TiO_2 nanobottles are discussed. The potential application in drug release was suggested by a comparison between TiO_2 nanobottles and TiO_2 nanotubes. A biocompatible polymer, polyvinyl alcohol, was also used to control the release kinetics in aqueous media. Methylene blue was used to simulate the drug. The results show possibility of using nanobottle morphology to give longer times for the drug release than are possible from normal circular tubes.

6.2 Introduction

Titanium dioxide nanotubes show good biocompatibility, making them appropriate materials for use in drug release. However, their use as drug carriers is limited by uncontrolled release. The geometry of TiO_2 nanotubes as membranes makes them suitable for use as injected capsules or biomedical implants [177].

Xiao and his workers [178] showed the excellent biocompatibility of both TiO_2 nanotube arrays prepared by anodisation and annealed in a carbon atmosphere.

One of the objectives of the work described in this thesis was to control the morphology of titanium dioxide nanotubes in order to develop their applications in controlled drug release. According to Popat and co-workers [25] TiO_2 nanotube array were used for local delivery of antibiotics at the site of implantation. This demonstrated the prevention of bacterial adhesion while the osseointegration properties of the nanostructured surfaces were maintained. Precise control of the nanotube length and diameter enabled different amounts of drugs to be eluted at different rates at the implant site. However, in their work, only straight, normal circular TiO_2 nanotubes were investigated. Recently Song and co workers created amphiphilic TiO_2 nanotubes with a hydrophobic monolayer modification after the first step in the anodisation. These tubes could be used for biomolecules carriers, in which the outer hydrophobic barrier provides an efficient cap against drug release to the environment. By use of the photocatalytic ability of TiO_2, a precisely controlled removal of the cap and a highly controlled release of the hydrophilic drug payload was achieved under UV illumination [111].

Here, we have designed bottle-shaped nanotubes for control of drug release. The long neck with small diameter affects the rate of drug release, limited by mass transfer. In order to achieve effective control, the neck diameter should be less than 100 nm. We used two-step anodisation to create the neck and base in sequence. In order to protect the morphology of the neck, an organic hydrophobic monolayer coating was applied after the first step in the anodisation. The diameters of the neck and base were controlled by the combination of anodisation temperature and voltage. The effects of anodisation voltage and electrolyte temperature have been discussed in section 1.2.4.6

and section 1.2.4.1. Our measurements confirmed that an increase in the voltage bias led to an increase in the diameter of TiO_2 nanotubes, as shown in section 3.5.2.

In order to study the release of the drug from nanobottles further, we chose biocompatible and water soluble polymers to cover the nanobottles loaded with drug. Polymers for use in drug release must be biodegradable, *i.e.* they must be broken down to non toxic monomers inside the body. They must also be biocompatible they *i.e.* must be remain biologically inert during implantation. The rate of drug release is controlled by dissolution of the polymer, which depends on its solubility and thickness.

Herein, the control of drug release was managed by two methods. First the release was controlled by the thickness of the polymer layer. TiO_2 nanotubes alone give only limited control of release rate. A polymer coating delays the initial release depending on its thickness. This was quantitatively studied. Secondly, nanobottles with a long narrow neck at the top and wide base at the bottom were developed. The loading capacity is controlled by the volume of the base and the release kinetics are determined by the inner diameter and length of the neck.

6.3 Preparation of TiO_2 Nanobottles

To create the appropriate nanobottle morphology, a titanium plate was prepared by the method described in section 2.2 and anodised in a homemade electrochemical cell with a second titanium plate as the cathode. The electrolyte was prepared from 10 ml H_3PO_4, 1 ml HF and 100 ml ethylene glycol. The electrode separation was 60 mm. and the surface area exposed to the electrolyte was approx 2.0 cm^2. Anodisation was carried out in two steps with controlled anodisation duration, voltage and electrolyte

temperature. The first anodisation was made with the temperature of the electrolyte between 0 °C and 5 °C. Then a hydrophobic layer was deposited by refluxing the sample in 2 mM octadecylphosphonic acid (ODPA) in toluene at 70 °C for at least 10 hours. The phosphonate formed a self-assembled monolayer (SAM) on the surface of the TiO_2 nanotubes. In order to confirm the attachment of ODPA, water contact angle measurements were carried out as function of the reflux duration. Each measured contact angle was an average of 10 measurements. The contact angle was measured by Image J software as the angle between the drop of water and the surface of the amorphous TiO_2 nanotubes. The phosphorus was also monitored by energy dispersive X-ray spectroscopy (EDX).

The base of the TiO_2 nanobottle was created by the second anodisation at 22 ± 2 °C the higher the temperature, the grater the diameter of the base. The ODPA coating protected the bottle neck created in the first anodisation process. The morphology of the titanium film made by two step anodisation was monitored by scanning electron microscopy (SEM (JSM 820M, Jeol) operating at 30 kV) and a transmission electron microscopy (TEM (Hitachi-7100) operating at 100 kV).

For comparison, titania nanotubes were also fabricated by anodizing a titanium plate in a single step with an electrolyte composed of 0.6 wt% ammonium fluoride and 2 vol% deionised water in ethylene glycol. The pore size was controlled by the applied potential and the tube thickness by the anodisation duration.

6.4 Results and Discussion

The synthesis of TiO_2 nanobottles involved three stages: the preparation of the TiO_2 bottle neck, surface modification with an organic attachment, and a second anodisation to create the base of the nanobottle. In the following sections, we discuss the technical details of the creation of nanobottles and the parameters that affect their morphology.

6.4.1 Synthesis of the Neck of the TiO_2 Nanobottle

The neck of the nanobottle is characterised by a small inner diameter. Anodisation of a polished titanium plate in an acidic fluoride-containing electrolyte at 0-5 $^{\circ}$C resulted in the production of self-organised nanopores. A typical sample is shown in Figure 6.1. Here, the anodisation time was 1 hour with bias of 60 V. With a lower bias, nanopores with smaller diameter could be formed.

The measured inner diameter (ID) of the pore is about 40 nm and outer diameter is about 200 nm. Strictly speaking, only nanopores, not nanotubes were formed. In one of the studies conducted by Enachi *et al* these pores were shown to be but their morphology might have been dependent on the particular electrolyte used, and the interconnected is not present in nanopores made in other electrolytes [179].

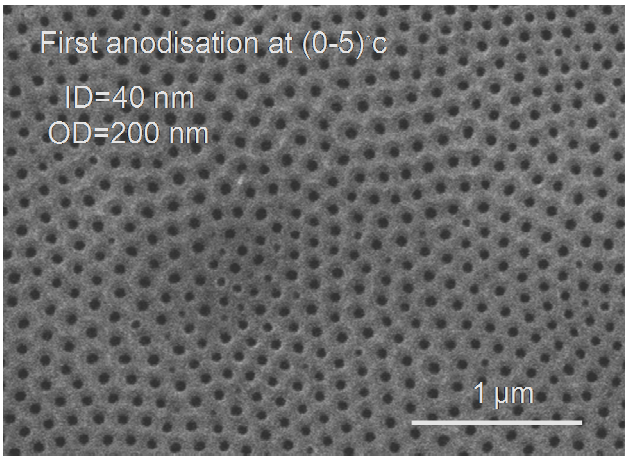

Figure 6.1 SEM image of TiO_2 nanopores with ID = 40 nm, OD = 200 nm prepared by anodisation of a titanium sample in an acidic electrolyte at low temperature (0-5 °C) for 1 hour at 60 V bias.

In our case, we found that the walls of the pores remained connected intact in spite of the fact that the pores were converted into tubes, till the end of second anodisation.

6.4.2 Modification of TiO_2 Nanotube Surfaces with ODPA

The initial nanotube array formed the necks of the nanobottles. In order to protect the necks from etching during the second anodisation, an ODPA monolayer was deposited on the surface of the porous structure formed in the first anodisation. The self-assembled monolayer of ODPA consists of vertically aligned ODPA molecules in which the phosphonate head group is covalently bonded to the surface of the nanopores and the long hydrocarbon chain gives a hydrophobic surface. The attachment typically occurs at hydroxide-terminated surface sites by condensation with phosphonate, to give covalent bonds between substrate oxygen and the anchor group. In this experiment, the sample was heated under reflux with 10 mM ODPA solution for 10 hours at 70 °C.

The surface of the TiO_2 nanopores prepared by anodisation has good wetting properties. After coating with an ODPA monolayer, the surface becomes hydrophobic. The wetting was characterised by the contact angle between drops of water and the TiO_2 nanotube surface [180]. If the contact angle between the drop of liquid and the titanium surface is less than 90 degrees, the liquid is said to wet the solid. If it is greater than 90 degrees, it is said to be non-wetting. A zero contact angle represents total wetting.

Contact angle measurements were made for TiO_2 arrays that had been treated for various reflux durations in an ODPA toluene solution. Figure 6.2 shows the contact angle as a function of reflux time. The water contact angle increases rapidly in the first hour, then slowly approaches saturation after 10 hours.

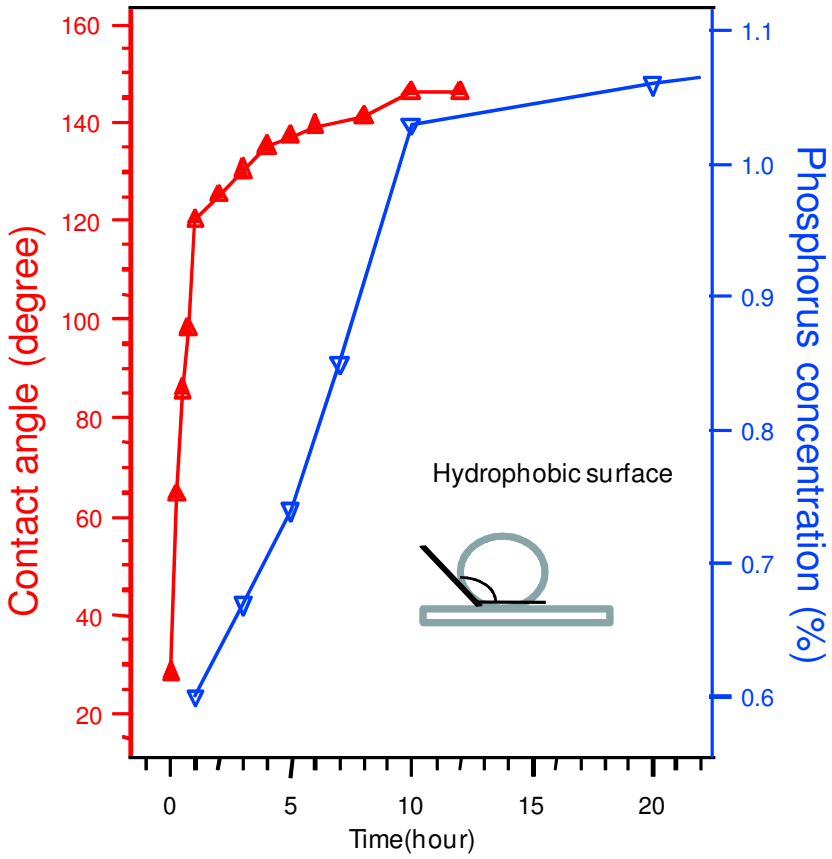

Figure 6.2 Variation of contact angle (Red line), and EDX analysis of % P relative to Ti (blue line) with reflux time.

We also used EDX to monitor the P/Ti ratio Figure 6.2. Surprisingly, the phosphorus concentration increases almost linearly as a function of reflux time. After 10 hours, the phosphorus concentration reaches saturation and there is no further up take of ODPA. The measured contact angle is contributed by the topmost surface and the inner wall surface of the nanotube.

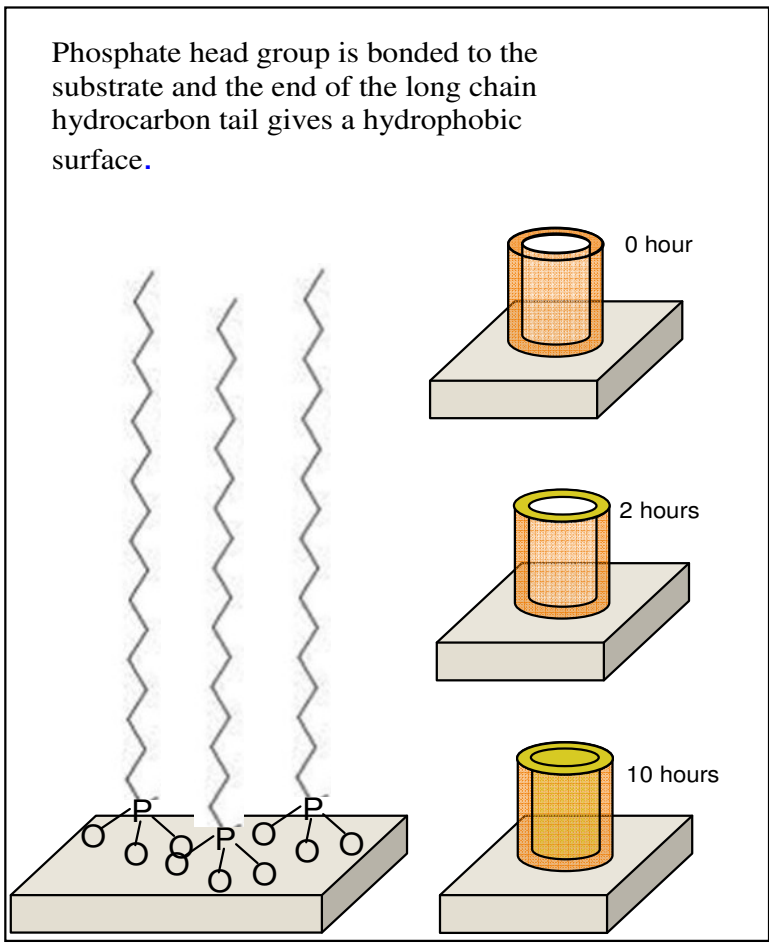

Figure 6.3 The formation of monolayer of ODPA on the surface of the tubes after 1 hour of reflux in ODPA solution. Further refluxing will forms an ODPA coating on the inside walls of nanopores shown by the approach of the water contact angle to its maximum.

We propose that after the first hour, a monolayer of ODPA is formed on the topmost surface of the nanopores resulting in a rapid increase of the contact angle. Further reflux results in the penetration of ODPA into the nanotubes to give an organic monolayer on the inside walls. In this process, the contact angle increases at a slower rate, due to the limited mass transport through the 40 nm pore. In EDX measurements, the beam can penetrate about 1 μm under the surface, so that. Phosphorus signals from

both the topmost and inside wall surface are measured simultaneously. Thus a smooth linear increase in the phosphorus signal was observed. After 10 hours, both the inside and the outside of the nanopores are covered with ODPA and there is no further increase of contact angle and phosphorus signal. The proposed ODPA deposition process is illustrated in Figure 6.3.

The purpose of the ODPA coating is to reduce the dissolution rate of the TiO_2 nanotubes and prevent enlargement of the inner diameter of the bottle neck during the second anodisation. The ODPA coating is crucial in forming the tube neck. Our experiment demonstrated that even with a high voltage (120 V) in the second anodisation, the tube mouth was not enlarged, and that tubes with a narrow inner diameter were retained after the first anodisation, even though, with the high voltage in the second anodisation, there was partial oxidation of ODPA.

6.5 Anodisation Parameters to Control the Shape of the Tubes

The control of anodisation parameters is essential for control of the tube morphologies. Here, various anodisation parameters were studied in order to create TiO_2 nanobottle shapes. Parameters such as electrolyte temperature, anodisation voltage and anodisation time were tailored in order to control the bottle morphology.

6.5.1 Temperature

Anodisation at various electrolyte temperatures has been used to control nanotube dimensions. Figure 6.4a and b show the current-time behavior for both first (low temperature) and second (room temperature) anodisation environments. In the first anodisation at 0-5 ºC the initial current is low due to limited mobility of fluoride anions

at low temperature and as a result only a slow etch is achieved. Although the applied potential is 100 V the inner diameter does not exceed 40 nm. The initial increase in the current is due to the oxidation of water, similar to that at room temperature reported in section 3.3.4. During the second anodisation, a much higher current was observed due to the increased dissolution rate at 22 ± 2 ˚C. The small inner diameter obtained at low temperature is ideal for a bottle neck.

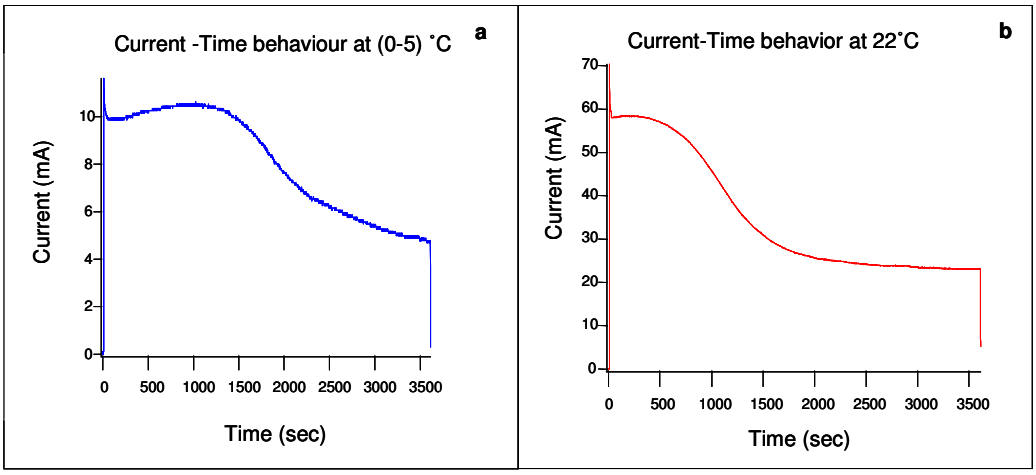

Figure 6.4 Current-time behavior at (a) 0-5 ˚C and (b) room temperature (22 ˚C).

6.5.2 Voltage

Here, we study the control of nanobottle morphology by changing both the anodisation voltage and the electrolyte temperature in a two-step anodisation. The increased voltage during the second anodisation drives the ions inside the preformed tubes and through the ODPA monolayer coating added after the first anodisation. The tube walls are, to a certain extent, protected against the etching effect of soluble

fluorides. The parameters chosen for the preparation of the titanium dioxide nanobottles are listed in Table 6.1.

Table 6.1 Parameters for formation of nanobottles.

Exp. number	Initial voltage (V)	Initial temperature (°C)	Duration (min)	Voltage at 2nd stage (V)	Final temperature (°C)	Duration (min)	The final tube shape
1	100	0	60	100	25	60	Tube with neck
2	100	0	60	120	25	20	Conical shape
3	60	0	60	120	25	20	Nanobottle
4	60	0	90	120	25	20	Nanobottle

To investigate the effect of temperature only, the anodisation voltage was kept at 100 V during both anodisation stages. Figure 6.5a and b show the morphology of the nanobottles after two step anodisation. The neck of the nanotube formed from the first step anodisation at low temperature is narrower than the base of the nanobottle anodised at room temperature. Although the differences in diameter between the neck and base are not very great, the morphology may be classified as tube with neck.

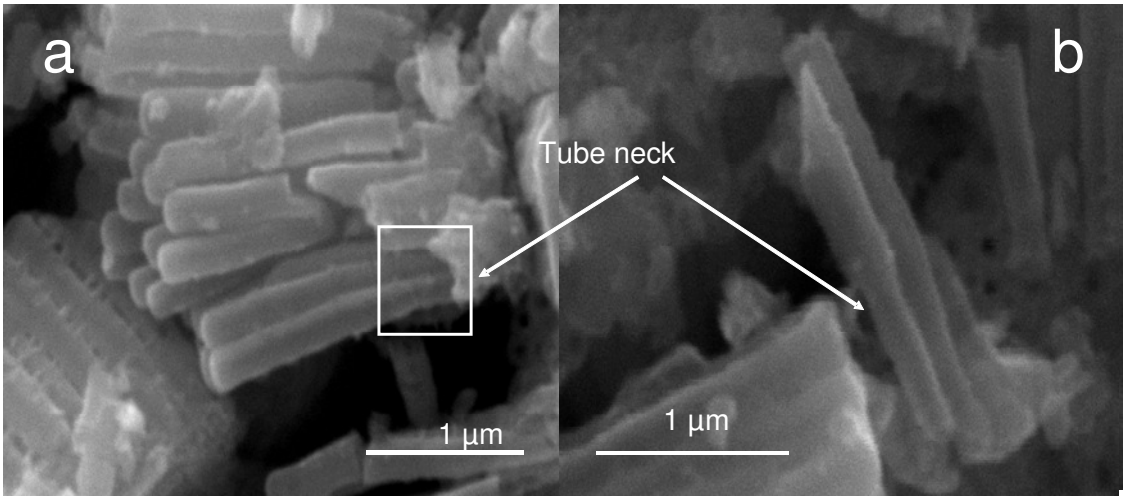

Figure 6.5 SEM images showing (a) formation of the neck (narrow diameter), (b) individual TiO_2 nanotubes with clear formation of the neck.

A good nanobottle should have a narrow neck and a wide base. In our attempt to achieve a better bottle morphology, a long anodisation time for the first anodisation step to form the neck, together with an increased voltage for the second anodisation to give wide tube base, was tried. Figure 6.6 displays the results of Exp 2.

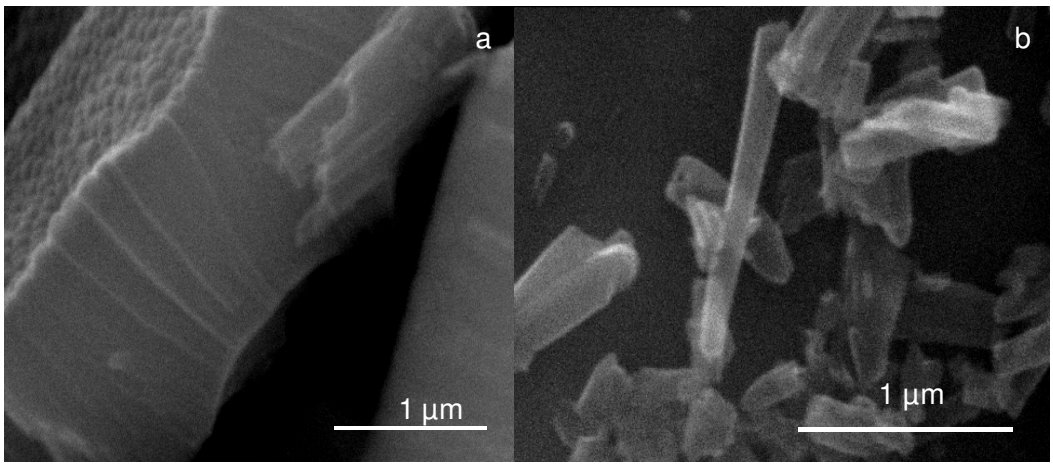

Figure 6.6 SEM images of TiO_2 nanotubes (a) side view and (b) conical shape of a TiO_2 individual nanotube.

Instead of nanobottle, a conical shaped nanotube was formed. Changing the voltage had produced a wider bottom.

From the results of Exp. 1 and 2, it is clear that the increase of the anodisation voltage from the first to the second step is important for the formation of a wide base and that the ODPA coating is effective in protecting the neck. In Exp 3 and 4, we reduced the voltage to 60 V in the first anodisation, and 120 V was used in the second step. Figures 6.7a and b show SEM images of nanobottles achieved under the conditions in Exp 3 and 4 respectively. In Exp 3, the time of first anodisation was 60 min and in Exp 4, the anodisation time was 90 min. The successful creation of good nanobottles is demonstrated by the very narrow diameter (30 nm) of the neck between the tube top and tube base observed in both Figures 6.7a and b.

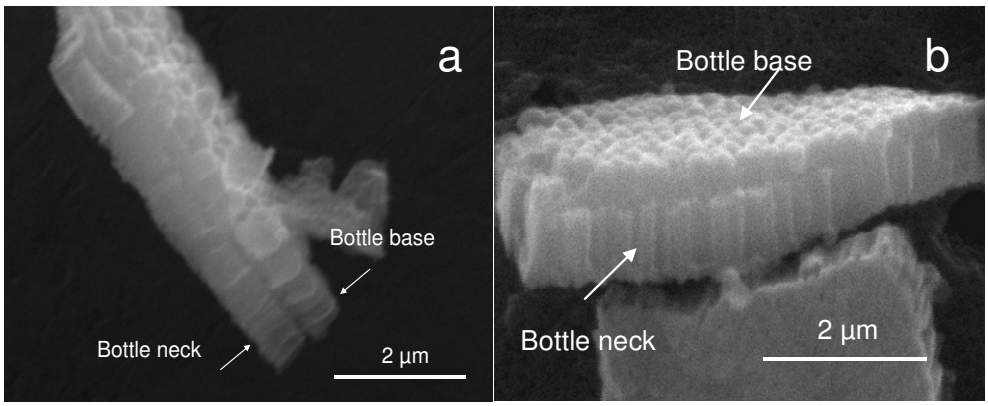

Figure 6.7 (a) SEM images of TiO_2 nanobottles from exp 3 and 4 respectively. In (a) the bottle neck length was controlled by the time of the first anodisation step. In (b) the nanobottles show the long necks from lengthening the time in the first anodisation step.

The base, formed in the second anodisation at high voltage and high temperature, is significantly wider than the neck. For individual nanotubes, the inner tube diameter measured from the tube mouth from the first anodisation stays constant throughout the second anodisation. Thus the protection by ODPA was effective. The lengths of the necks in Figure 6.7a are 850 nm, shorter than those in Figure 6.7b (1300 nm). The difference is a direct result of the difference of the anodisation time in the first step (60 min *vs* 90 min). However, the base lengths and diameters for the nanobottles are almost identical. The length of the neck seems to have no significant effect on the anodisation in the second step.

Figure 6.8 summarises the morphology of nanotube and nanobottles created under the conditions listed in Table 6.1. When the difference in anodisation voltage between the first and second step is not large enough, only conical nanotubes are formed. The duration of the first anodisation affects the length of the neck; the longer the anodisation, the longer the neck.

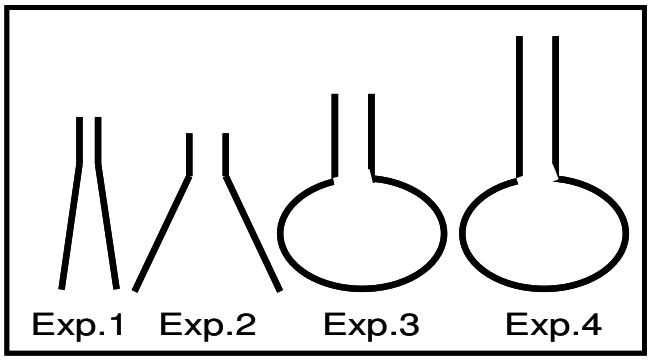

Figure 6.8 Schematic representation of tubes formed with experimental parameters as shown in table 6.1.

The accurate dimensions of a nanobottle were measured on a separated single bottle, shown in Figure 6.9a. The neck had an ID of 40 nm, an OD of 124 nm and the length was 221 nm. The base had a width of 330 nm and a length of 410 nm. The measured neck length is less than that observed from the side-on SEM image in Figure 6.7a possibly because of some of neck was broken off from the bulk. TEM images also confirmed the dimension of nanobottles as seen in Figure 6.9b and c.

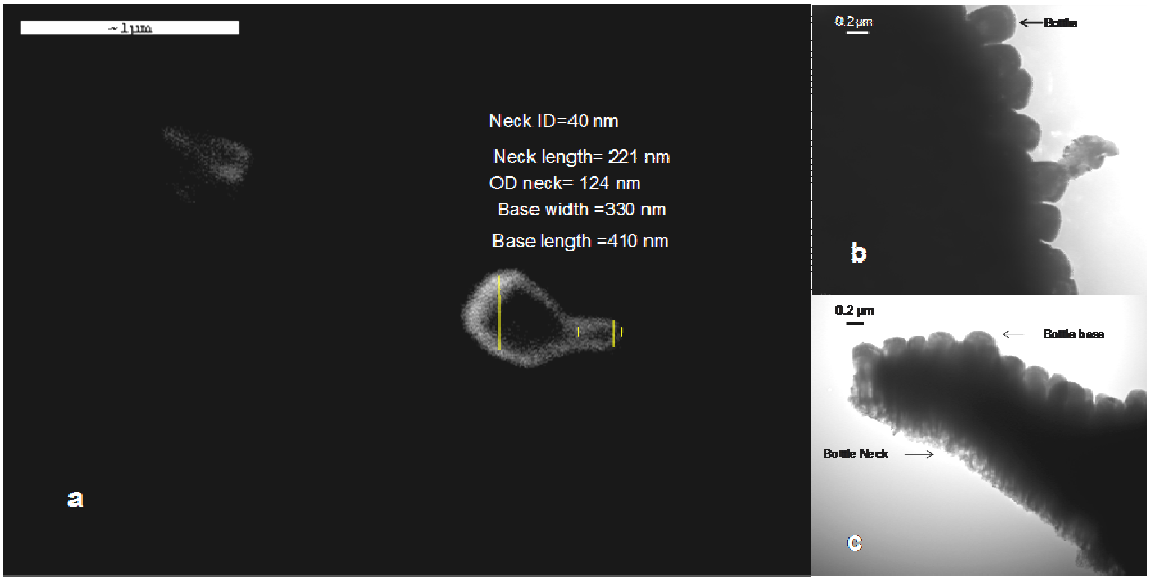

Figure 6.9 (a) SEM image of an individual TiO_2 nanobottle (b and c) TEM images showing side view of TiO_2 nanobottles.

The same experiment without an ODPA coating yielded nanobottles with much shorter neck, as shown in Figure 6.10. Figure 6.10b shows a magnified side view of the nanobottles. Some bottles are formed with broken necks as a result of significant dissolution in the second anodisation at room temperature and high voltage. Therefore,

in order to create a well shaped nanobottle, it is essential to protect the bottle neck with a coating of ODPA.

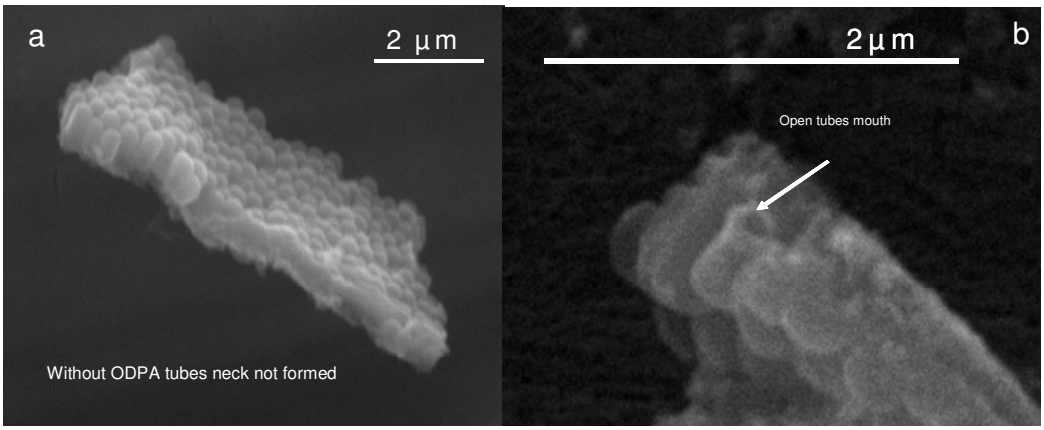

Figure 6.10 (a and b) SEM images of TiO_2 nanobottles produced by two-step anodisation without ODPA protection.

6.6 Application in Drug Release

Here, the aim of my study was to use the morphology of nanostructures, including nanotubes and nanobottles to control drug release. The bottle shape makes it possible to control the maximum loading and the release kinetics independently.

6.6.1 Methylene Blue Loading

Standard open TiO_2 nanotubes have been studied as possible drug delivery vehicles filled with antibiotics [178]. The purpose of developing nanobottles for drug release is to increase the drug loading and to slow the drug release kinetics. The ability to manage these properties gives significant opportunities for clinical applications. In this study, methylene blue (MB) was used as a convenient drug because it is a

monoamine oxidase inhibitor (MAOI). Its molecular structure is similar to those of chlorpromazine and typical antipsychotics, which are infused intravenously at doses exceeding 5 mg/kg. It is the basic compound from which chlorpromazine and many other antipsychotics are made [181]. The concentration of released MB can be easily monitored by its absorbance at 663 nm [182] with a standard UV-Vis spectrometer.

Various methods are used for loading chemicals into nanotubes. For example, the drug may be pipetted on to the TiO_2 nanotube surface in order to cover the surface with the drug solution gently [178]. A careful flushing with appropriate solvent is necessary to remove excess chemicals on the surface without causing chemical loss inside the nanotubes. Chemicals can also be introduced to by soaking the nanotubes in solution under vacuum condition followed by flushing, under vacuum condition, the gas trapped in the nanotube can be released and allowing a more efficient chemical loading achieved [183]. In either method, the sample has to be completely dried before kinetic measurements.

In our experiments samples of titanium dioxide nanotubes and nanobottles were immersed for several days in 500 ppm aqueous methylene blue solution, prepared from 0.02 g of MB in 40 ml water. The loaded TiO_2 nanotube arrays were then rinsed with water on a rotating spinner in order to remove the dye from the surface. After filling and rinsing, the TiO_2 nanotubes arrays were left to dry in the air or under vacuum. All operations were carried out at room temperature.

6.6.2 Polyvinyl Alcohol (PVA) Coating

As a biocompatible polymer, PVA was used to coat the surface of the loaded TiO_2 nanotubes, in order to develop additional control of the chemical release kinetics. The PVA polymer solution (1% w/v) was made up in a mixture of water and ethanol (1:1) and then stirred for 4 hours. The addition of ethanol accelerates the drying of the PVA coating. After filling the TiO_2 nanotubes with MB, PVA was coated on to the nanotube surface with a spin coater. An aliquot of PVA solution was applied to the surface and spun for 5 min at 300 rpm. The thickness was controlled by the solution concentration and spin rate. With a fixed solution concentration and spin rate, we could control the thickness by the number of coats. The release kinetics of MB were studied as a function of PVA film thickness.

6.6.3 The Release kinetics of Methylene Blue

Standard drug release measurements, are usually made in media such as water, or saline or other buffered aqueous solutions [184]. In our experiments, the methylene blue release kinetics were measured in 20 ml deionised water at 22 $^{\circ}$C. The concentrations of released MB were measured by UV-Vis spectrometry at 663 nm where the MB has maximum absorbance. Under controlled conditions, MB elution was measured at various times up to 4 weeks, after which the MB concentration reached a plateau and release finished. The MB was released quickly during the first hour and completely within 4 weeks. The absorbance of the released MB solution was stable for more than three months. This indicates that methylene blue dye did not degrade in aqueous solution. We found that drug elution was most profoundly determined by parameters such as tube diameter, tube length and loading time. The release involved diffusion of

the MB entrapped in the nanotubes through the polymer coating. The parameters that affect the release rate are discussed in the following paragraphs.

6.6.3.1 The Layer Thickness

Concentrated PVA solutions have high viscosity and give thick films, which require long drying times. In addition, the films may not be sufficiently homogeneous. For these reasons dilute PVA aqueous solutions (1 w/v %) were used to give good quality spin coating. The thickness of the PVA film was controlled by multi-step coating-drying cycles, and was measured by SEM. The results, presented in Figure 6.11, show the thickness of the PVA coating as a function of the number of coats applied.

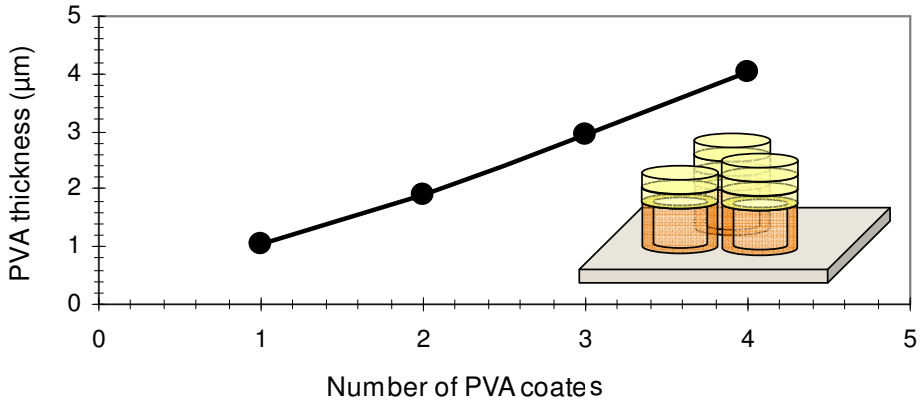

Figure 6.11 Plot of the thickness of the PVA layer against number of coatings with 1 % w/v solution.

The data shows a linear dependence of PVA thickness on the number of coats. Each layer of coating increases the thickness by 1.0 µm. The linear relationship gives excellent control of the film thickness.

The thickness of these PVA layers on the mouth of the TiO_2 nanotubes can be used to control the release of MB. Figure 6.12 shows the release of MB as a function of PVA thicknesses ranging from 1 to 3 μm. On each elution curve, the release kinetics can be defined by three linear stages. Within a very short initial period (less than 1 min), there is rapid release of a small amount of MB attributed to uncoated areas at the edge of the Ti plates. There is then slower release of MB within 20 min of submerging the sample in water. The release rate at this stage depends on the thickness of the PVA coatings; thicker coatings result in slower release. The MB release is related to the dissolution of the PVA film. Due to the hydrophilic nature of MB, there is always some leaching of MB from the top of the nanotubes into the PVA films. Once the PVA films are dissolved, the release rate become independent of the polymer film thickness, and is controlled only by the diameter and length of the nanotubes. This can be clearly observed in Figure 6.12.

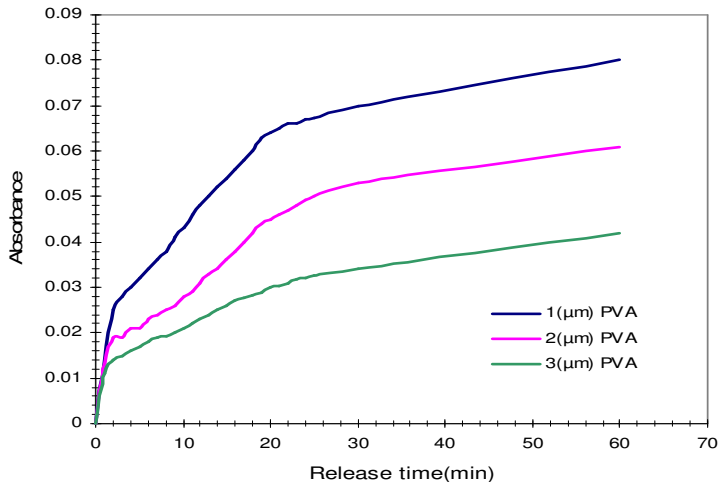

Figure 6.12 The release kinetics of MB from TiO_2 nanotubes with PVA coatings of different thicknesses.

The function of the PVA coating is to delay the release of MB in the third stage. In our experiments, with the PVA thicknesses we used the delay was small because of the high solubility of PVA. The delay would be expected to be greater with less soluble biocompatible polymer coatings with lower solubility.

6.6.3.2 Tube Length

One of the advantages of using anodised TiO_2 nanotubes for controlled drug release is that both the diameter and length of the nanotubes can be independently controlled by the anodisation procedure. For a fixed anodisation time and voltage, the longer the anodisation time, the longer the nanotubes. The kinetics are affected by both the diameter and length of the nanotube. With a fixed diameter, shorter nanotubes give faster release. The dimensions of the nanotubes may be measured from SEM images.

The MB release kinetics from TiO_2 nanotubes with different lengths are shown in Figure 6.13. The nanotubes were created by anodisation in NH_4F/EG solution with a bias of 100 V at room temperature. After 30, 60 and 90 min nanotubes with lengths of 5.5, 11.1 and 18.5 μm, respectively were obtained.

As the release follows a diffusion mechanism which is proportional to the concentration of the loaded drug, it is reasonable to assume that the MB release follows first order kinetics. Under such conditions, the release kinetics can be fitted by the equation: $I = A_0 [1- \exp (-Kt)]$, in which I is the absorbance elution, A_0 is the saturated absorbance (maximum loading), t is the release time and K is the release rate constant. The drug release can also be normalised against the maximum drug release A_0. Figure 6.13 shows kinetic measurements of the normalised drug release. After fitting to the

first order kinetics, the rate constants (in units hour $^{-1}$) of 11.1, 6.3 and 1.25 were found for nanotubes with lengths of 5.5, 11.1 and 18.5 µm respectively. These confirm that the release rate is faster for shorter nanotubes. The kinetic behavior shows that drugs diffusing into the solvent from shorter nanotubes have less distance to travel.

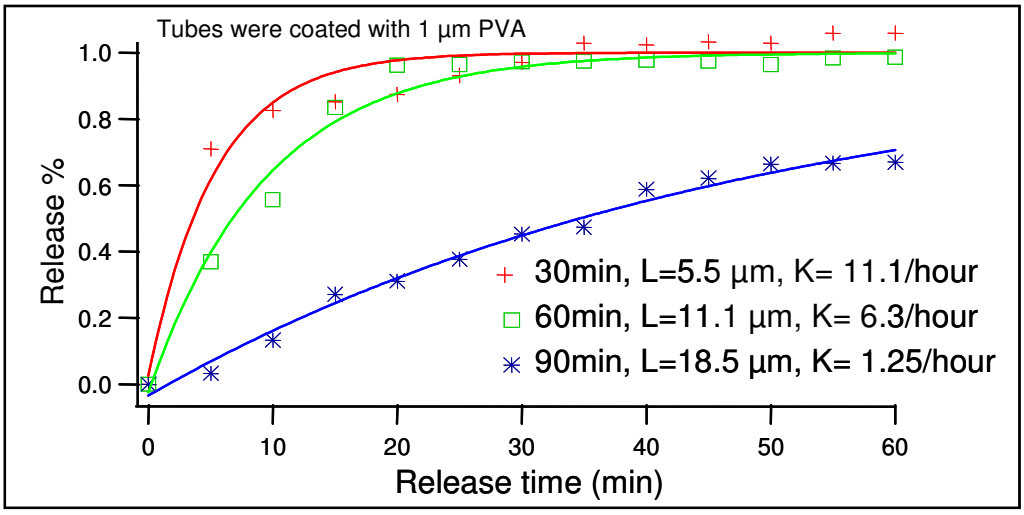

Figure 6.13 Release patterns from tubes of different lengths anodised at 100 V.

The curves in Figure 6.13, show that longer nanotubes have higher loadings of MB, defined by the area under the curve. This offers the possibility of controlling the loading capacity of the nanotubes in addition to the release kinetics.

6.6.3.3 Tube Length and Diameter

For a fixed anodisation time, higher voltages give nanotubes of greater diameter and length. The diameter increases linearly with the applied voltage. However, that is not true for tube length, as explained in chapter 3. The dimensions of the nanotubes were measured from SEM images. We used of voltages of 40, 60 and 100 V. With a bias of 40 V for 1 hour anodisation, nanotubes with inner diameter of 55 nm and total

length of 1.2 µm were observed. For anodisation at 60 V for 1 hour, the ID was 70 nm and the length 2.2 µm. With 100 V anodisation, the tube ID increased to 110 nm and the length to 10 µm. For a valve metal, the increase in the tube diameter is directly related to the thickness of the barrier layer, which is proportional to the anodisation voltage. Normally, at higher voltage, the rates of oxidation and dissolution at the bottom of the nanotube are also higher, giving a higher anodisation current. This in turn increases the electrolyte temperature and anodisation rate. Figure 6.14 shows the MB release kinetics from nanotubes with different diameters and lengths.

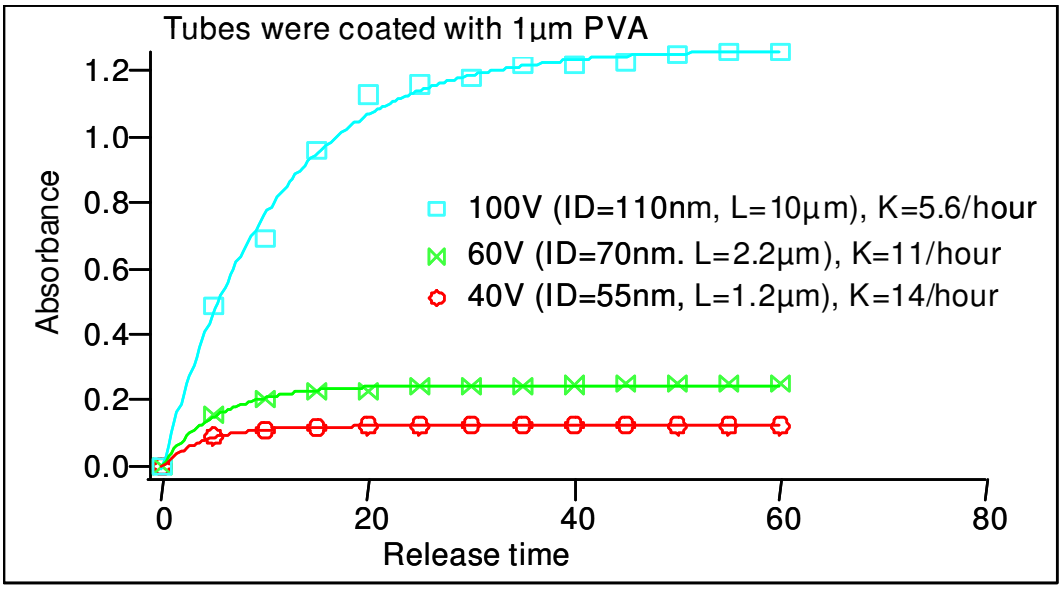

Figure 6.14 Release patterns from tubes with different diameters. The tubes were anodised at different voltages for an anodisation time of 1 hour.

It is clear that larger and longer nanotubes have higher MB loadings. In nanotubes made at lower bias (40 V), the release rate is faster than that from nanotubes anodised at higher voltage. The measured rate constants are 14, 11 and 5.6 h^{-1} for nanotubes created at 40, 60 and 100 V, respectively. The nanotubes made at higher voltage have larger diameter, and should therefore give faster release. This is contradictory to what we

observed and it implies that the effect of tube length overrides that of tube diameter under our experimental conditions.

6.6.4 Comparison between Nanobottles and Nanotubes

With two step anodisation and use of an organic coating, we were able to create bottle shaped nanostructures, which offer additional means for control of drug release kinetics. In Figure 6.15, we show a schematic diagram of a complete sequence including synthesis of nanobottles, drug loading, encapsulating nanobottles with polymer coating and release of MB.

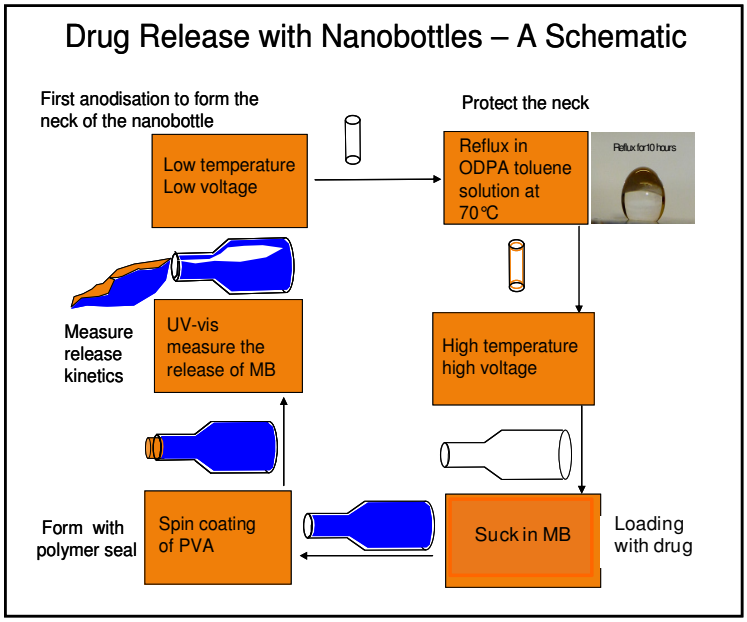

Figure 6.15 Schematic diagram showing the synthesis of TiO_2 nanobottles, loading with MB, coating with polymer and the drug release process.

In this part of the thesis, a direct comparison of the MB release kinetics is made between nanotubes and nanobottles in order to demonstrate the influence of the nano morphology on drug release.

The release of MB from both nanotubes and nanobottles is shown in Figure 6.16. The nanotubes were created by anodisation for 1 hour at 60 V in an electrolyte of 0.6% ammonium fluoride, 2% water in EG. These nanotubes have IDs of 80 nm and are 3.5 µm long. The nanobottles were created by two-step anodisation and had necks of 40 nm ID and lengths of 350 nm. The base was formed with a wider ID of 350 nm and length of 815 nm. In both cases, a layer of PVA 1 mm thick was spin-coated on to the surface after the loading of the MB. The release of MB was measured during a period of 2 weeks.

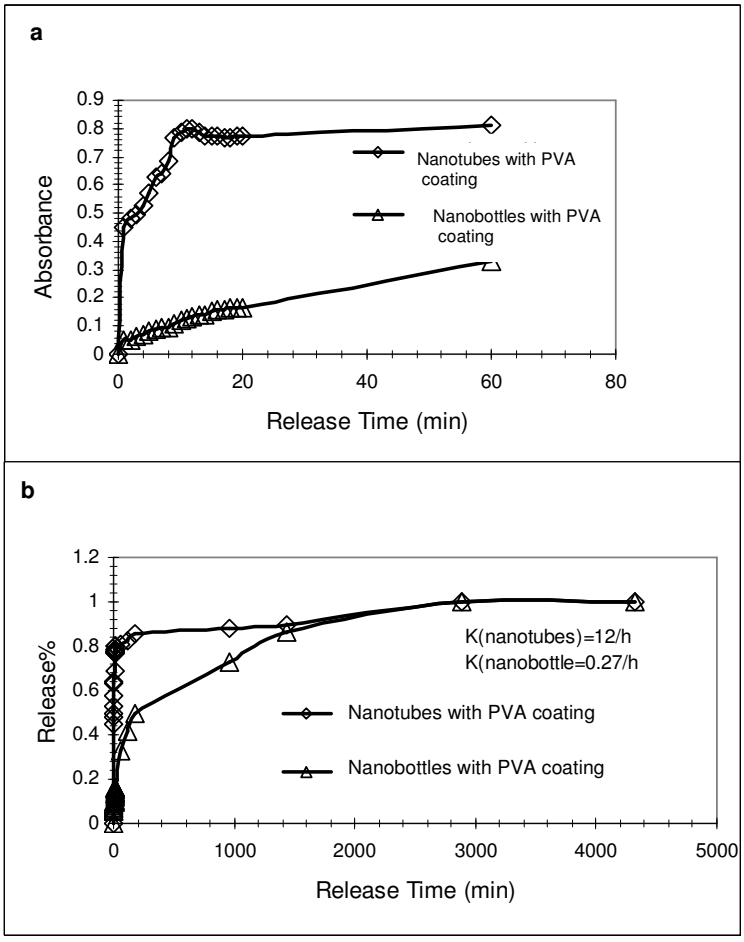

Figure 6.16 (a) Release of MB from nanobottles and nanotubes; (b) comparison of % release of MB between nanobottles and nanotubes.

Figure 6.16a shows the initial MB release from both nanotubes and nanobottles. A much slower MB release was observed for the nanobottles; for the nanotubes, the release was complete within 10 min in contact with water. This is also clearly demonstrated in Figure 6.16b which displays measurements shown over 3 days. For nanobottles, a gradual release of MB was observed over 3000 min (2 days). Thus, the release of MB is much slower from nanobottles than from nanotubes, indicating that the narrow neck of the nanobottle controls the drug release. From the first order drug release kinetics we estimate the release rate constant for nanotubes as 12 h^{-1} and for nanobottles of 0.27 h^{-1}. These rate constants suggest that the time for release of 50% of MB (half life) is 3.5 min for nanotubes and 154 min for nanobottles.

MB release with and without the PVA coating, is shown in Figure 6.17. The release of MB from TiO_2 nanobottles is extended by the use of a PVA coating. The release rate constant from the nanobottles without PVA coating is about 10 h^{-1} which suggests an even slower release than that from the PVA coated nanotubes (12 h^{-1}).

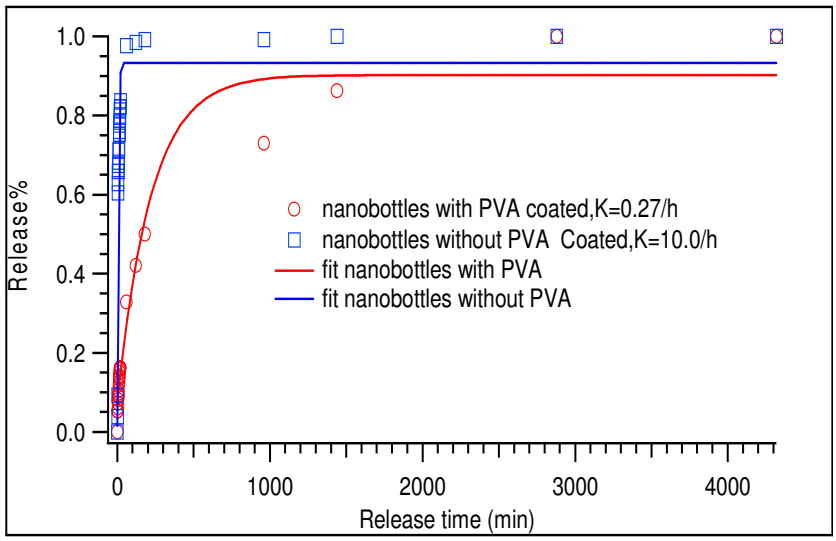

Figure 6.17 % Release of MB by using various nanobottle arrays, coated and uncoated with PVA.

This delay in MB release is clearly related to the dimensions of the bottleneck which is very important for control of the kinetics of the release. We expect that a narrower ID and longer neck will reduce the overall MB release rate and that the volume of the base of the nanobottles will determine the total loading of the drug within the nanostructures.

6.7 Conclusions

We have shown that it is possible to make TiO_2 nanobottles by use of two-step anodisation. To the best of our knowledge, this is the first time that the synthesis of TiO_2 nanobottles has been described. The application of nanobottles in drug release confirms that the nanobottle shape effectively delays the drug elution compared with nanotubes of uniform diameter. In addition, the release of drugs from both nanotubes and nanobottles can be controlled by use of PVA coatings.

The bottle shaped nanotubes were created by initial anodisation at low temperature and low voltage. The narrow neck was protected by a coating of ODPA. The base of the nanobottle was created by a second anodisation at room temperature and higher voltage. By a combination of electrolyte temperature and voltage the overall shape of the nanobottles can be precisely controlled. Further investigations are underway to discover how the shape of the nanobottles can affect the drug loading and release kinetics.

PVA polymer coatings can also be used to slow down the overall release from both TiO_2 nanobottles and nanotubes. Such effects are directly related to the water

solubility of the polymer coating. In further experiments various other polymers will be investigated to evaluate their influence on the kinetics of drug release.

Chapter 7 Applications of TiO_2 Nanotubes in Water Splitting and Degradation of Organic Compounds

7.1 Abstract

TiO_2 nanotubes with two different morphologies, polygonal and circular, were chosen for investigation as photoanodes in a photoelectrolysis cell (PEC) for water splitting. The photoenergy was converted into, and stored as, chemical energy in the form of hydrogen and oxygen gas. The efficiency of hydrogen generation by the addition of organic compounds as electron donors was also investigated. These donors react irreversibly with the photogenerated holes in the valence band and enhance the photocatalytic activity by reducing the electron-hole recombination rate.

7.2 Introduction

The development of renewable energy sources helps to reduce CO_2 emissions and to reduce the dependence on limited reserves of fossil fuels. Hydrogen produced from water using solar light is a clean, renewable, and sustainable source of energy and its use could provide a critical breakthrough in efforts to reduce environmental pollution caused by the use of fossil fuels. Burning hydrogen results in the generation of water, which neither results in air pollution nor leads to the emission of greenhouse gases [94].

A system for photocatalytic hydrogen production [185] by splitting water must not only absorb solar light but also efficiently convert photon energy into chemical energy. Many efforts have been focused on the creation of nanostructured

photocatalysts in order to increase the efficiency for hydrogen production from solar energy.

By exposing a TiO_2 nanotube photoanode to UV light, electron (e^-) and hole (h^+) pairs are generated in the conduction and valence bands respectively of the semiconductor. The excited electron moves from the CB moves to the external circuit and reaches the cathode (in this case Pt). Meanwhile, the corresponding positively charged hole comes out from the nanotube surface to the electrolyte solution (in this case, 1M KOH in water) and oxidizes water to generate a proton H^+. Gaseous oxygen O_2 is produced at the anode. The external potential (applied through the potentiostat to the cell) helps the proton to reach the surface of the cathode, where it combines with the liberated electron to form hydrogen H_2. The H_2 generation efficiency has also been investigated by the use of organic hole scavengers. Liu and co-workers [131] found that ethylene glycol enhanced the rate of hydrogen generation. A wide range of organic compounds such as carbon, sugar, alcohols, cellulose, hydrocarbons and fatty acids can be used as reducing agents. These compounds are oxidized to give hydrogen gas and at the same time, water is reduced. Various tube morphologies have been used for generating hydrogen such as multiwall nanotubes [53].

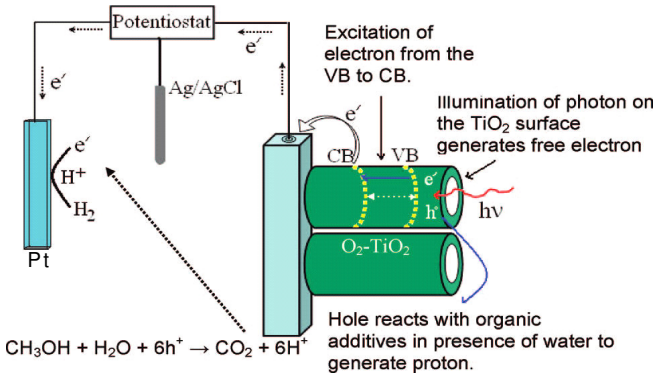

Figure 7.1 The mechanism of hydrogen generation [186].

The principle of TiO_2 nanotube photocatalysis and the experimental arrangement are shown in Figure 7.1 adapted from Morhapatra's work [186]. A three-electrode configuration is used, with a saturated Ag/AgCl reference electrode and Pt foil as a cathode. Under light illumination, holes from the valence band move towards the electrolyte and react with the organic compounds and electrons from the conduction band move towards the Ti plate and through the external circuit to the cathode.

We investigated the influence of crystallite and tube morphology on the efficiency of hydrogen generation. We compared the photocurrent from circular and polygonal nanotubes and monitored the effects of the annealing temperature on the photoelectrolysis efficiency. The second part of this chapter is focused on the enhancement of H_2 generation by use of organic hole scavengers. The efficiency is normally restricted by the oxidation at the anode as two holes are required simultaneously to oxidize a molecule of water. Upon addition of hole scavengers, holes oxidize the organic additives instead of water, and this normally requires a lower oxidation potential.

7.3 Preparation of TiO_2 Nanotubular Photoanodes for Water Splitting

Samples were prepared as described in chapter 2 section 2.2. A TiO_2 nanotube array was formed by anodisation under an applied voltage 100 V. The anodisation time was 1 hour and the distance between the electrodes was 6.0 cm. The electrolyte was 0.6 wt. % of ammonium fluoride and 2 wt. % of DI water in EG. After anodisation, the TiO_2 nanotubular array was ultrasonicated in DI water for 10 min then left to dry, and annealed at a specific temperature for a specific time. Experiments were carried out in a glass cell with a three-electrode configuration, as described previously in chapter 2 (section 2.9). The area of the anode was 1 cm^2. A potentiostat was used to control the PEC voltage and to measure the photocurrent. A solution of 100 ml of 1 M KOH was used as electrolyte.

To study the effects of organic hole-scavengers, organic compounds, such as EG, methanol and mixtures of the two were added to the electrolyte by a microsyringe. The measurement of photocurrent density was made after stirring for 3 min. In order to optimise the crystal structure, the titania arrays were annealed at 550 $^{\circ}C$, chosen because it gave the maximum photocurrent for TiO_2 nanotubes in KOH solution without organic additives**.**

7.4 Results and Discussion

We studied the effects of nanotube length, diameter and annealing temperature. Phase transitions were monitored with powder XRD, and correlated with the photocurrent. The effects of tube morphology, such as whether the nanotubes were polygonal or circular nanotubes were also studied.

7.4.1 The Effect of Tube Length on the Photocurrent Density

The length and area of the nanotube are must be optimised. An optimal length and large area is very important for the absorption of the incident photon, to prevent the recombination of photogenerated electron-hole pairs. The light absorption is generally increased when the thickness of the TiO_2 film or the length of the vertically aligned nanotubes is increased. If the nanotubes are too short, the light is not effectively absorbed. Short nanotubes have less surface area accessible to the electrolyte so the photocurrent density is restricted. With short anodisation times, the initial nanotubes are normally irregular [43] so the transportation of ions in and out of the bulk nanomaterial is restricted. For a one dimensional nanotube with length longer than needed for full light absorption the probability of the charge transportation is reduced as the photogenerated electron hole-pair can recombine. Therefore the size and shape of the tubes should be optimised to maximise light absorption, surface area and charge transportation.

In our experiments, the tube length was controlled by changing the anodisation parameters such the anodisation time [66]. As shown in Figure 7.2, the tube length increased non-linearly with the anodisation time. With 20 min anodisation, short TiO_2 nanotubes with length about 2.5 µm were formed; after 240 minutes the tube length was 25 µm.

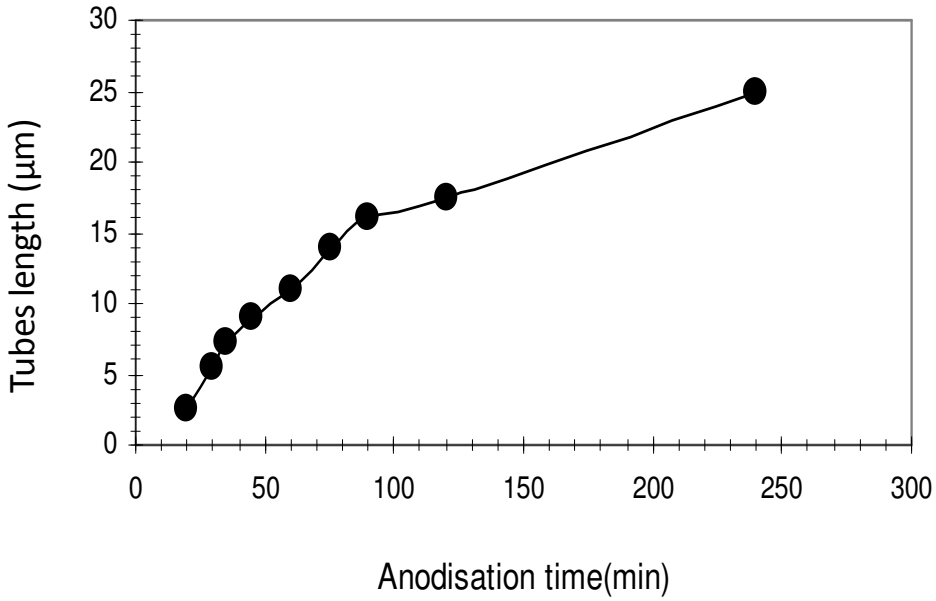

Figure 7.2 The effect of anodisation time on TiO_2 nanotube thickness.

The light blue curve in Figure 7.3a shows the photocurrent as a function of electrochemical potential relative to the saturated Ag/AgCl electrode. The TiO_2 nanotubes were 5.5 µm thick and were annealed at 500 ˚C for 30 min before they were used as photoanodes. The red curve shows the photocurrent with the xenon light source alternating on and off. The dark current is shown by the dark blue curve. It is clear that, without light, the current was almost zero for an electrochemical potential between –1.0 and +1.5 V. In contrast, with illumination, the photocurrent gradually increases and reaches maximum of 6.3 mA/cm^2.

The effect of tube length on the photocurrent density in the PEC is shown in Figure 7.3b. The length of the nanotubes was measured by SEM and the photocurrent density was measured at an electrochemical potential of 0 V relative to Ag/AgCl. As the length of the nanotubes increased, the photocurrent density gradually increased. When

the thickness was about 11 µm, obtained by 60 min anodisation, the highest photocurrent density was achieved. Longer nanotubes gave slightly smaller photocurrent density.

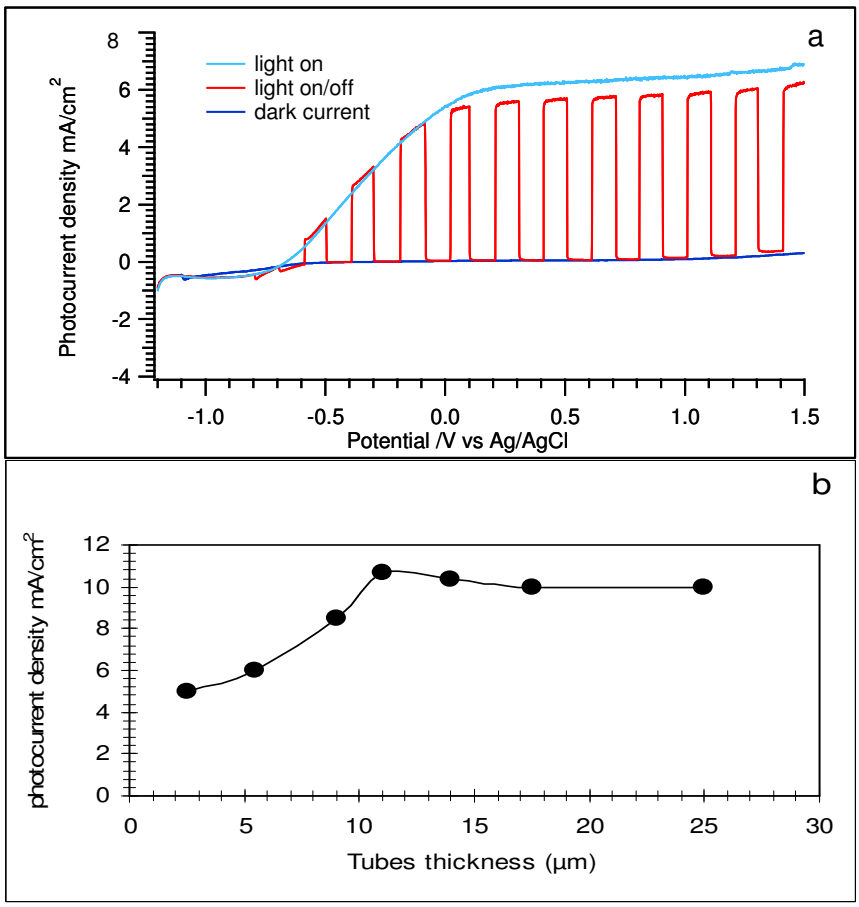

Figure 7.3 (a) The photocurrent from nanotubes 5.5 µm long anodised for 30 min and annealed at 500 °C (b) the effect of tube length on the photocurrent density of TiO_2 nanotubes annealed at 500 °C.

7.4.2 The Influence of Voltage on the Photoresponse

Both the diameter and length of the nanotubes can be tailored by control of the anodisation voltage [66, 157]. In a previous section, we have reported that a higher anodisation voltage gives longer nanotubes with larger diameter. An increase in the

nanotube diameter increases the electrolyte mobility and enhances the reaction at the liquid-solid interface. An increase of the tube length improves the light absorption.

The photocurrent density was studied for both crystallised (annealed) and amorphous (as synthesised) TiO_2 nanotube arrays. Figure 7.4 shows the photocurrent density measured at 0 V relative to Ag/AgCl as a function of anodisation voltage, with tubes having diameters from 30-160 nm. For amorphous TiO_2 nanotubes, the effect of anodisation voltage is not obvious; there is only a slow increase in photocurrent density as the voltage is increased. However, for samples annealed at 500 ˚C, the photocurrent density increases dramatically as a function of anodisation voltage. For example, with 20 V anodisation, the photocurrent density reached 1.7 mA/cm^2 and with 120 V anodisation the photocurrent density reached 10.5 mA/cm^2. This represents a six-fold increase in the power conversion. It is clear that annealing the sample to give crystalline nanotubes increases the photocurrent. This increase is directly related to the charge mobility, which can be greatly increased in crystalline samples that have fewer defects as charge traps. In the next section, we focus on the effect of annealing temperature on the efficiency of water splitting.

Increases in both tube length and tube diameter can contribute to the increase in photocurrent density, but we are not able to clearly distinguish their individual contributions experimentally. It is very difficult to control the nanotube diameter without affecting the nanotube length.

For annealed nanotubes, the photocurrent density gradually approaches a maximum value at an anodisation bias of 120 V. We expect the photocurrent density to

decrease if the anodisation voltage is increased further. This behavior may be compared with the effect of tube length on the photocurrent discussed in a previous section; it is probably the length of the nanotube which limits charge transfer to the back metallic electrode. The measured nanotube diameter increases from 80 to 120 nm when the anodisation voltage increases from 60 to 120 V. We expect therefore that in this voltage range, the tube diameter will have little effect on the photocurrent, since the effect of improved electrolyte transportation in and out of the nanotube is balanced by the reduction in surface area.

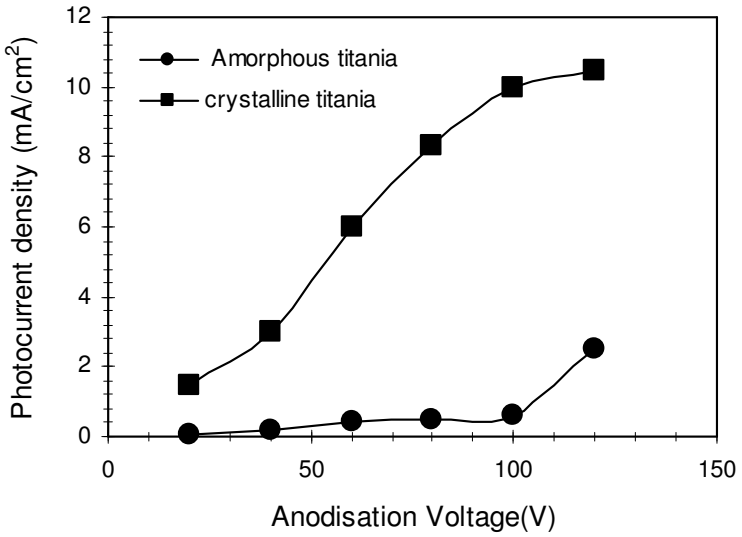

Figure 7.4 The effect of anodisation voltage on the photocurrent density from amorphous and crystalline titania nanotubes.

7.4.3 The Effect of Thermal Treatment on the Photocurrent Density

TiO_2 nanotubes are initially obtained with an amorphous structure. They can be converted into anatase at temperatures higher than 280 °C [48, 187]. However, according to Macak *et al* [143] anatase can also be directly formed during anodisation and may be converted into rutile on heating by the rearrangement of Ti-O octahedra following the breakage of two Ti-O bonds. The process is accelerated by oxygen vacancies in the anatase lattice and can be further affected by thermal treatments, addition of dopants and the method of synthesis. The transition from anatase to rutile which occurs at an annealing temperature above 700 °C, is an important factor to be considered in optimizing the response of a material in a given application. Our experimental evidence has confirmed that the photoefficiency is maximised when the dominant phase is anatase with a small amount of rutile.

In addition to the crystal phase transition, the morphology of the nanotubes changes during annealing at high temperature. Nanotubes are reported to be stable up to 580 °C in air [187]. At higher temperatures the tubular structure collapses. Regonini et al. observed rutile protrusions at temperatures of 500 °C or higher and identified these protrusions as the main cause of the collapse of the nanotubes [188].

In our work the measured photocurrent density is shown in Figure 7.5a with light alternately on and off. For electrochemical potentials between −1.0 and +1.2 V, the dark current is almost zero. However, with the light on, the photocurrent gradually increases as the electrode potential increases from −0.5 V to +1.2 V. It is clear that the maximum photocurrent density from the polygonal nanotubes (20.0 mA/cm^2, green curve) is much higher than that from circular nanotubes (15.3 mA/cm^2, red curve).

The typical morphologies of polygonal and circular nanotubes are shown in the insert in Figure 7.5b. Details have been discussed in chapter 4 section 4.4.1. After annealing at 550 ˚C in air, the photocurrent density was measured in a glass PEC with 1M KOH as electrolyte and illumination from a 300 W xenon lamp. A comprehensive study of the effect of annealing temperature is shown in Figure 7.5b from 22 ˚C to 750 ˚C.

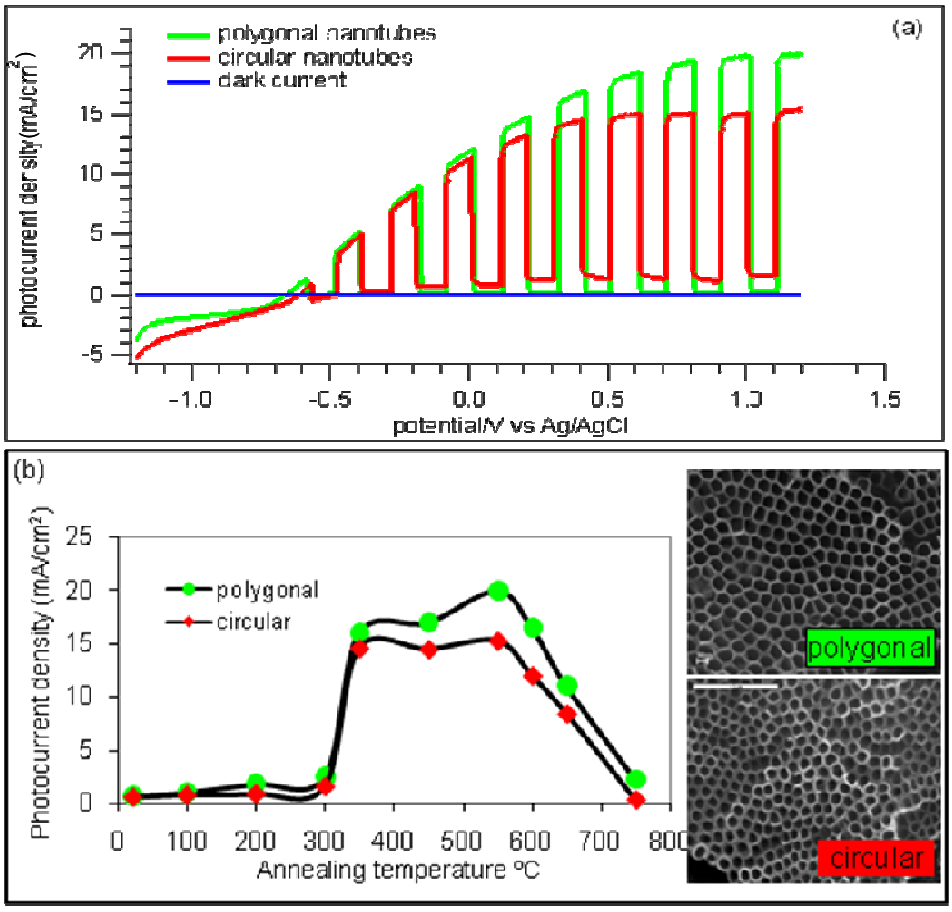

Figure 7.5 (a) The voltammograms of polygonal and circular TiO_2 nanotubes annealed at 550 ˚C under illumination (light on) and without illumination (light off). (b) Photocurrent density of polygonal and circular nanotubes annealed at various temperatures from 22-750 ˚C.

For both circular and polygonal nanotubes, the photocurrent densities are low when the samples are annealed below 300 ˚C. For samples annealed above this temperature, the photocurrent density increases and reaches a maximum for samples annealed at 550 ˚C. For samples annealed at high temperature the photocurrent density decreases almost linearly as a function of temperature.

It is also clear, that whatever the annealing temperature, the photocurrent density is higher from polygonal than from circular nanotubes. The maximum difference in photocurrent was observed at 550 ˚C when the photocurrent density was maximum. We believe this is related to our assumption that for polygonal nanotubes, crystals form most readily along the line where the flat tube walls intersect.

A similar temperature-dependent photocurrent density manner has been observed. Hardcastle and co-workers [189] found a decrease of photocurrent density when a TiO_2 anode was annealed between 500 ˚C and 600 ˚C and they that suggested this was due to the phase transition from anatase to rutile. Similar results were found for WO_3 semiconductor photoanodes [190]. In the next section, we describe the use of XRD to investigate the phase transition and to correlate it with the photoresponse described here.

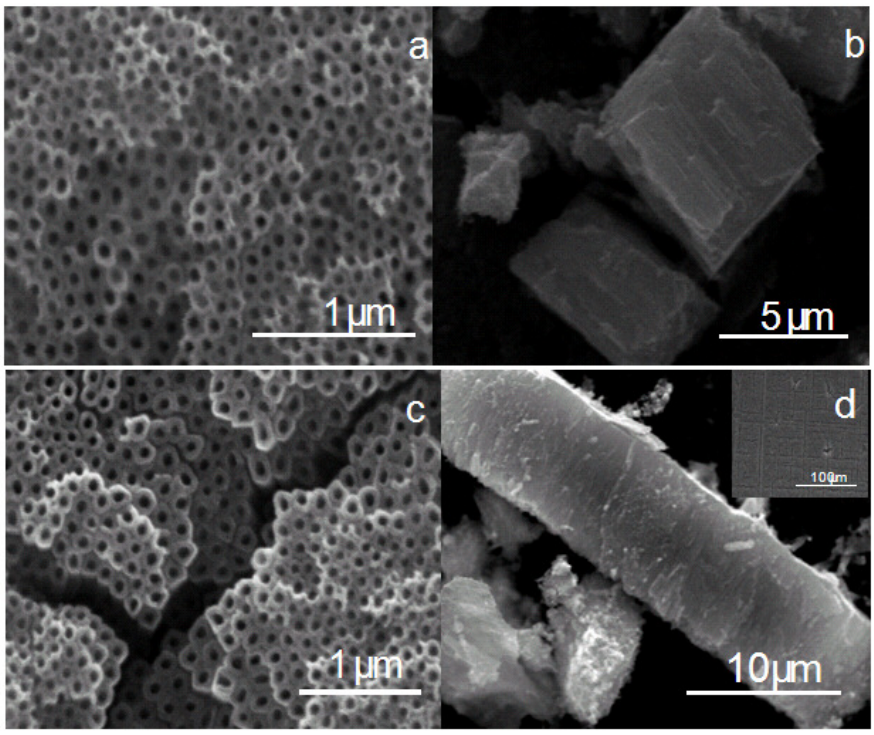

Figure 7.6 SEM images of TiO_2 nanotubes annealed at 550 °C for circular nanotubes (a) top-view, (b) side view and polygonal nanotubes (c) top-view and (d) side view.

The morphology of both polygonal and circular tubes was affected by the annealing process. The tube dimensions such as diameter and length are slightly different before and after annealing. After annealing a reduction in porosity and surface area occurs due to the nucleation of crystalline structure [191, 192], Figures 7.6 shows the morphology of both circular (Figure 7.6a and b) and polygonal (Figure 7.6c and d) nanotubes after annealing at 550 °C. Although the tubular structures are maintained, the ID of the nanotubes is reduced by 10% on average during annealing. The lengths of the annealed nanotubes are measured from the SEM images shown in Figure 7.6 b and d. The length of the nanotubes was reduced to 8 µm (the original lengths for polygonal and circular tubes were 11 and 10 µm, respectively) and the overall surface area was reduced, during annealing.

The morphological transition at higher temperature is shown in Figure 7.7 with the top view of the circular nanotubes annealed at 600 ˚C (Figure 7.7a) and 650 ˚C (Figure 7.7b).

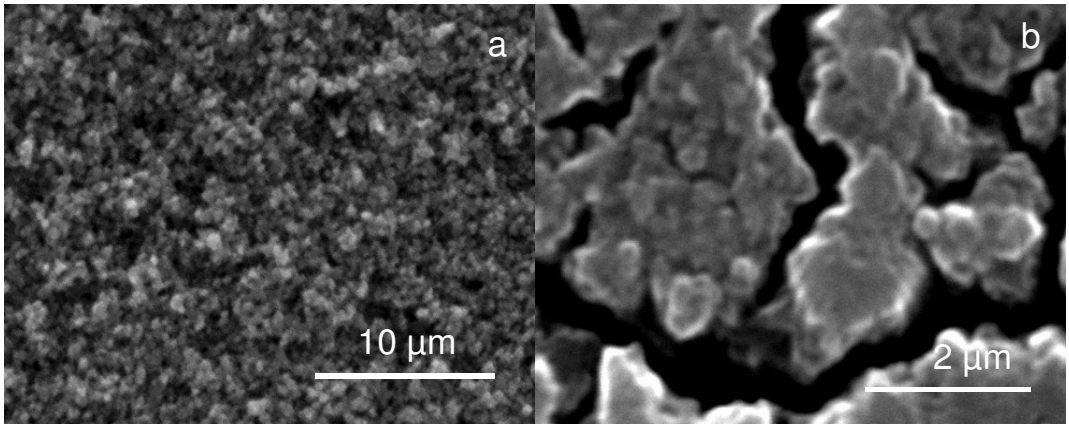

Figure 7.7 SEM images of TiO_2 nanotube arrays annealed at (a) 600 ˚C and (b) 650 ˚C showing (a) collapse and (b) cracking after sintering.

The images show that the original structure of the nanotubes collapses at 600 ˚C and that there is serious cracking at 650 ˚C. The collapse and sintering of the nanotube structures gives a significant reduction in effective surface area and reduced contact between the TiO_2 and electrolyte. Thus the photocurrent density is also reduced.

7.4.4 The Effect of Thermal Treatment on the Crystal phase Transition

Powder XRD measurements have been made on polygonal and circular TiO_2 nanotube arrays in order to study the phase transition as a function of annealing temperature. The annealing temperatures varied from 22 ˚C to 750 ˚C.

A typical powder XRD pattern of a sample annealed at 650 ˚C is shown in Figure 7.8. The diffraction data show three phases: anatase, rutile and Ti metal. In general,

samples annealed at low temperature show only the presence of anatase with the 101 peak at 2θ = 25.3º. As the annealing temperature increases the signal at 2θ = 27.5º, corresponding to rutile, appears.

All anatase and rutile peaks were calibrated by standard patterns [129]. The tables of peaks are shown in Chapter 2 (section 2.8). In Figure 7.8, the Miller indices of the peaks are labelled and the anatase and rutile phases are indicated by A and R. As the thin TiO_2 nanotube layers were grown on Ti plates, the diffraction peaks from the Ti substrate can also be observed.

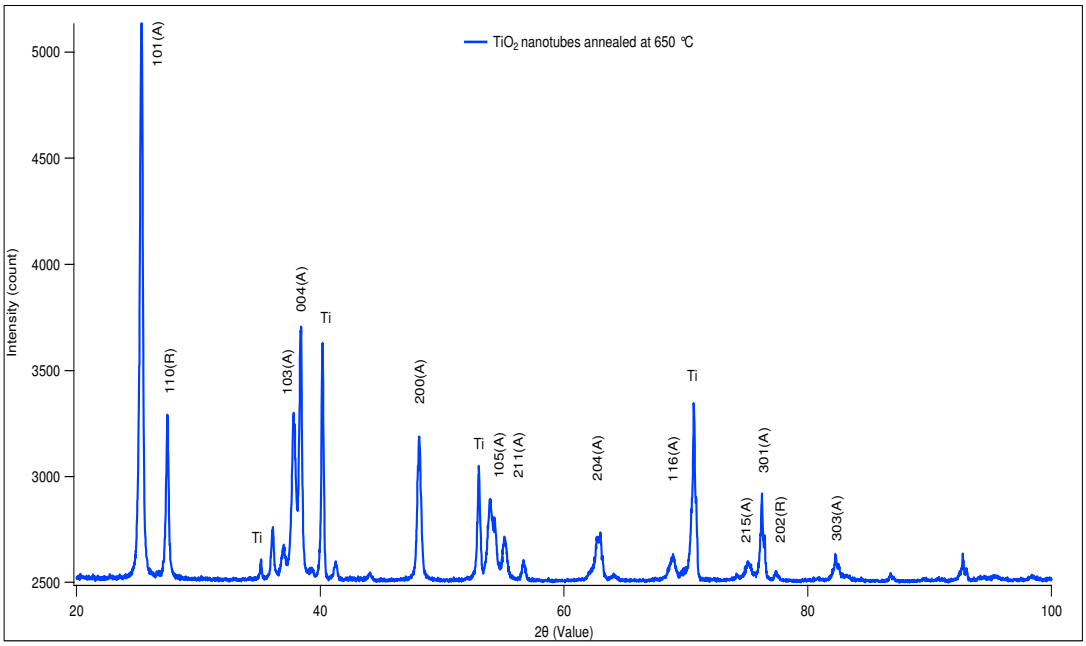

Figure 7.8 A typical XRD pattern of a TiO_2 nanotube thin film showing anatase (A) and rutile (R) on titanium (Ti).

Here, we correlate the photocurrent density measurements reported in last section with the XRD results. Thin films are usually, prepared on a substrate. In X-ray diffraction patterns the peaks from the substrate can sometimes overshadow those from the thin film. The contribution of the substrate can be minimized by reducing the angle of incidence of the X-ray beam. This technique is called glancing angle X-ray diffraction (GAXRD). In order to compare polygonal and circular films we used GAXRD analysis with an angle of incidence 4º on samples obtained by thermal treatment in air at 100, 200, 300, 400 and 500 ˚C. The results are shown in Figure 7.9 (a-e).

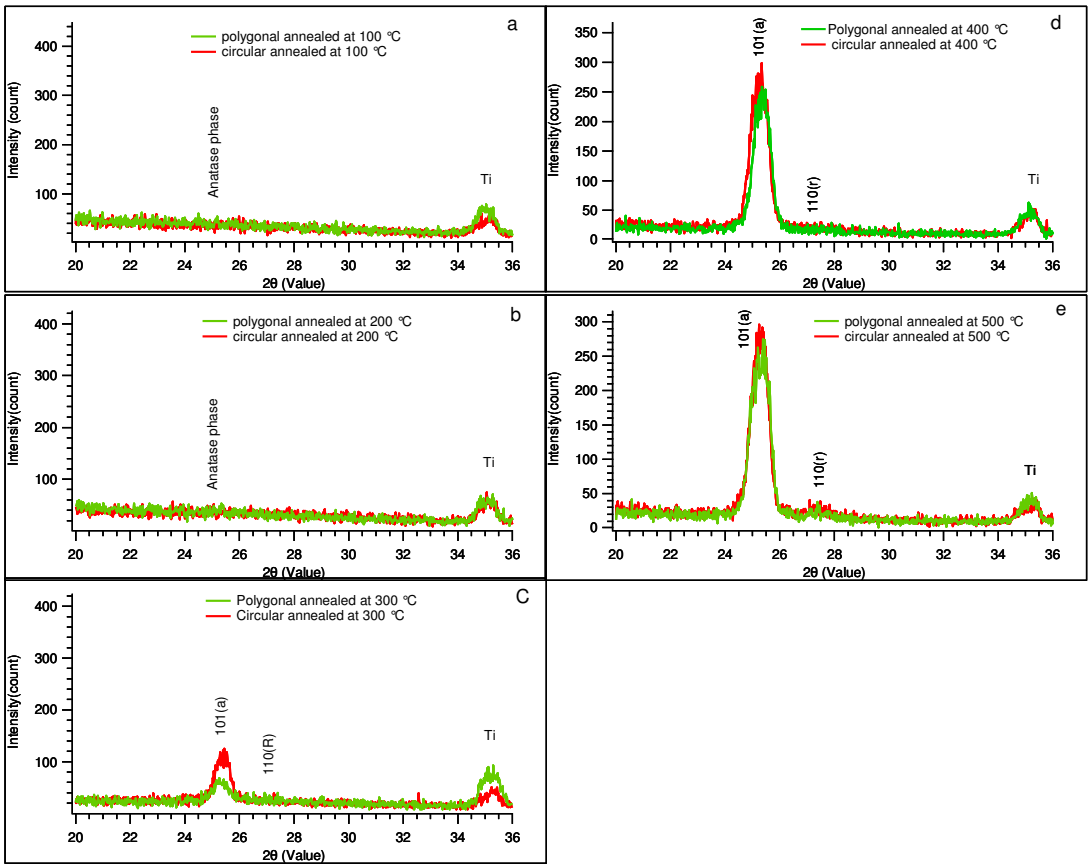

Figure 7.9 4º GAXRD patterns for polygonal (green curve) and circular (red curve) nanotubular arrays annealed at various temperatures (a) 100 ºC, (b) 200 ºC, (c) 300 ºC, (d) 400 ºC and (e) 500 ºC, for 2 hours.

When the sample is annealed below 300 ˚C, there is no obvious crystallisation. However, the anatase structure starts to form at 300 ˚C, the temperature, at which the photocurrent densities start to increase. The XRD patterns of polygonal and circular TiO_2 nanotubes confirmed the presence of anatase. At this stage, there is no significant difference in the crystallinity between the polygonal and circular nanotubes.

Further annealing at higher temperatures improves the crystal structure dramatically. Figure 7.10 shows the XRD data from polygonal and circular nanotubes annealed at 550 ˚C. At this stage, the dominant phase is anatase with small contribution of rutile. A significant increase in the photocurrent density was observed for samples annealed at this temperature, without significant change of the tubular morphology. Therefore, we can conclude that the improvement of the crystallinity is essential for the improvement of the photoefficiency. Annealing in ambient oxygen is found to be an important post-treatment process to transform titania nanotubes from amorphous to crystalline. A high annealing temperature produces better crystallinity as shown by XRD traces.

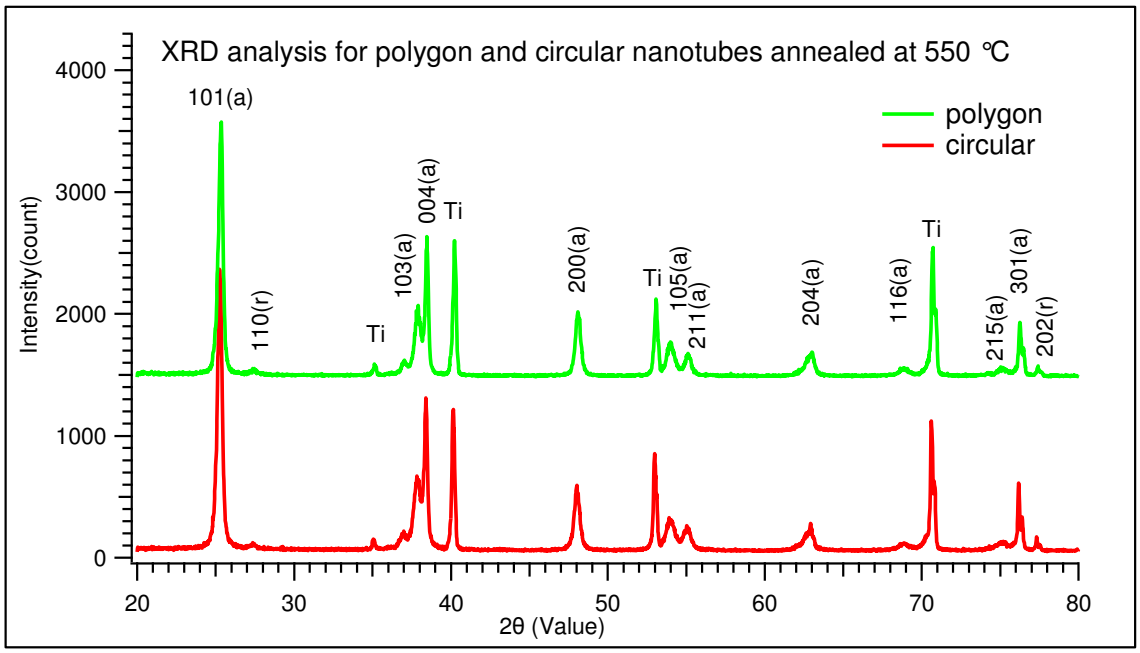

Figure 7.10 Typical XRD traces of polygonal and circular TiO_2 nanotubes annealed at 550 ˚C.

Further annealing at higher temperature decreases the photo efficiency, although the diffraction data shown in Figure 7.11 show a further improvement of the crystal quality. Polygonal TiO_2 nanotubes show increased amounts of rutile. For the nanotubes annealed at 650 ˚C, the intensity of the rutile 110 (r) peak from polygonal nanotubes (859 counts) is almost the double that from circular nanotubes (424 counts). The intensity of the Ti substrate remains constant, which suggests no significant reduction of film thickness.

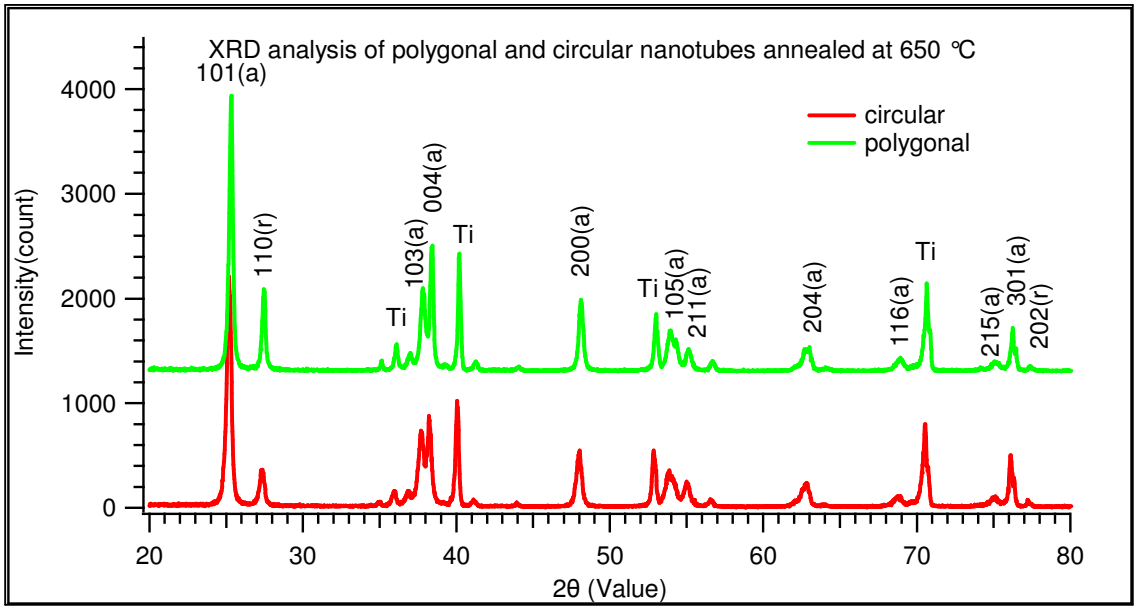

Figure 7.11 Typical XRD traces for TiO_2 polygonal and circular nanotubes annealed at 650 ˚C.

The increase in the proportion of rutile becomes more obvious for a sample annealed at 750 ˚C, as shown in Figure 7.12. The most intense rutile peak from (110) plane has a high intensity for both polygonal and circular nanotubes. However, its intensity increases more significantly for the polygonal nanotubes.

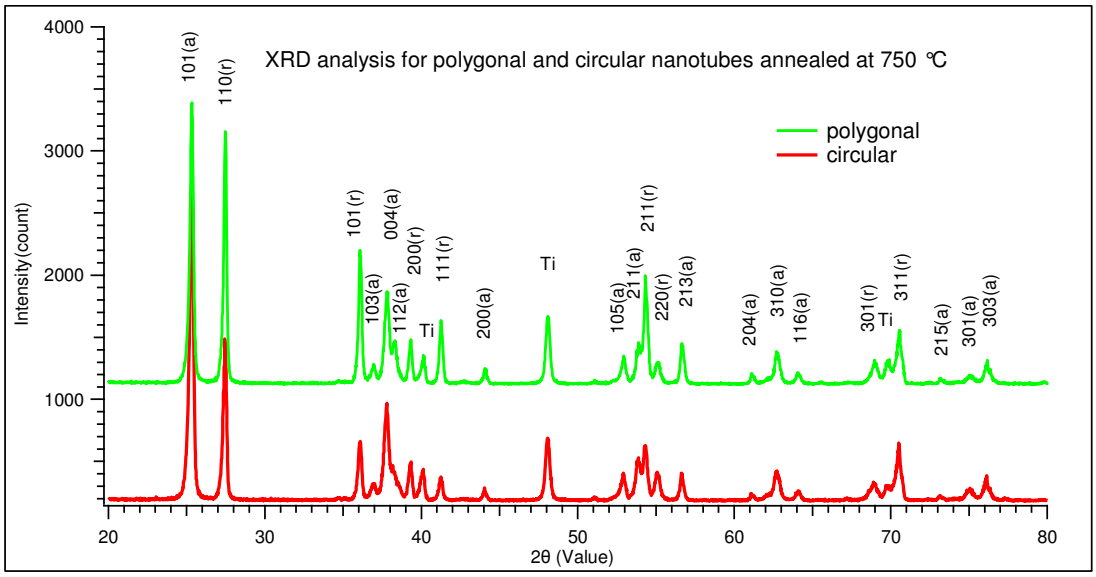

Figure 7.12 Typical XRD patterns for TiO_2 polygonal and circular nanotubes annealed at 750 ˚C.

The increase in the photocurrent density for TiO_2 nanotubes is strongly related to their crystal structure. Annealing at a temperature above 300 ˚C is essential for the formation of anatase which results in an increase in photocurrent density as the charge mobility increases. For samples annealed at higher temperatures, the crystallinity is improved for both polygonal and circular nanotubes but the photocurrent density decreases. We consider that the collapse of the tubular morphology with a reduction in surface area is the key factor in the loss of photoefficiency.

7.4.5 The Effect of Annealing Time on the Photocurrent Density

A phase transition during annealing is normally kinetically controlled. So the annealing time affects the crystallinity and the photocurrent density. TiO_2 films were

annealed at 300 ˚C and 500 ˚C for various durations (2-7 h) in a tube furnace in air. The photocurrent density was measured after annealing.

Figure 7.13a shows the enhancement in the photocurrent density of TiO_2 nanotubes (measured at 0 V *vs*. Ag/AgCl) with increased annealing time and Figure 7.13b shows examples for various annealing times. The photocurrent density gradually increases from 0.85 mA/cm^2 for a sample annealed for 2 h to 3.4 mA/cm^2 for a sample annealed for 7 h, corresponding to a factor of 4 improvements. The XRD study showed that anatase is formed at 300 ˚C. But as anatase formation might be restricted by the crystallinity kinetics an increase in annealing time could improve the crystallinity and the photoefficiency. Annealing times longer than 7 h gave no improvement in photocurrent density.

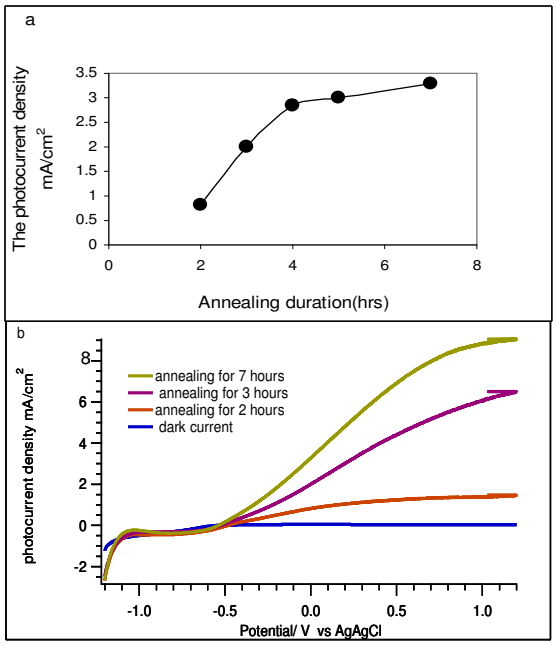

Figure 7.13 (a) The influence of annealing duration on the photocurrent density of TiO_2 nanotubes annealed in air at 300 ˚C, (b) voltammetric measurements, for TiO_2 nanotubes annealed for different times.

For samples annealed at 500 ˚C, the photocurrent density also increases with increased annealing duration as shown in Figure 7.14a. However, the leveling off of the photocurrent density was achieved in a shorter time (3 hours) than for samples annealed at 300 ˚C. This observation suggests that 1) the formation of crystallites is responsible for the improvement of the photocurrent density; 2) the crystallisation rate is higher at 500 ˚C than at 300 ˚C. These conclusions are confirmed by the XRD patterns shown in, Figure 7.14b for TiO_2 nanotubes annealed at 550 ˚C for 2 and 4 h. The anatase peak at 25.3º is clearly higher in the sample annealed for 4 hours.

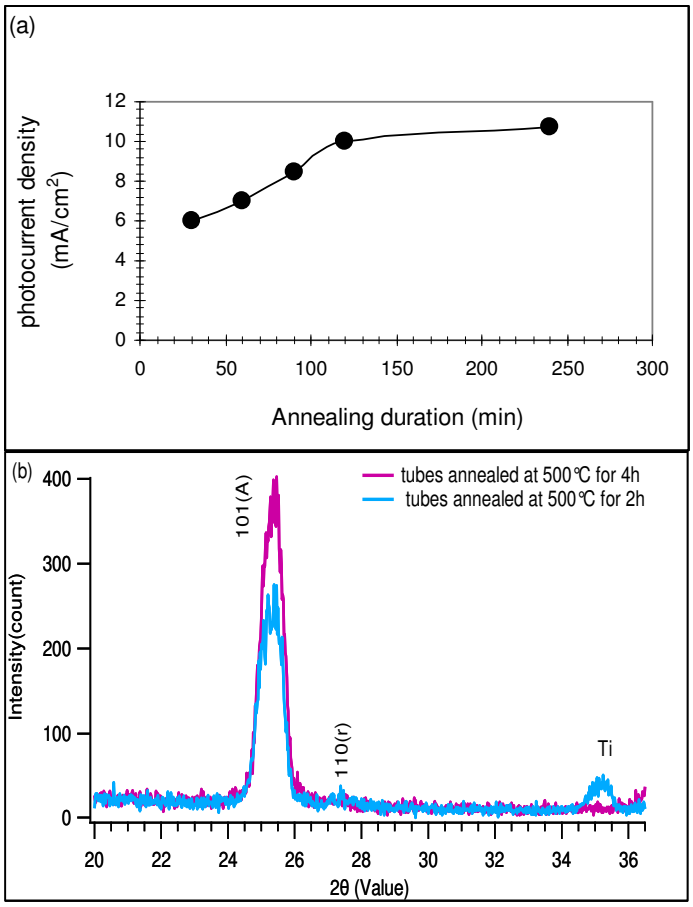

Figure 7.14 (a) The influence of annealing duration on the photocurrent density of TiO_2 nanotubes annealed in air at 500 ˚C, (b) XRD patterns for TiO_2 nanotubes annealed at 500 ˚C for different annealing times.

7.4.6 Addition of Organic Compounds

Organic compounds can be used as hole scavengers to improve the photoefficiency. The presence of organic compounds in the electrolyte suppresses generation of oxygen gas at the photoanode; instead organic compounds are oxidized. A significant increase in the photocurrent following the addition of organic compounds, suggests that the oxidation of H_2O at the anode is the rate limiting process in their absence.

In our experiments we used methanol and ethylene glycol as organic additives as they contain hydroxide groups which facilitate adsorption on to metal oxide surfaces. The addition of 0.05 to 5 ml vol % of methanol or EG to 100 ml 1M KOH leads to a gradual increase in the photocurrent density for both polygonal and circular nanotubes as shown in Figure 7.15. However, the increase in photocurrent density is much higher for polygonal nanotubes than for circular nanotubes. For a photoanode with polygonal nanotubes, the photocurrent was increased from 13 mA/cm^2 to 20.5 mA/cm^2 or 18.5 mA/cm^2 when, respectively, 1.6 ml methanol or 1.6 ml EG was added. For circular nanotubes the photocurrent was increased from 11 mA/cm^2 to 17.5 mA/cm^2 or 16.0 mA/cm^2 when 1.6 ml of methanol or EG was added. Addition of methanol or EG improved the photocurrent density by at least 50%.

The addition of more organic compound does not necessarily increase the photocurrent further. At this stage, the photoefficiency is limited by other factors, such as photon absorption, charge mobility and reduction of H_2O. For polygonal and circular nanotubes, the addition of methanol and EG has similar effects, although the initial

photocurrent density is higher for polygonal nanotubes. However, it seems that methanol is a better choice than EG as hole scavenger in this application.

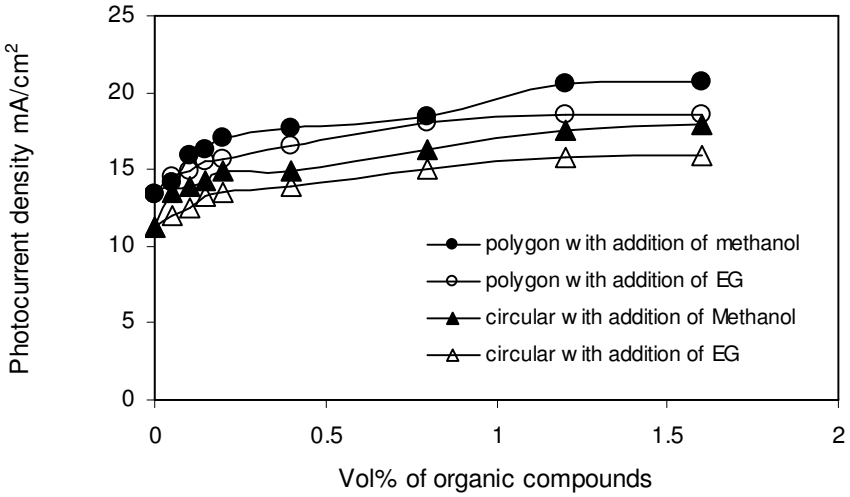

Figure 7.15 The effect of the addition of organic compounds on the photocurrent density using polygonal and circular nanotubes as photoanodes.

The effect of various organic additives on the reduction of electron-hole recombination losses depends on their redox potential and reactivity in a particular solution [186]. The chemical potential of the electrons in a solution is determined by redox potentials of all substance present, including the redox potential of the solvent itself.

The splitting of water with the addition of methanol and EG as organic additives can be described as follows:

$$CH_3OH + H_2O + 6h^+ \rightarrow CO_{2(gas)} + 6H^+_{(aq)} \quad \text{Equation 7.1}$$

$$6H^+ + 6e^- \rightarrow 3H_{2(gas)} \quad \text{Equation 7.2}$$

$$HOCH_2CH_2OH + 2H_2O + 10h \rightarrow 10H^+ + 2CO_2 \quad \text{Equation 7.3}$$

$$10H^+ + 10e^- \rightarrow 5H_2 \quad \text{Equation 7.4}$$

Hence, 1 mol of methanol generates 3 mol of hydrogen and 1 mol of EG generates 5 mol of hydrogen.

Better enhancements of photocurrent were achieved for polygonal nanotubes than for circular nanotubes and slightly better enhancements for methanol than for EG. The reason photocurrent enhancement with methanol is greater might be related to the diffusion rates of the organic compounds into the nanotubes, which is determined by the diameter of nanotubes and the size of molecules of organic compounds.

7.4.7 Addition of the Mixture of EG and Methanol

As we have demonstrated that addition of methanol or EG improves the photocurrent density to 20.5 and 17 mA/cm^2 for polygonal and circular nanotubes respectively, we decided to examine the possibility of obtaining a further increase in the photocurrent density by use of mixtures of methanol and EG. Mixtures with the volume ratios, of 1:1 and 2:1 of EG and methanol were added to 100 ml of 1M KOH electrolyte. The experimental results show only slight enhancement of photocurrent density by addition of methanol-EG mixtures.

Figure 7.16 shows the gradual increase in the photocurrent density of polygonal and circular TiO_2 nanotubes by increasing volumes of 1:1 mixtures of EG and

methanol. The current densities were sampled at an electrochemical potential of 0 V *vs* Ag/AgCl. The maximum photocurrent density was achieved by the addition of 0.65 ml of a 1:1 mixture of methanol and EG (0.325 ml of methanol plus 0.325 ml of EG), which is much lower than the volume of methanol or EG alone (1.6 ml) to achieve the same effect. The achieved photocurrent density was 21.0 mA/cm^2 and 17.5 mA/cm^2 for polygonal and circular nanotubes respectively. Thus, for polygonal nanotubes, the addition of a mixture of organic compounds increases the photocurrent density slightly, while for circular nanotubes, there is almost no increase of the photocurrent density.

Typical voltammetric measurements with light on and off, for polygonal and circular nanotubes, are shown in Figure 7.16b. In this experiment, the total volume of added organic compounds was 0.8 ml (0.4 ml of methanol + 0.4 ml of EG). The maximum photocurrent densities were achieved at a potential of + 0.8 V with a value of 29 mA/cm^2 for the polygonal nanotubes. However for circular nanotubes, the maximum photocurrent density was achieved at a potential of + 0.2 V with a value of 17 mA/cm^2.

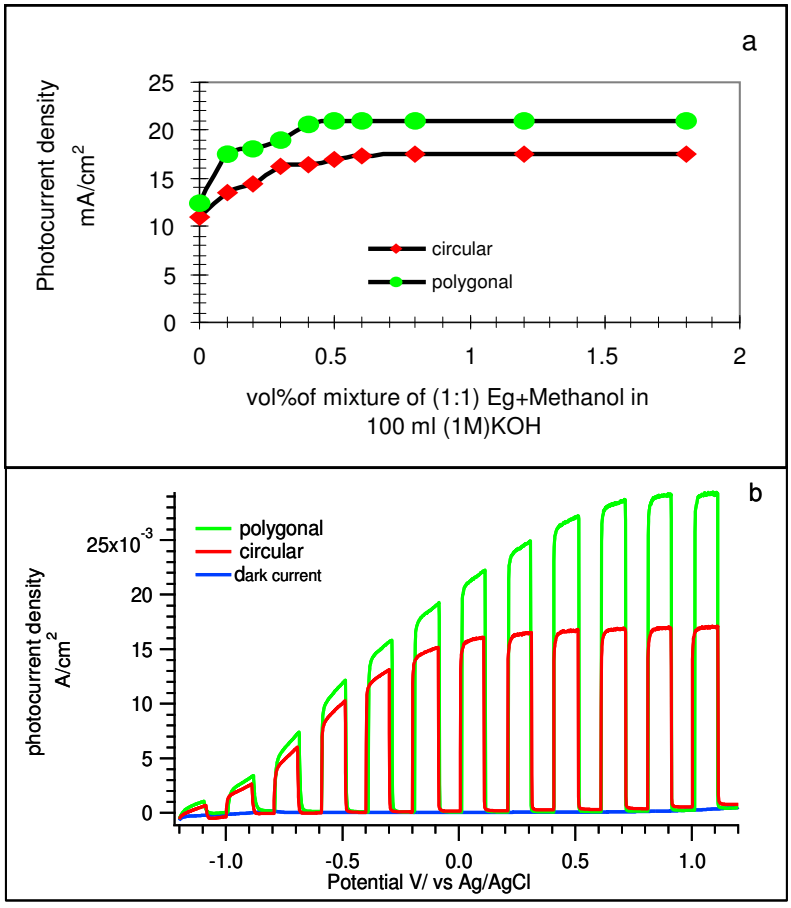

Figure 7.16 (a) Photocurrent density for a TiO_2 photoanode in 1 M KOH containing various amounts of 1:1 mixtures of EG and methanol, (b) Voltammetric measurements of polygonal and circular tubes in 1 M KOH with the addition of a mixture of 0.4 ml of methanol and 0.4 ml of EG.

The addition of various volumes of organic compounds was also investigated. Figure 7.17a shows the increase in the photocurrent density (measured at 0 V *vs* Ag/AgCl) when the volume % of a 2:1 EG/methanol mixture was increased. The maximum photocurrent densities of 23.0 mA/cm^2 and 17.5 mA/cm^2 at 0 V potential were achieved for polygonal and circular photoanode arrays respectively. Figure 7.17b shows the voltammetric measurement for polygonal nanotubes used as photoanodes in a PEC with addition of a 2:1 methanol/EG mixture (0.4 ml EG + 0.2 ml methanol).

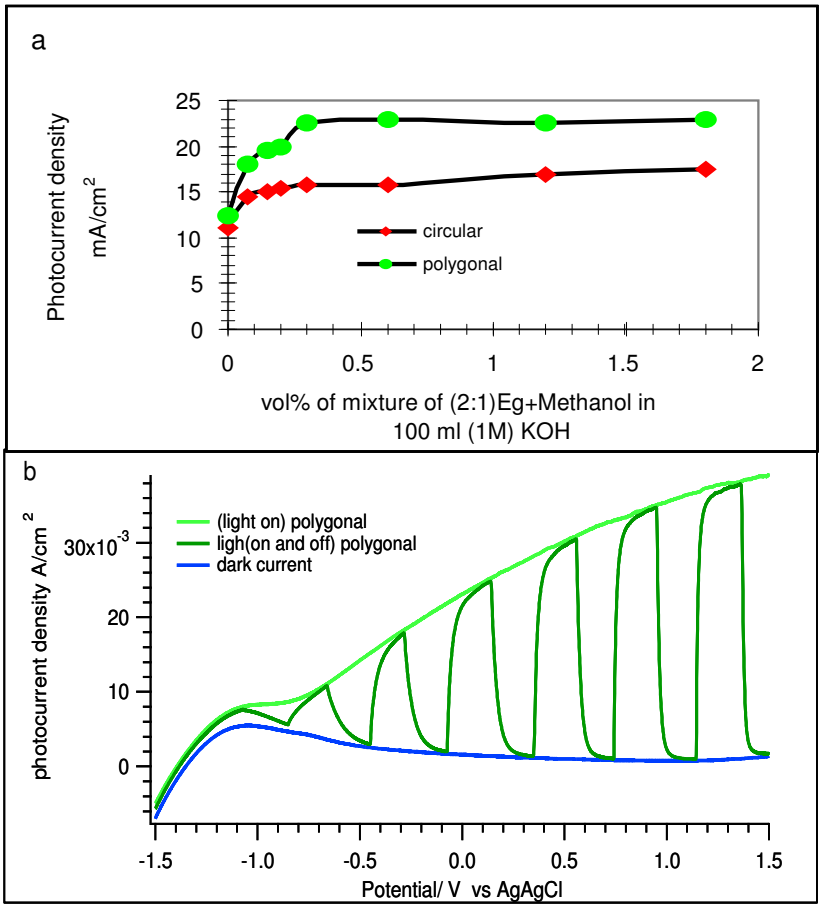

Figure 7.17 (a) Photocurrent density for TiO_2 photoanode in 1 M KOH containing various volumes of a 2:1 mixture of EG and methanol. (b) Voltammetric measurements of polygonal and circular tubes in 1 M KOH with addition 0.4 ml of EG + 0.2 ml of methanol.

The addition of a 1:1 EG/methanol mixture has a small effect on the photocurrent density for the circular nanotubes, and gives small increase in photocurrent density from 20.5 to 21.0 mA/cm^2 for polygonal nanotubes. With a 2:1 ratio EG: methanol mixture, the photocurrent density increases further from 21 to 23 mA/cm^2. Thus the enhancement of photocurrent density by the organic scavenger appears to be related to the nanotube morphology. The polygonal and circular nanotubes differ in three aspects. First, the polygonal nanotube has a flat wall shared with neighbouring nanotubes, while the

circular nanotube has a curved wall. Secondly, the circular nanotube array has two types of accessible channels for the organic electrolyte. One is the channel inside the tube; the other is the void between neighbouring nanotubes. Thirdly, due to the absence of voids between nanotubes, the ID of polygonal nanotubes is normally larger than that of circular nanotubes by 10%. Using organic scavengers, the molecules are oxidized on the surface of the nanotubes and the efficiency could be affected by the diffusion and adsorption of the molecules. The effective enhancement of photocurrent density from polygonal nanotubes with both methanol and EG, or mixtures of these compounds is directly related to the large ID of the nanotubes. For circular nanotubes, methanol, the smaller molecule, is more effective than EG. A mixture of methanol and EG does not improve the efficiency, compared with methanol alone.

7.5 The Photoconversion Efficiency of TiO_2 Nanotubes

The efficiency of photoenergy conversion through the photoelectrochemical process is defined by the ratio of the electrochemical energy to the input photoenergy it can be calculated by the following equation [193].

$$\eta(\%) = [J_p(E^{\circ}_{rev} - E_{app})/I_{light}] \times 100 \quad \textbf{Equation 7.5}$$

where η is the photoconversion efficiency, J_p is the photocurrent density (mA/cm^2), I_{light} is the incident light irradiance, E_{rev} is the standard reversible potential for water splitting which is 1.23 *vs* standard hydrogen electrode V_{RHE}, and E_{app} is the applied potential which is $E_{app} = (E_{meas} - E_{oc})$, where E_{meas} is the electrode potential (*vs*. Ag/AgCl) of the working electrode and E_{oc} is the electrode potential (*vs*. Ag/AgCl) of the same working electrode under open circuit and under illumination. The

photoelectrochemical power is defined by the product of the effective voltage and the corresponding current density. The true energy conversion power is defined as the energy stored in the form of hydrogen, related to the free energy of the hydrogen combustion. From equation 7.5, the output power and photoconversion efficiency become zero under open and short circuit conditions. At open circuit, the effective potential becomes maximum of 1.23 V, but the current density, J_p, is 0 mA/cm^2. At short circuit, the effective potential becomes zero when a maximum photo current is achieved.

In our experiment, a focused 300 W xenon lamp was used as the light source. This gives a UV power (200 nm-400 nm) of 50 mW, measured with a laser power meter. As TiO_2 has a band gap of 3.2 eV, only the UV part of the light was utilised. The measurements were taken with and without the addition of organic compounds.

7.5.1 The Photoconversion Efficiency without Addition of Organic Compounds

Figure 7.18a shows the photocurrent densities of polygonal and circular nanotubes annealed at 550 ˚C with 1M KOH solution without the addition of organic compounds, as electrolyte. The measured photocurrent densities at 0 V *vs* Ag/AgCl are 12.5 and 11.0 mA/cm^2 and the open circuit voltages are – 0.69 and – 0.59 V for polygonal and circular nanotubes respectively. The short circuit potential can be calculated as (1.23 + E_{oc}) with values of 0.54 (polygonal nanotubes) and 0.64 V (circular nanotubes). The output photocurrents from polygonal nanotubes are always higher than the circular nanotubes.

The calculated photoelectrochemical power and the corresponding energy conversion efficiencies are shown in Figure 7.18b. The maximum power, as well as maximum efficiency were achieved at electrochemical potentials of –1.5 and +0.5 V *vs* Ag/AgCl for polygonal and circular nanotubes, respectively.

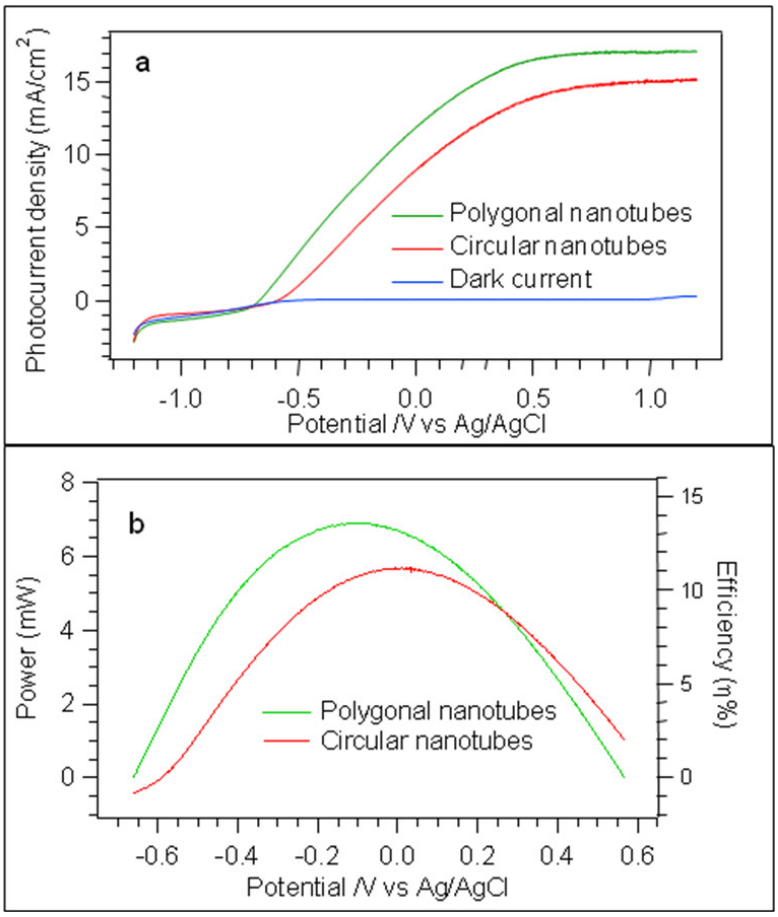

Figure 7.18 (a) Photocurrent density of polygonal and circular nanotubes in 1 M KOH without addition of organic compounds and (b) the corresponding power and photoconversion efficiency of polygonal and circular TiO_2 nanotube arrays annealed at 550 ˚C with a power input of 50 mW.

The polygonal nanotube photoanode achieves higher output power with a maximum UV efficiency of 13.5%, and the circular nanotube photoanode achieves a maximum efficiency of 10.8 %. The output power and conversion efficiency are all zero at open and short circuit voltages. The higher efficiency for polygonal nanotubes is related to its higher photocurrent density. The higher performance in photoenergy conversion with polygonal nanotube electrodes is possibly related to their higher crystallinity and to the shared tube wall structure. Such structural features could

improve the charge mobility within the TiO_2 allowing photogenerated electrons to be harvested and transferred to the cathode through the external circuit.

7.5.2 The Photoconversion Efficiency with Addition of Organic Compounds

With addition of organic compounds, the photocurrent density and photoconversion efficiency were studied as shown in Figure 7.19a and b. Equal volumes of 0.1 ml of EG and methanol were added to the 1M KOH electrolyte. The maximum photocurrent density increased from 17 to 30 mA/cm^2 for polygonal nanotubes. For circular nanotubes, the maximum photocurrent density increased from 14.5 to 16 mA/cm^2. Using equation 7.5, the calculated output power and photoconversion efficiencies are plotted in Figure 7.19b. The maximum output powers are 6.6 and 5.4 mW (at a potential of –0.5 V *vs* Ag/AgCl), which gives maximum efficiencies of 13.2 and 10.8% for polygonal and circular nanotubes. Such efficiencies are actually less than or similar to those without addition of organic compounds, although the maximum photocurrent was increased significantly for polygonal nanotubes. For both polygonal and circular nanotubes, the open circuit potentials were shifted from - 1.2 V to - 0.6 V by addition of organic compounds as were the potential for maximum output power and the photoconversion efficiency.

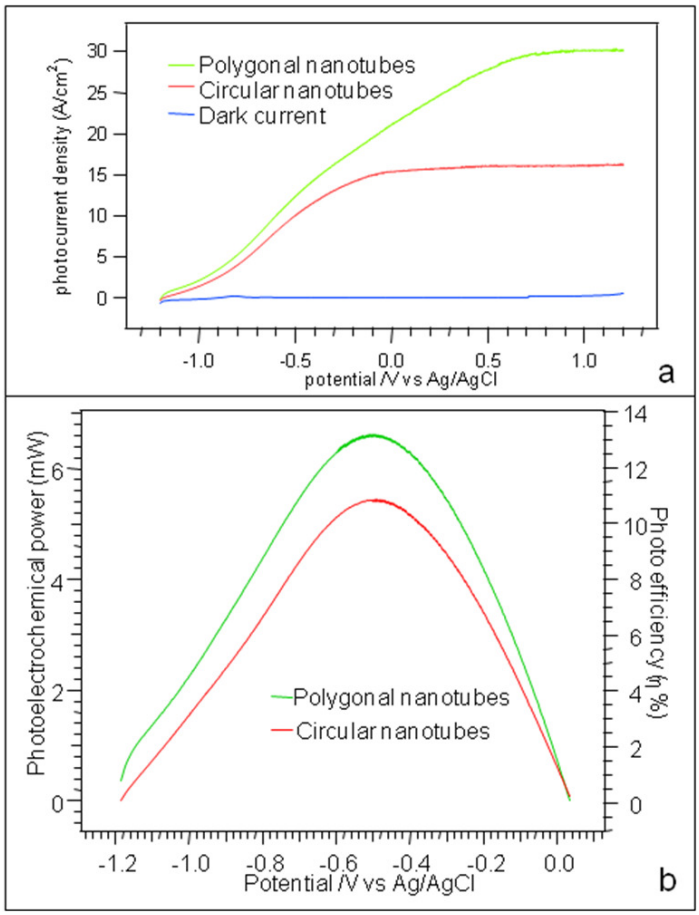

Figure 7.19 (a) Photocurrent density of polygonal and circular nanotubes in 1 M KOH with addition of a 1:1 mixture of EG and methanol and (b) the corresponding power and photoconversion efficiency of polygonal and circular TiO_2 nanotube arrays for the same mixture.

7.6 Conclusion

In this chapter, the application of polygonal and circular TiO_2 nanotubes in water splitting was investigated. We studied the influence of the crystal structure and sample morphologies on the efficiency of the process. Improvements in the crystallinity of the nanotubes significantly increased the photocurrent. Under most conditions, polygonal

nanotubes performed better than circular nanotubes as photoanodes. The formation of anatase and rutile phases within the walls of the TiO_2 nanotubes was identified by powder XRD.

Although the addition of organic hole scavengers does not improve the photoconversion efficiency, the maximum photocurrent does increase from that measured without organics. This increase in photocurrent is more obvious for polygonal nanotubes than for circular nanotubes. This might be due to the larger inner diameter of polygonal nanotubes giving better molecular transport.

References

1. Macak, J.M., et al., *TiO_2 nanotubes: Self-organized electrochemical formation, properties and applications.* Current Opinion in Solid State and Materials Science, 2007. 11(1-2): p. 3-18.
2. Ghicov, A. and P. Schmuki, *Self-ordering electrochemistry: a review on growth and functionality of $TiO_{(2)}$ nanotubes and other self-aligned $MO_{(x)}$ structures.* Chemical Communications, 2009(20): p. 2791-2808.
3. Liu, Y., et al., *Photoelectrocatalytic degradation of tetracycline by highly effective TiO_2 nanopore arrays electrode.* Journal of Hazardous Materials, 2009. 171(1-3): p. 678-683.
4. Carp, O., C.L. Huisman, and A. Reller, *Photoinduced reactivity of titanium dioxide.* Progress in Solid State Chemistry, 2004. 32(1-2): p. 33-177.
5. Landmann, M., E. Rauls, and W.G. Schmidt, *The electronic structure and optical response of rutile, anatase and brookite TiO_2.* Journal of Physics: Condensed Matter, 2012. 24(19): p. 195503.
6. Mo, S.-D. and W.Y. Ching, *Electronic and optical properties of three phases of titanium dioxide: Rutile, anatase, and brookite.* Physical Review B, 1995. 51(19): p. 13023-13032.
7. Li, G.H., et al., *Synthesizing mixed-phase TiO_2 nanocomposites using a hydrothermal method for photo-oxidation and photoreduction applications.* Journal of Catalysis, 2008. 253(1): p. 105-110.
8. Sahel, K., et al., *Photocatalytic decolorization of Remazol Black 5 (RB5) and Procion Red MX-5B - Isotherm of adsorption, kinetic of decolorization and mineralization.* Applied Catalysis B-Environmental, 2007. 77(1-2): p. 100-109.
9. Chen, X. and S.S. Mao, *Titanium dioxide nanomaterials: Synthesis, properties, modifications, and applications.* Chemical Reviews, 2007. 107(7): p. 2891-2959.
10. Song, M.Y., et al., *Electrospun TiO_2 electrodes for dye-sensitized solar cells.* Nanotechnology, 2004. 15(12): p. 1861-1865.
11. Hwang, D., et al., *High-Efficiency, Solid-State, Dye-Sensitized Solar Cells Using Hierarchically Structured TiO_2 Nanofibers.* ACS Applied Materials & Interfaces, 2011. 3(5): p. 1521-1527.
12. Allam, N.K. and C.A. Grimes, *Room Temperature One-Step Polyol Synthesis of Anatase $TiO_{(2)}$ Nanotube Arrays: Photoelectrochemical Properties.* Langmuir, 2009. 25(13): p. 7234-7240.
13. Sordo, C., et al., *Solar photocatalytic disinfection with immobilised $TiO_{(2)}$ at pilot-plant scale.* Water Science and Technology, 2010. 61(2): p. 507-512.
14. Kitano, M., K. Tsujimaru, and M. Anpo, *Hydrogen production using highly active titanium oxide-based photocatalysts.* Topics in Catalysis, 2008. 49(1-2): p. 4-17.
15. Pan, X.A., et al., *TiO_2 nanotubes infiltrated with nanoparticles for dye sensitized solar cells.* Nanotechnology, 2011. 22(23).
16. Michael, G., *Conversion of sunlight to electric power by nanocrystalline dye-sensitized solar cells.* Journal of Photochemistry and Photobiology A: Chemistry, 2004. 164(1-3): p. 3-14.

17. Hagfeldt, A. and M. Graetzel, *Light-Induced Redox Reactions in Nanocrystalline Systems.* Chemical Reviews, 1995. 95(1): p. 49-68.
18. Jia, F., et al., *Preparation of carbon coated TiO_2 nanotubes film and its catalytic application for H_2 generation.* Catalysis Communications, 2011. 12(6): p. 497-501.
19. Grätzel, M., *Artificial photosynthesis: Water cleavage into hydrogen and oxygen by visible light.* Accounts of Chemical Research, 1981. 14(12): p. 376-384.
20. Ikeda, T., et al., *Time-resolved infrared spectroscopy of K_3Ta_3B 2O12 photocatalysts for water splitting.* Journal of Physical Chemistry B, 2006. 110(15): p. 7883-7886.
21. Shen, S., et al., *Visible-light-driven photocatalytic water splitting on nanostructured semiconducting materials.* International Journal of Nanotechnology, 2011. 8(6-7): p. 523-591.
22. Nowotny, J., et al., *TiO_2 Surface Active Sites for Water Splitting.* The Journal of Physical Chemistry B, 2006. 110(37): p. 18492-18495.
23. Gratzel, M., *Photoelectrochemical cells.* Nature, 2001. 414(6861): p. 338-344.
24. Cao, S., K.L. Yeung, and P.L. Yue, *An investigation of trichloroethylene photocatalytic oxidation on mesoporous titania-silica aerogel catalysts.* Applied Catalysis B-Environmental, 2007. 76(1-2): p. 64-72.
25. Popat, K.C., et al., *Titania nanotubes: A novel platform for drug-eluting coatings for medical implants?* Small, 2007. 3(11): p. 1878-1881.
26. Asahi, R., et al., *Electronic and optical properties of anatase TiO_2.* Physical Review B, 2000. 61(11): p. 7459-7465.
27. Aarik, J., et al., *Effect of crystal structure on optical properties of TiO_2 films grown by atomic layer deposition.* Thin Solid Films, 1997. 305(1-2): p. 270-273.
28. Huang, S.Y., et al., *Charge Recombination in Dye-Sensitized Nanocrystalline TiO_2 Solar Cells.* The Journal of Physical Chemistry B, 1997. 101(14): p. 2576-2582.
29. Majjad, L.Z., *Dye-modified nano crystalline TiO_2 surfaces in light-driven water purification organic contaminates*, An-Najah National University Faculty of Graduate Studies.
30. Gai, Y.Q., et al., *Design of Narrow-Gap TiO_2: A Passivated Codoping Approach for Enhanced Photoelectrochemical Activity.* Physical Review Letters, 2009. 102(3).
31. Wilson, N.C., I.E. Grey, and S.P. Russo, *Nonmetal Doping at Octahedral Vacancy Sites in Rutile: A Quantum Mechanical Study.* The Journal of Physical Chemistry C, 2007. 111(29): p. 10915-10922.
32. Kontos, A.G., et al., *Photo-induced effects on self-organized TiO_2 nanotube arrays: the influence of surface morphology.* Nanotechnology, 2009. 20(4): p. 045603.
33. Hornyak, G.L., et al., *Template synthesis of carbon nanotubes.* Nanostructured Materials, 1999. 12(1-4): p. 83-88.
34. Chen, X.B. and S.S. Mao, *Synthesis of titanium dioxide ($TiO_{(2)}$) nanomaterials.* Journal of Nanoscience and Nanotechnology, 2006. 6(4): p. 906-925.
35. Wei, M.D., et al., *Synthesis of tubular titanate via a self-assembly and self-removal process.* Inorganic Chemistry, 2006. 45(14): p. 5684-5690.

36. Richter, C., et al., *Ultrahigh-aspect-ratio titania nanotubes.* Advanced Materials, 2007. 19(7): p. 946-+.
37. Bauer, S., et al., *Size selective behavior of mesenchymal stem cells on ZrO(2) and TiO(2) nanotube arrays.* Integrative Biology, 2009. 1(8-9): p. 525-532.
38. Berger, S., et al., *Influence of Water Content on the Growth of Anodic TiO(2) Nanotubes in Fluoride-Containing Ethylene Glycol Electrolytes.* Journal of the Electrochemical Society, 2010. 157(1): p. C18-C23.
39. Chen, P., et al., *Solid-state dye-sensitized solar cells using TiO(2) nanotube arrays on FTO glass.* Journal of Materials Chemistry, 2009. 19(30): p. 5325-5328.
40. Albu, S.P., et al., *250 mu m long anodic TiO(2) nanotubes with hexagonal self-ordering.* Physica Status Solidi-Rapid Research Letters, 2007. 1(2): p. R65-R67.
41. Albu, S.P., et al., *Formation of Double-Walled TiO(2) Nanotubes and Robust Anatase Membranes.* Advanced Materials, 2008. 20(21): p. 4135-+.
42. Berger, S., et al., *Transparent TiO_2 Nanotube Electrodes via Thin Layer Anodization: Fabrication and Use in Electrochromic Devices.* Langmuir, 2009. 25(9): p. 4841-4844.
43. Passalacqua, R., et al., *Anodically Formed TiO_2 Thin Films: Evidence for a Multiparameter Dependent Photocurrent-Structure Relationship.* Nanoscience and Nanotechnology Letters, 2012. 4(2): p. 142-148.
44. Jun, Y., J.H. Park, and M.G. Kang, *The preparation of highly ordered TiO_2 nanotube arrays by an anodization method and their applications.* Chemical Communications, 2012. 48(52): p. 6456-6471.
45. Chen, Y., et al., *Large-scale sparse TiO_2 nanotube arrays by anodization.* Journal of Materials Chemistry, 2012. 22(13): p. 5921-5923.
46. Albu, S.P., D. Kim, and P. Schmuki, *Growth of Aligned TiO_2 Bamboo-Type Nanotubes and Highly Ordered Nanolace.* Angewandte Chemie International Edition, 2008. 47(10): p. 1916-1919.
47. Kim, D., et al., *Bamboo-Type TiO_2 Nanotubes: Improved Conversion Efficiency in Dye-Sensitized Solar Cells.* Journal of the American Chemical Society, 2008. 130(49): p. 16454-+.
48. Macak, J.M., et al., *Smooth anodic TiO_2 nanotubes: annealing and structure.* physica status solidi (a), 2006. 203(10): p. R67-R69.
49. Tighineanu, A., et al., *Conductivity of TiO_2 nanotubes: Influence of annealing time and temperature.* Chemical Physics Letters, 2010. 494(4–6): p. 260-263.
50. Allam, N.K. and C.A. Grimes, *Formation of vertically oriented TiO_2 nanotube arrays using a fluoride free HCl aqueous electrolyte.* Journal of Physical Chemistry C, 2007. 111(35): p. 13028-13032.
51. Grimes, C.A., *Synthesis and application of highly ordered arrays of TiO_2 nanotubes.* Journal of Materials Chemistry, 2007. 17(15): p. 1451-1457.
52. Mor, G.K., et al., *Enhanced photocleavage of water using titania nanotube arrays.* Nano Letters, 2005. 5(1): p. 191-195.
53. Gong, J., Y. Lai, and C. Lin, *Electrochemically multi-anodized TiO_2 nanotube arrays for enhancing hydrogen generation by photoelectrocatalytic water splitting.* Electrochimica Acta, 2010. 55(16): p. 4776-4782.
54. Li, S., et al., *Anodization Fabrication of Highly Ordered TiO_2 Nanotubes.* The Journal of Physical Chemistry C, 2009. 113(29): p. 12759-12765.

55. Hahn, R., J.M. Macak, and P. Schmuki, *Rapid anodic growth of TiO_2 and WO_3 nanotubes in fluoride free electrolytes.* Electrochemistry Communications, 2007. 9(5): p. 947-952.
56. Lohrengel, M.M., *Thin Anodic Oxide Layers on Aluminum and Other Valve Metals - High-Field Regime.* Materials Science & Engineering R-Reports, 1993. 11(6): p. 243-294.
57. Sul, Y.T., et al., *The electrochemical oxide growth behaviour on titanium in acid and alkaline electrolytes.* Medical Engineering & Physics, 2001. 23(5): p. 329-346.
58. Oregan, B. and M. Gratzel, *A Low-Cost, High-Efficiency Solar-Cell Based on Dye-Sensitized Colloidal TiO_2 Films.* Nature, 1991. 353(6346): p. 737-740.
59. Paulose, M., et al., *Anodic Growth of Highly Ordered TiO_2 Nanotube Arrays to 134 μm in Length.* The Journal of Physical Chemistry B, 2006. 110(33): p. 16179-16184.
60. Taveira, L.V., et al., *Initiation and growth of self-organized TiO_2 nanotubes anodically formed in $NH_4F/(NH_4)(_2)SO_4$ electrolytes.* Journal of the Electrochemical Society, 2005. 152(10): p. B405-B410.
61. Yasuda, K. and P. Schmuki, *Control of morphology and composition of self-organized zirconium titanate nanotubes formed in $(NH_4)(_2)SO_4/NH_4F$ electrolytes.* Electrochimica Acta, 2007. 52(12): p. 4053-4061.
62. Chok, C.L., B.L. Ng, and F.K. Yam, *The effects of fluoride-based electrolyte concentrations on the morphology of self-organized titania nanotubes.* Optoelectronics and Advanced Materials-Rapid Communications, 2010. 4(2): p. 148-150.
63. Wang, J. and Z.Q. Lin, *Anodic Formation of Ordered $TiO(_2)$ Nanotube Arrays: Effects of Electrolyte Temperature and Anodization Potential.* Journal of Physical Chemistry C, 2009. 113(10): p. 4026-4030.
64. Lee, W., et al., *Structural engineering of nanoporous anodic aluminium oxide by pulse anodization of aluminium.* Nature Nanotechnology, 2008. 3(4): p. 234-239.
65. Paulose, M., et al., *TiO_2 nanotube arrays of 1000 mu m length by anodization of titanium foil: Phenol red diffusion.* Journal of Physical Chemistry C, 2007. 111(41): p. 14992-14997.
66. Sun, L.D., et al., *Effect of electric field strength on the length of anodized titania nanotube arrays.* Journal of Electroanalytical Chemistry, 2009. 637(1-2): p. 6-12.
67. Yin, H., H. Liu, and W.Z. Shen, *The large diameter and fast growth of self-organized TiO_2 nanotube arrays achieved via electrochemical anodization.* Nanotechnology, 2010. 21(3).
68. Sreekantan, S., et al., *Influence of electrolyte pH on TiO_2 nanotube formation by Ti anodization.* Journal of Alloys and Compounds, 2009. 485(1–2): p. 478-483.
69. Macak, J.M. and P. Schmuki, *Anodic growth of self-organized anodic TiO_2 nanotubes in viscous electrolytes.* Electrochimica Acta, 2006. 52(3): p. 1258-1264.
70. Zwilling, V., M. Aucouturier, and E. Darque-Ceretti, *Anodic oxidation of titanium and TA_6V alloy in chromic media. An electrochemical approach.* Electrochimica Acta, 1999. 45(6): p. 921-929.

71. Gong, D., et al., *Titanium oxide nanotube arrays prepared by anodic oxidation.* Journal of Materials Research, 2001. 16(12): p. 3331-3334.
72. Mor, G.K., et al., *A review on highly ordered, vertically oriented TiO_2 nanotube arrays: Fabrication, material properties, and solar energy applications.* Solar Energy Materials and Solar Cells, 2006. 90(14): p. 2011-2075.
73. Macak, J.M., K. Sirotna, and P. Schmuki, *Self-organized porous titanium oxide prepared in Na_2SO_4/NaF electrolytes.* Electrochimica Acta, 2005. 50(18): p. 3679-3684.
74. Raja, K.S., M. Misra, and K. Paramguru, *Formation of self-ordered nano-tubular structure of anodic oxide layer on titanium.* Electrochimica Acta, 2005. 51(1): p. 154-165.
75. Macak, J.M., H. Tsuchiya, and P. Schmuki, *High-aspect-ratio TiO_2 nanotubes by anodization of titanium.* Angewandte Chemie-International Edition, 2005. 44(14): p. 2100-2102.
76. Macak, J.M., et al., *Smooth anodic TiO_2 nanotubes.* Angewandte Chemie-International Edition, 2005. 44(45): p. 7463-7465.
77. Yang, D.J., et al., *Fabrication of a patterned $TiO_{(2)}$ nanotube arrays in anodic oxidation.* Journal of Electroceramics, 2009. 23(2-4): p. 159-163.
78. Shankar, K., et al., *Cation effect on the electrochemical formation of very high aspect ratio TiO_2 nanotube arrays in formamide - Water mixtures.* Journal of Physical Chemistry C, 2007. 111(1): p. 21-26.
79. Nakayama, K., T. Kubo, and Y. Nishikitania, *Anodic formation of titania nanotubes with ultrahigh aspect ratio.* Electrochemical and Solid State Letters, 2008. 11(3): p. C23-C26.
80. Fujishima, A. and K. Honda, *Electrochemical Photolysis of Water at a Semiconductor Electrode.* Nature, 1972. 238(5358): p. 37-+.
81. Herrmann, J.M., *Heterogeneous photocatalysis: State of the art and present applications.* Topics in Catalysis, 2005. 34(1-4): p. 49-65.
82. Dodd, A., et al., *Optical and photocatalytic properties of nanocrystalline TiO_2 synthesised by solid-state chemical reaction.* Journal of Physics and Chemistry of Solids, 2007. 68(12): p. 2341-2348.
83. Cristante, V.M., et al., *Synthesis and characterization of TiO_2 chemically modified by Pd(II) 2-aminothiazole complex for the photocatalytic degradation of phenol.* Journal of Photochemistry and Photobiology A: Chemistry, 2008. 195(1): p. 23-29.
84. Li, G. and K.A. Gray, *The solid–solid interface: Explaining the high and unique photocatalytic reactivity of TiO_2-based nanocomposite materials.* Chemical Physics, 2007. 339(1-3): p. 173-187.
85. Yu, J., et al., *Effects of calcination temperature on the microstructures and photocatalytic activity of titanate nanotubes.* Journal of Molecular Catalysis A: Chemical, 2006. 249(1-2): p. 135-142.
86. Fujishima, A., X. Zhang, and D.A. Tryk, *TiO_2 photocatalysis and related surface phenomena.* Surface Science Reports, 2008. 63(12): p. 515-582.
87. Shankar, K., et al., *A study on the spectral photoresponse and photoelectrochemical properties of flame-annealed titania nanotube-arrays.* Journal of Physics D-Applied Physics, 2005. 38(18): p. 3543-3549.

88. Yang, L.X., et al., *Fabrication and Characterization of Pt/C-TiO(2) Nanotube Arrays as Anode Materials for Methanol Electrocatalytic Oxidation.* Energy & Fuels, 2009. 23: p. 3134-3138.
89. Yang, Y., X.H. Wang, and L.T. Li, *Synthesis and photovoltaic application of high aspect-ratio TiO_2 nanotube arrays by anodization.* Journal of the American Ceramic Society, 2008. 91(9): p. 3086-3089.
90. Nozik, A.J. and R. Memming, *Physical Chemistry of Semiconductor−Liquid Interfaces.* The Journal of Physical Chemistry, 1996. 100(31): p. 13061-13078.
91. Liu, Z., et al., *Highly ordered TiO_2 nanotube arrays with controllable length for photoelectrocatalytic degradation of phenol.* Journal of Physical Chemistry C, 2008. 112(1): p. 253-259.
92. Albu, S.P., et al., *Self-organized, free-standing TiO_2 nanotube membrane for flow-through photocatalytic applications.* Nano Letters, 2007. 7(5): p. 1286-1289.
93. Park, J., S. Kim, and A. Bard, *Novel Carbon-Doped TiO_2 Nanotube Arrays with High Aspect Ratios for Efficient Solar Water Splitting.* Nano Letters, 2005. 6(1): p. 24-28.
94. Bak, T., et al., *Photo-electrochemical hydrogen generation from water using solar energy. Materials-related aspects.* International Journal of Hydrogen Energy, 2002. 27(10): p. 991-1022.
95. Hoffmann, M.R., et al., *Environmental Applications of Semiconductor Photocatalysis.* Chemical Reviews, 1995. 95(1): p. 69-96.
96. Cowan, A.J., et al., *Water Splitting by Nanocrystalline TiO_2 in a Complete Photoelectrochemical Cell Exhibits Efficiencies Limited by Charge Recombination.* The Journal of Physical Chemistry C, 2010. 114(9): p. 4208-4214.
97. Zhou, C., et al., *Site-specific photocatalytic splitting of methanol on TiO_2(110).* Chemical Science, 2010. 1(5): p. 575-580.
98. Gurunathan, K., P. Maruthamuthu, and M.V.C. Sastri, *Photocatalytic hydrogen production by dye-sensitized Pt/SnO_2 and Pt/SnO_2/RuO_2 in aqueous methyl viologen solution.* International Journal of Hydrogen Energy, 1997. 22(1): p. 57-62.
99. Nada, A.A., et al., *Studies on the photocatalytic hydrogen production using suspended modified TiO_2 photocatalysts.* International Journal of Hydrogen Energy, 2005. 30(7): p. 687-691.
100. Fujihara, B., T. Ohno, and M. Matsumura, *Splitting of water by electrochemical combination of two photocatalytic reactions on TiO_2 particles.* Journal of the Chemical Society-Faraday Transactions, 1998. 94(24): p. 3705-3709.
101. Litter, M.I., *Heterogeneous photocatalysis - Transition metal ions in photocatalytic systems.* Applied Catalysis B-Environmental, 1999. 23(2-3): p. 89-114.
102. Choi, W.Y., A. Termin, and M.R. Hoffmann, *The Role of Metal-Ion Dopants in Quantum-Sized TiO_2 - Correlation between Photoreactivity and Charge-Carrier Recombination Dynamics.* Journal of Physical Chemistry, 1994. 98(51): p. 13669-13679.
103. Asahi, R., et al., *Visible-Light Photocatalysis in Nitrogen-Doped Titanium Oxides.* Science, 2001. 293(5528): p. 269-271.

104. Martyanov, I.N., et al., *Structural defects cause TiO_2-based photocatalysts to be active in visible light.* Chemical Communications, 2004(21): p. 2476-2477.
105. Ihara, T., et al., *Visible-light-active titanium oxide photocatalyst realized by an oxygen-deficient structure and by nitrogen doping.* Applied Catalysis B: Environmental, 2003. 42(4): p. 403-409.
106. Gratzel, M., *Photovoltaic and photoelectrochemical conversion of solar energy.* Philosophical Transactions of the Royal Society a-Mathematical Physical and Engineering Sciences, 2007. 365(1853): p. 993-1005.
107. Zhu, K., et al., *Enhanced charge-collection efficiencies and light scattering in dye-sensitized solar cells using oriented TiO_2 nanotubes arrays.* Nano Letters, 2007. 7(1): p. 69-74.
108. Linsebigler, A.L., G. Lu, and J.T. Yates, *Photocatalysis on TiO_2 Surfaces: Principles, Mechanisms, and Selected Results.* Chemical Reviews, 1995. 95(3): p. 735-758.
109. Tung, Y.C., *Effect of morpholgies and electronic properites of metal oxide nanostrucure layer on dye sensitized solar cells* 2010, The University of Hong Kong.
110. Schmidt-Stein, F., et al., *X-ray induced photocatalysis on $TiO_{(2)}$ and $TiO_{(2)}$ nanotubes: Degradation of organics and drug release.* Electrochemistry Communications, 2009. 11(11): p. 2077-2080.
111. Song, Y.Y., et al., *Amphiphilic TiO_2 Nanotube Arrays: An Actively Controllable Drug Delivery System.* Journal of the American Chemical Society, 2009. 131(12): p. 4230-4232.
112. Peng, L.M., et al., *Long-Term Small Molecule and Protein Elution from TiO_2 Nanotubes.* Nano Letters, 2009. 9(5): p. 1932-1936.
113. Varghese, O.K., et al., *Hydrogen sensing using titania nanotubes.* Sensors and Actuators B: Chemical, 2003. 93(1-3): p. 338-344.
114. Wisitsoraat, A., et al., *Characterization of n-type and p-type semiconductor gas sensors based on NiO_x doped TiO_2 thin films.* Thin Solid Films, 2009. 517(8): p. 2775-2780.
115. Korotcenkov, G., *Metal oxides for solid-state gas sensors: What determines our choice?* Materials Science and Engineering B-Solid State Materials for Advanced Technology, 2007. 139(1): p. 1-23.
116. Miyazaki, H., et al., *Hydrogen-sensing properties of anodically oxidized TiO_2 film sensors - Effects of preparation and pretreatment conditions.* Sensors and Actuators B-Chemical, 2005. 108(1-2): p. 467-472.
117. Lim, S.H., et al., *Room-Temperature Hydrogen Uptake by TiO_2 Nanotubes.* Inorganic Chemistry, 2005. 44(12): p. 4124-4126.
118. Fujishima, A. and T.N. Rao, *Interfacial photochemistry: Fundamentals and applications.* Pure and Applied Chemistry, 1998. 70(11): p. 2177-2187.
119. Fujishima, A. and X.T. Zhang, *Titanium dioxide photocatalysis: present situation and future approaches.* Comptes Rendus Chimie, 2006. 9(5-6): p. 750-760.
120. Ren, Y., et al., *Nanoparticulate $TiO_2(B)$: An Anode for Lithium-Ion Batteries.* Angewandte Chemie International Edition, 2012. 51(9): p. 2164-2167.

121. Su, X., et al., *Advanced titania nanostructures and composites for lithium ion battery.* Journal of Materials Science, 2012. 47(6): p. 2519-2534.
122. Lee, E., *Scanning Electron Microscopy and x-R Microanalysis*. 1993, USA: PTR Prentice-Hall, Inc. 8.
123. Holt, D.B. and D.C. Joy, *SEM Microcharacterization of semiconductors*. Vol. 5. 1989, London, UK: Academic press limited.
124. Goldstein, J.I., et al., eds. *Scanning Electron Microscopy and X-Ray Microanalysis A text for Biologists, Materials Scientists, and Geologists*. 1981, Plenum press.: London.
125. Jeol and S.A. Technology, *A Guide to Scanning Microscope Observation*.
126. Jenkins, T.E., *Semiconductor Science*. 1995, London: printice Hall international(UK)Limited.
127. Clugston, P.A.A.M., *Principles of physical chemistry.* 1982: p. 54.
128. Macak, J.M., *Growth of Anodic Self-Organized Titanium Dioxide Nanotube Layer* 2008, Erlangen-Nürnberg.
129. Thamaphat, K., P. Limsuwan, and B. Ngotawornchai, *Phase Characterization of TiO_2 Powder by XRD and TEM* Kasetsart J. (Nat. Sci.), 2008. 42: p. 357 - 361.
130. Paulose, M., et al., *Visible light photoelectrochemical and water-photoelectrolysis properties of titania nanotube arrays.* Journal of Photochemistry and Photobiology a-Chemistry, 2006. 178(1): p. 8-15.
131. Liu, Z.Y., et al., *Hydrogen generation under sunlight by self ordered $TiO_{(2)}$ nanotube arrays.* International Journal of Hydrogen Energy, 2009. 34(8): p. 3250-3257.
132. Zhu, J.F. and M. Zach, *Nanostructured materials for photocatalytic hydrogen production.* Current Opinion in Colloid & Interface Science, 2009. 14(4): p. 260-269.
133. Roukes, S.F.a.M.L., ed. *understanding nanotechnology*. 2002, Scientific American,Inc.,and Byron Preiss Visual Publications, Inc. 39.
134. Bermudez, V.M., *Low-energy electron-beam effects on poly(methyl methacrylate) resist films.* Journal of Vacuum Science & Technology B, 1999. 17(6): p. 2512-2518.
135. Ma, S.Q., et al., *Polystyrene negative resist for high-resolution electron beam lithography.* Nanoscale Research Letters, 2011. 6.
136. Madou, M., *Fundamentals of Microfabrication.* 2002: p. pp. 9. ISBN 0-8493-0826-7.
137. Park, J., et al., *Narrow Window in Nanoscale Dependent Activation of Endothelial Cell Growth and Differentiation on TiO_2 Nanotube Surfaces.* Nano Letters, 2009. 9(9): p. 3157-3164.
138. Gao, X.F., et al., *An Efficient Method To Form Heterojunction $CdS/TiO_{(2)}$ Photoelectrodes Using Highly Ordered $TiO_{(2)}$ Nanotube Array Films.* Journal of Physical Chemistry C, 2009. 113(47): p. 20481-20485.
139. Kang, T.S., et al., *Fabrication of Highly-Ordered TiO_2 Nanotube Arrays and Their Use in Dye-Sensitized Solar Cells.* Nano Letters, 2009. 9(2): p. 601-606.

140. Kim, D., et al., *Formation of a Non-Thickness-Limited Titanium Dioxide Mesosponge and its Use in Dye-Sensitized Solar Cells.* Angewandte Chemie-International Edition, 2009. 48(49): p. 9326-9329.
141. Su, Z.X., G. Hahner, and W.Z. Zhou, *Investigation of the pore formation in anodic aluminium oxide.* Journal of Materials Chemistry, 2008. 18(47): p. 5787-5795.
142. Macak, J.M., S.P. Albu, and P. Schmuki, *Towards ideal hexagonal self-ordering of TiO_2 nanotubes.* Physica Status Solidi-Rapid Research Letters, 2007. 1(5): p. 181-183.
143. Macak, J.M., et al., *Mechanistic aspects and growth of large diameter self-organized TiO_2 nanotubes.* Journal of Electroanalytical Chemistry, 2008. 621(2): p. 254-266.
144. Yoriya, S. and C.A. Grimes, *Self-Assembled $TiO_{(2)}$ Nanotube Arrays by Anodization of Titanium in Diethylene Glycol: Approach to Extended Pore Widening.* Langmuir, 2010. 26(1): p. 417-420.
145. Yoriya, S., et al., *Initial studies on the hydrogen gas sensing properties of highly-ordered high aspect ratio TiO_2 nanotube-arrays 20 mu m to 222 mu m in length.* Sensor Letters, 2006. 4(3): p. 334-339.
146. Mohamed, A.E., et al., *Fabrication of Titania Nanotube Arrays in Viscous Electrolytes.* Journal of Nanoscience and Nanotechnology, 2010. 10(3): p. 1998-2008.
147. Su, Z.X. and W.Z. Zhou, *Formation Mechanism of Porous Anodic Aluminium and Titanium Oxides.* Advanced Materials, 2008. 20(19): p. 3663-+.
148. Su, Z.X. and W.Z. Zhou, *Formation, microstructures and crystallization of anodic titanium oxide tubular arrays.* Journal of Materials Chemistry, 2009. 19(16): p. 2301-2309.
149. Thebault, F., et al., *Modeling of Growth and Dissolution of Nanotubular Titania in Fluoride-Containing Electrolytes.* Electrochemical and Solid State Letters, 2009. 12(3): p. C5-C9.
150. Lu, S.J., et al., *Ionic nano-convection in anodisation of aluminium plate.* Chemical Communications, 2009(37): p. 5639-5641.
151. Chen, Y., et al., *Formation of titanium oxide nanogrooves island arrays by anodization.* Electrochemistry Communications, 2010. 12(1): p. 86-89.
152. Lee, B.G., et al., *Formation behavior of anodic $TiO_{(2)}$ nanotubes in fluoride containing electrolytes.* Transactions of Nonferrous Metals Society of China, 2009. 19(4): p. 842-845.
153. Su, Z.X., M. Buehl, and W.Z. Zhou, *Dissociation of Water During Formation of Anodic Aluminum Oxide.* Journal of the American Chemical Society, 2009. 131(24): p. 8697-8702.
154. Valota, A., et al., *Influence of water content on nanotubular anodic titania formed in fluoride/glycerol electrolytes.* Electrochimica Acta, 2009. 54(18): p. 4321-4327.
155. Mor, G.K., et al., *Transparent highly ordered TiO_2 nanotube arrays via anodization of titanium thin films.* Advanced Functional Materials, 2005. 15(8): p. 1291-1296.

156. Yasuda, K., et al., *Mechanistic aspects of the self-organization process for oxide nanotube formation on valve metals.* Journal of the Electrochemical Society, 2007. 154(9): p. C472-C478.
157. Albu, S.P. and P. Schmuki, *Highly defined and ordered top-openings in TiO_2 nanotube arrays.* Physica Status Solidi-Rapid Research Letters, 2010. 4(7): p. 151-153.
158. Ohno, T., K. Sarukawa, and M. Matsumura, *Photocatalytic Activities of Pure Rutile Particles Isolated from TiO_2 Powder by Dissolving the Anatase Component in HF Solution.* The Journal of Physical Chemistry B, 2001. 105(12): p. 2417-2420.
159. Mohapatra, S.K., et al., *A novel method for the synthesis of titania nanotubes using sonoelectrochemical method and its application for photoelectrochemical splitting of water.* Journal of Catalysis, 2007. 246(2): p. 362-369.
160. Canciani, G., *Morphologically Controlled Nanostructure Synthesis For Chiral Catalysis*, 2012, University of Sussex: Brighton. p. 30.
161. Zhang, Z.H., et al., *Aminolysis route to monodisperse titania nanorods with tunable aspect ratio.* Angewandte Chemie-International Edition, 2005. 44(22): p. 3466-3470.
162. Jun, Y.W., et al., *Surfactant-assisted elimination of a high energy facet as a means of controlling the shapes of TiO_2 nanocrystals.* Journal of the American Chemical Society, 2003. 125(51): p. 15981-15985.
163. Yi, D.K., S.J. Yoo, and D.Y. Kim, *Spin-on-based fabrication of titania nanowires using a sol-gel process.* Nano Letters, 2002. 2(10): p. 1101-1104.
164. Zhou, Y., E.Y. Ding, and W.D. Li, *Synthesis of TiO_2 nanocubes induced by cellulose nanocrystal (CNC) at low temperature.* Materials Letters, 2007. 61(28): p. 5050-5052.
165. Tang, J., et al., *An organometallic synthesis of TiO_2 nanoparticles.* Nano Letters, 2005. 5(3): p. 543-548.
166. Weng, C.C., et al., *Using a solution crystal growth method to grow arrays of aligned, individually distinct, single-crystalline TiO_2 nanoneedles within nanocavities.* Chemistry of Materials, 2005. 17(13): p. 3328-3330.
167. Liu, L., et al., *Fabrication of rutile TiO_2 tapered nanotubes with rectangular cross-sections via anisotropic corrosion route.* Chemical Communications, 2010. 46(14): p. 2402-2404.
168. Olzierski, A. and I. Raptis, *Development and molecular-weight issues on the lithographic performance of poly (methyl methacrylate).* Microelectronic Engineering, 2004. 73-4: p. 244-251.
169. Yang, C., et al., *Effects of depositing temperatures on structure and optical properties of TiO_2 film deposited by ion beam assisted electron beam evaporation.* Applied Surface Science, 2008. 254(9): p. 2685-2689.
170. Wilbur, J.L., et al., *Microcontact printing of self-assembled monolayers: Applications in microfabrication.* Nanotechnology, 1996. 7(4): p. 452-457.
171. Kim, Y.K., G.T. Kim, and J.S. Ha, *Simple Patterning via Adhesion between a Buffered-Oxide Etchant-Treated PDMS Stamp and a SiO_2 Substrate.* Advanced Functional Materials, 2007. 17(13): p. 2125-2132.

172. Knez, M., K. Nielsch, and L. Niinistö, *Synthesis and Surface Engineering of Complex Nanostructures by Atomic Layer Deposition.* Advanced Materials, 2007. 19(21): p. 3425-3438.
173. Sander, M.S., et al., *Template-Assisted Fabrication of Dense, Aligned Arrays of Titania Nanotubes with Well-Controlled Dimensions on Substrates.* Advanced Materials, 2004. 16(22): p. 2052-2057.
174. Goh, C., K.M. Coakley, and M.D. McGehee, *Nanostructuring Titania by Embossing with Polymer Molds Made from Anodic Alumina Templates.* Nano Letters, 2005. 5(8): p. 1545-1549.
175. Masuda, H., et al., *Square and triangular nanohole array architectures in anodic alumina.* Advanced Materials, 2001. 13(3): p. 189-192.
176. Al-Abdullah, Z.T.Y., et al., *The influence of hydroxide on the initial stages of anodic growth of TiO(2) nanotubular arrays.* Nanotechnology, 2010. 21(50).
177. Shrestha, N.K., et al., *Magnetically Guided Titania Nanotubes for Site-Selective Photocatalysis and Drug Release.* Angewandte Chemie-International Edition, 2009. 48(5): p. 969-972.
178. Xiao, X.L., et al., *Biocompatibility and in vitro antineoplastic drug-loaded trial of titania nanotubes prepared by anodic oxidation of a pure titanium.* Science in China Series B-Chemistry, 2009. 52(12): p. 2161-2165.
179. Enachi, M., et al., *Cathodoluminescence of TiO_2 nanotubes prepared by low-temperature anodization of Ti foils.* Materials Letters, 2010. 64(20): p. 2155-2158.
180. Balaur, E., et al., *Wetting behaviour of layers of TiO_2 nanotubes with different diameters.* Journal of Materials Chemistry, 2005. 15(42): p. 4488-4491.
181. Gillman, P.K., *Methylene blue implicated in potentially fatal serotonin toxicity.* Anaesthesia, 2006. 61(10): p. 1013-1014.
182. Yao, J. and C.X. Wang, *Decolorization of Methylene Blue with TiO_2 Sol via UV Irradiation Photocatalytic Degradation.* International Journal of Photoenergy, 2010.
183. Moseke, C., et al., *TiO_2 nanotube arrays deposited on Ti substrate by anodic oxidation and their potential as a long-term drug delivery system for antimicrobial agents.* Applied Surface Science, 2012. 258(14): p. 5399-5404.
184. Langer, R.S. and N.A. Peppas, *Present and Future Applications of Biomaterials in Controlled Drug Delivery Systems.* Biomaterials, 1981. 2(4): p. 201-214.
185. Dholam, R., et al., *Physically and chemically synthesized TiO_2 composite thin films for hydrogen production by photocatalytic water splitting.* International Journal of Hydrogen Energy, 2008. 33(23): p. 6896-6903.
186. Mohapatra, S.K., et al., *Efficient photoelectrolysis of water using TiO_2 nanotube arrays by minimizing recombination losses with organic additives.* Journal of Physical Chemistry C, 2008. 112(29): p. 11007-11012.
187. Varghese, O.K., et al., *Crystallization and high-temperature structural stability of titanium oxide nanotube arrays.* Journal of Materials Research, 2003. 18(1): p. 156-165.
188. Regonini, D., et al., *Effect of heat treatment on the properties and structure of TiO_2 nanotubes: phase composition and chemical composition.* Surf. Interface Anal. , 2010. 42: p. 139-144.

189. Hardcastle, F.D., et al., *Photoelectroactivity and Raman spectroscopy of anodized titania (TiO_2) photoactive water-splitting catalysts as a function of oxygen-annealing temperature.* Journal of Materials Chemistry, 2011. 21(17).
190. Ahn, K.S., et al., *The effect of thermal annealing on photoelectrochemical responses of WO_3 thin films.* Journal of Applied Physics, 2007. 101(9).
191. Kumar, K.N.P., K. Keizer, and A.J. Burggraaf, *Textural Evolution and Phase-Transformation in Titania Membranes .1. Unsupported Membranes.* Journal of Materials Chemistry, 1993. 3(11): p. 1141-1149.
192. Kumar, K.P., et al., *Textural Evolution and Phase-Transformation in Titania Membranes .2. Supported Membranes.* Journal of Materials Chemistry, 1993. 3(11): p. 1151-1159.
193. Zhang, Z.H., M.F. Hossain, and T. Takahashi, *Photoelectrochemical water splitting on highly smooth and ordered TiO_2 nanotube arrays for hydrogen generation.* International Journal of Hydrogen Energy, 2010. 35(16): p. 8528-8535.